San Joaquin Renewables
Class VI Permit Application
AoR and Corrective Action Plan

Prepared for

San Joaquin Renewables LLC
McFarland, California

Submitted to

U.S. Environmental Protection Agency Region 9
San Francisco, California

Prepared by

DBS&A
Daniel B. Stephens & Associates, Inc.

a Geo-Logic Company

43 Randolph Road, #129
Silver Spring, Maryland 20904
www.dbstephens.com

Project # DB19.1252.SS

August 16, 2022

AREA OF REVIEW AND CORRECTIVE ACTION PLAN
40 CFR 146.84(b)

SAN JOAQUIN RENEWABLES

1. Facility Information

Facility name:	San Joaquin Renewables Injection Well: SJR-I1
Facility contact:	T.J. Paskach, Ph.D. 1521 West F Ave, Nevada, IA 50201 515-292-1200 x121/tpaskach@frontlinebioenergy.com
Well location:	McFarland, Kern County, California 35.688330, -119.276642

2. Computational Modeling Approach

This AoR and Corrective Action Plan is a component of the San Joaquin Renewables, LLC (SJR) application to the U.S. Environmental Protection Agency Region 9 (U.S. EPA) for an Underground Injection Control (UIC) Class VI permit for a planned facility located in McFarland, California. This plan is one of several separate documents submitted to the U.S. EPA Geologic Sequestration Data Tool (GSDT), and includes required information regarding the Area of Review (AoR) delineation and planned corrective action. Geologic analyses that underpin the conceptual model used in the AoR numerical modeling is primarily described in the narrative permit application report.

The permit application and associated documents were prepared by a team including Daniel B. Stephens & Associates, Inc. (DBS&A), Driltek, Finsterle Geoconsulting, Keystone Diversified Energy, Inc. (KDEI), and Best Core Services. Geologic analyses used to develop the AoR modeling conceptual model were performed primarily by DBS&A, Driltek and KDEI. AoR numerical modeling with the TOUGH simulator was performed by Finsterle Geoconsulting.

2.1. Model Background

According to 40 CFR 146.84, the AoR "is delineated using computational modeling that accounts for the physical and chemical properties of all phases of the injected carbon dioxide stream and displaced fluids, and is based on available site characterization, monitoring, and operational data." This section provides a general description of the numerical simulator used for the analysis.

The computer code used to perform the modeling is the general-purpose compositional reservoir simulator TOUGH2 (Pruess et al., 2012) as implemented in the iTOUGH2 simulation-optimization framework (Finsterle et al., 2017). The TOUGH2 equation-of-state (EOS) module ECO2N (Pruess, 2005) is used to simulate non-isothermal multiphase flow of fluid mixtures of water, carbon dioxide, and sodium chloride (NaCl) in geologic media. The fluids considered are

a water-rich aqueous phase, which also contains dissolved NaCl and carbon dioxide, and a carbon dioxide-rich "gas" phase, which for the pressures and temperatures encountered in deep saline formations used for geologic carbon sequestration is in supercritical condition. Solid salt may also be present. Equilibrium phase partitioning of water and carbon dioxide determines the composition of the aqueous and gaseous phases as a function of temperature, pressure, and salinity (Spycher et al., 2003), as well as the precipitation and dissolution of solid salt. Each of the components may therefore undergo phase changes. Consequently, all phases (aqueous, gaseous, and solid) may be present, and may disappear or appear at any point in the computational model during the course of the simulation. The thermophysical properties of the two fluid phases (specifically density and dynamic viscosity) are calculated as a function of pressure, temperature, and salinity. Brine density varies with pressure, temperature, salinity, and the concentration of dissolved carbon dioxide.

Phase interference is described by user-specified parametric relative permeability and capillary pressure functions. Phase trapping of supercritical carbon dioxide is thus accounted for, whereby the history-dependent increase in the residual gas saturation can be captured using the hysteretic model of Doughty (2013).

For numerical simulation, the continuous space and time variables of the governing equations must be discretized. Space discretization is made directly from the integral form of the mass- and energy-balance equations, without converting them into partial differential equations. This integral finite difference method is applicable to regular or irregular grids in one, two, and three dimensions. Time is discretized fully implicitly as a first-order backward finite difference. Discretization results in a set of strongly coupled nonlinear algebraic equations, with the time-dependent primary thermodynamic variables of all grid blocks as unknowns. These equations are cast in residual form and solved simultaneously using Newton-Raphson iterations. Different methods are available to solve the linear equations arising at each iteration step, such as preconditioned conjugate gradient solvers.

The integration of TOUGH2/ECO2N in iTOUGH2 provides simulation enhancements and additional user features (Finsterle, 2021). For this work, iTOUGH2 capabilities were used to specify and change initial and boundary conditions, to extract the system responses at selected points in space and time, to calculate the first and second moments of the carbon dioxide plume, and to generate visualization files.

TOUGH2 has been extensively used for research and applications involving challenging subsurface multiphase flow and transport problems, including geologic carbon sequestration (see https://tough.lbl.gov/pubs/ for a list of more than 160 peer-reviewed journal articles that use TOUGH2 to study geological carbon dioxide storage). Moreover, TOUGH2 was benchmarked against other simulators used for modeling geologic carbon sequestration as part of the GeoSeq code intercomparison study (Pruess et al., 2004).

2.2. Site Geology and Hydrology

2.2.1. Physical Processes

The injection and redistribution of carbon dioxide in a saline formation involve coupled physical and chemical phenomena, including hydrological flow and transport processes, phase partitioning and geochemical reactions, and geomechanical effects. The numerical model needs to be able to capture the main processes that affect the delineation of the AoR. The potential significance of a process depends on its influence on the main carbon dioxide migration and trapping mechanism, which are understood from extensive research and experience at other geologic carbon sequestration sites. The uncertainty in the geological structure, input parameters and the general system state should also be considered when selecting the processes to be included in the numerical model. Some of these uncertainties and variabilities can be examined using sensitivity analyses (see Section 3.2 below).

The evolution of (a) the free-phase plume of supercritical carbon dioxide (scCO2), (b) the pressure buildup induced by carbon dioxide injection, and (c) the associated brine displacement are predominantly hydrogeological flow and transport processes, which are appropriately described by the multiphase flow formulation of the TOUGH2 simulator. In particular, injected carbon dioxide flows through the geologic formation in response to pressure and viscous forces, accounting for capillary pressure effects and phase interferences described by relative permeabilities for both the aqueous and carbon dioxide-rich phases. As injection proceeds, a buoyant carbon dioxide plume evolves, which may become trapped in larger-scale geological structures (referred to as structural trapping). An accurate representation of the main geological and hydrostratigraphic structures is therefore essential, along with an accurate calculation of the thermophysical properties of the fluid mixtures, which is provided by TOUGH2. On the small scale, the gas phase may also become discontinuous and get trapped in certain portions of the pore space (referred to as phase trapping or hydraulic trapping). The use of an effective residual gas saturation in the relative permeability functions or a fully hysteretic retention model account for these phase-trapping mechanisms. Moreover, carbon dioxide dissolves in the aqueous phase, increasing its density and potentially leading to gravity-driven downwards migration. Finally, geochemical reactions may take place that bind (and thus immobilize) carbon dioxide into carbonate minerals. However, mineralization is typically a slow, long-term geochemical reaction, which is conservatively neglected in these simulations. Geochemical reactions are therefore limited to phase partitioning of the three components, water, carbon dioxide and NaCl, including the potential precipitation of solid salt as the injected carbon dioxide dries out the native brine.

The injection of large amounts of carbon dioxide may lead to significant overpressures (specifically near the injection well) and thus a reduction in the effective stress, potentially leading to reactivation of faults or jeopardize the mechanical integrity of sealing layer. The calculated overpressure has been analyzed to examine the risk of induced seismicity or other geomechanical effects (see the Narrative permit application report). Coupled hydrological-geomechanical processes are not explicitly simulated in the AoR modeling, i.e., no stress-strain calculation is performed; however, the expansion or compression of the pore space in response to changes in fluid pressures is accounted for through an elastic pore compressibility.

The temperature within the model domain increases with depth. However, assuming that the temperature of the injected carbon dioxide is identical to the formation temperature, the simulations are performed in isothermal mode (i.e., the temperature does not vary with time).

2.2.2. Conceptual Model

The TOUGH2 numerical model is based on the conceptual geologic model described in the Narrative permit application report. As described in that report, review of seismic data and well log data was used to create a digital grid model of the area that provides the top elevation of the following formations on a 200 meter grid spacing:

- Ground surface
- Etchegoin
- Miocene
- Santa-Margarita
- Round-Mountain
- Olcese
- Freeman-Jewett
- Pyramid Hills
- Vedder 1
- Vedder 1A
- Vedder 2
- Vedder 3
- Vedder 4
- Cantleberry Sand
- Walker
- Basement

The geologic conceptual model is displayed in a series of cross-sections (Figures 2-23 to 2-27 of the narrative permit application report) and maps (Figures 2-28 through 2-35 of the permit application report). The starting point for the TOUGH numerical model was the 200 m digital geologic grid model.

For the purpose of TOUGH2 numerical modeling, additional layers were incorporated to represent the separate shale and sand units within each of the Vedder formation units. Based on review of well logs, the following assumptions were made regarding vertical layer thickness:

- Uppermost sand units in the Vedder formation were combined into a single model layer, termed the Upper Vedder, that includes the thickness of the Pyramid Hills, Vedder 1,

Vedder 1A and Vedder 2. Shale between the Vedder 1 and Vedder 2 was assumed to be thin and to not represent a significant barrier to vertical flow.

- Vedder 2 shale is placed at the bottom of the Vedder 2 unit, and overlies the Vedder 3 unit. Thickness of the Vedder 2 shale was assumed to be 35 percent of the total Vedder 2 thickness, thin to a minimum of 5 meters (or the entire thickness of the Vedder 2 if less than 5 meters), and thicken to a maximum of 30 meters.

- Vedder 3 shale is placed at the bottom of the Vedder 3 unit, and overlies the Vedder 4 unit. Thickness of the Vedder 3 shale was assumed to be 65 percent of the total Vedder 3 thickness, thin to a minimum of 10 meters (or the entire thickness of the Vedder 3 if less than 10 meters), and thicken to a maximum of 50 meters.

- Vedder 4 shale is placed at the bottom of the Vedder 4 unit, and overlies the Walker formation. Thickness of the Vedder 4 shale was assumed to be 45 percent of the total Vedder 4 thickness, and thin to a minimum of 5 meters (or the entire thickness of the Vedder 4 if less than 5 meters).

- Vedder 4 and Vedder-Cantleberry Sand were combined into a single numerical model layer

The injection site is relatively close to the Pond-Poso Creek fault system. The propagation of both the carbon dioxide plume and the pressure perturbation across the fault line is thus of interest and depends on whether these faults are sealing or non-sealing. As the analyses described in the Narrative permit application report show, the lateral sealing effectiveness critically depends on the shale gouge ratio. Section 2.3 of the Narrative permit application report describes Allan diagrams and shale gouge ratio determination for the Pond-Poso Creek fault, and Figure 2-39 of the permit application report presents a diagram and map of fine-scaled cross-sections that were generated along the fault system.

2.3. Model Domain

Model domain information is summarized in Table 2-1.

The three-dimensional (3-D) mesh for the TOUGH2 simulations presented in this report was created using AMESH (Haukwa, 1998) together with pre- and post-processing scripts written in Python, that (1) process relevant site characterization information, such as geological layering and fault trace data; (2) generate the input file needed to run AMESH; and (3) perform post-processing of AMESH output. Post-processing includes, for example, assigning materials to elements and removing elements and connections that are considered outside the simulation domain. Some details regarding discretization and material assignment are given below.

Creating a 3-D, unstructured grid of Voronoi elements with AMESH requires specification of 2-D grid points in the X-Y plane, which are then repeated at multiple depths in the Z direction. Note that for simplicity, latitude, longitude, and elevation are referred to as X, Y, and Z, respectively. For the current mesh, the X-Y grid is composed of a “background” grid, which contains radial and Cartesian components, within which fault trace grid points are embedded. The resulting X-Y grid is shown in Figure 2-1.

Specifically, the background grid contains (1) a radial portion with 24 equally spaced 15° sectors, centered around the well coordinates (X,Y) = (294,000 meters [m], 3,951,600 m), and extending outward 6 kilometers (km) with a radial spacing from 10 m up to 1,000 m; (2) a Cartesian portion (surrounding the radial portion) with 1,000 m discretization in the X and Y directions; (3) a second, coarser Cartesian portion (surrounding the first Cartesian portion) with 4,000 m discretization in the X and Y directions; and (4) thin layers of elements on the north, south, east, and west boundaries. Discretization in the Z direction is given by uniform 5 m spacing over the vertical extent of relevant geological layers (from elevations of -5,500 m to 400 m).

To accurately represent each fault in the model, grid points are placed along lines determined through interpolation of fault trace data; grid points are automatically spaced along the interpolated lines in a manner that is consistent with the background grid. Additional grid points are placed on the sides of each fault grid point (in a direction from the fault grid point that is perpendicular to the fault trace) to ensure that the fault elements are smoothly connected to each other and have the desired width. In some cases, it is necessary to manually adjust a grid point (e.g., to ensure that intersecting faults are connected appropriately). When fault grid points overlap with or are too close to background grid points, those background grid points are removed.

Figure 2-2 shows a fault embedded within the radial portion of the background grid. Figure 2-3 and Figure 2-4 demonstrate how intersecting faults are connected in the mesh. The Jasmin faults (Figure 2-4) are relatively far away from the carbon dioxide injection area and are therefore embedded in a region of the background mesh with lower resolution.

Note that faults in the model are assumed to be vertical, but they may or may not extend vertically through the entire model. That is, a “potential” fault element at a given X-Y location at one depth may be assigned fault properties, whereas another potential fault element at the same X-Y position and at a different depth may be assigned some other geological material if no fault is present at that depth based on the conceptual model.

Assignment of materials in the mesh is based on (1) a dataset that contains the elevations of the upper surfaces of the geological layers of interest (ground surface, USDW, Round Mountain, Olcese, Freeman-Jewett, multiple sand and shale layers within the Vedder formation, and Walker) on an X-Y grid with a 200 m by 200 m resolution; and (2) fault trace data in which (a) lists of X-Y coordinates form fault traces, (b) the depth ranges over which the faults are present, and (c) fault sections that receive an additional sub-category during the assignment of fault properties (e.g., such that some parts of a fault may be treated as sealing, others as partially sealing or non-sealing).

The procedure for assigning materials to the mesh processes one column of elements at a time. Each column, which corresponds to a unique pair of X-Y coordinates, is categorized as follows: (1) a column of vertical boundary elements (on the north, south, east, or west model boundaries), (2) a column of elements that may belong to a given fault depending on the depth range over which the fault is present, (3) a column of elements that are not fault elements but are next to and share a boundary to the east or west of potential fault elements, or (4) a column of regular elements from the initial background grid (i.e., all other cases).

For each element, it is determined to which geological layer the element belongs based on its elevation Z within a column and the corresponding entry in the table of geological layer data; the

identified material identifier is assigned to the element. Depending on the category of element being considered (described in the previous paragraph), and based on the geological layer determination, some elements require additional consideration.

For example, to reduce the size of the mesh and increase computational efficiency, elements are removed from the mesh if they are outside of what is considered the simulation domain, namely, if they are determined to be: (a) above the ground surface, (b) more than 50 m above the Olcese surface, (c) more than 50 m below the Walker surface; or (d) south of the curved boundary on the southern and parts of the eastern borders of the model. Cutting such elements and connections from the basic grid reduces the number of elements and connections from approximately 1,343,000 to 140,000, and from approximately 4,518,000 to 432,000, respectively.

The bounding box of the final grid is given by the following coordinate ranges: 274,000 m < Longitude < 328,600 m; 3,928,200 m < Latitude < 3,970,600 m; -5,440 masl < elevation < 345 masl. This model domain size is sufficiently large so that boundary effects are insignificant, as confirmed by the results of the analysis (see Case M in Section 3.2). The injection well is located at (X,Y) = (294,000, Y = 3,951,600).

The remaining upper-most and lower-most elements in a column are specified as top and bottom boundary materials, respectively. If the top element was the ground surface, then it receives its own ground surface boundary material instead of the "top" boundary material. If a column of elements is on a vertical boundary, then its elements are given appropriate boundary designations.

The elements in columns that are on a fault trace are generally assigned a fault material. Potential offsets in geological layers exist from one side of a fault to the other. Elements covering the entire vertical extent of both sides of the offset—from the shallowest element on the shallower side of the offset to the deepest element on the deeper side of the offset—are assigned fault materials. Moreover, elements in some faults are treated as sealing while others are treated as partially sealing or non-sealing. These subcategories of fault materials are assigned depending on (1) the location of the element along the fault trace, (2) elevation, and (3) which geological layer is situated to its east.

Each element of the final mesh is assigned to one of 38 material types, each pointing to the appropriate set of property parameters. Figure 2-5 shows a cross section of the materials for a plane going through the injection well from south to north (cross-section location shown on Figure 2-6a).

This three-dimensionally truncated model with an unstructured X-Y mesh is computationally efficient and at the same time provides the resolution required to represent the hydrostratigraphic layering and fault structures, and to resolve regions where strong gradients (in pressure and saturation) are expected, specifically near the injection well and fault trace lines. Moreover, the model includes the components and features that are key to delineating the AoR: (1) The injection reservoir (Vedder) and its substructure of alternating sand and shale layers; (2) the sandstone Olcese formation; (3) the confining layers above the Vedder and below the Olcese; (4) the overall inclination and detailed topography of the injection layers and their confining layers; (5) the faults, with subcategories of their sealing properties; and (6) offsets of layers across faults.

Table 2-1. Model domain information (note coordinates are the bounding box of an unstructured grid).

Coordinate System	NAD27/UTM Zone 11N		
Coordinate System Units	Meters		
Coordinate of X min	274,000	**Coordinate of X max**	328,600
Coordinate of Y min	3,928,200	**Coordinate of Y max**	3,970,600
Elevation of Z min	-5,540	**Elevation of Z max**	345

2.4. Porosity and Permeability

Numerical model initial parameter values were assigned based on laboratory core analyses and values from available literature for the area. Porosity and permeability values were based on laboratory core analyses (as described in the Narrative permit application). Table 2-2 summarizes porosity and permeability values for each formation. Horizontal permeability was calculated based on the geometric mean of all sample results, and vertical permeability was calculated based on the harmonic mean of all sample results (Fetter, 2001). Horizontal permeability for Vedder sand units ranges from 192 to 613 millidarcies (mD) and vertical permeability ranges from 62 to 154 mD. Vedder shale units range in horizontal permeability from 0.11 to 0.91 mD, and vertical permeability 0.0052 to 0.025 mD. The Freeman Jewett formation horizontal permeability is calculated to be 0.26 mD, and vertical permeability is 0.0036 mD. The Olcese permeability values were calculated from weighted geometric and harmonic averages assuming 90 percent sands and 10 percent shales, and horizontal and vertical permeability are 77 and 4.3 mD respectively. Round Mountain horizontal and vertical permeability values are 0.037 and 0.00073 mD.

Representative porosity values were obtained from the median of all values for each formation, and ranged from 15-percent (Vedder 3 shale) to 34-percent (Upper Vedder sands).

Permeability and porosity values obtained from the laboratory core analyses generally compare well to a previous compilation given by Birkholzer et al. (2011) and reproduced in Appendix A. Birkholzer et al. (2011) present a Vedder sand horizontal permeability of 303 mD and vertical permeability of 61 mD; Vedder shale values are horizontal permeability of 0.1 mD and vertical permeability of 0.05 mD. Freeman-Jewett (referred to as Temblor-Freeman in Birkholzer et al., 2011) horizontal permeability is given as 0.002 mD and vertical as 0.001 mD. Porosity values are also generally similar, with a value of 0.26 given for the Vedder sand units (compared to a range of 0.26 to 0.34 given in Table 2-1).

Table 2-3 of this report presents a conceptualization of the permeability of the Pond-Poso Creek fault that was generated for the purpose of TOUGH2 modeling. Permeability of the fault gouge at each fault location was determined based on the shale gouge ratio at each location for the Olcese, Upper Vedder, and Vedder 3 units. Four subcategories were assigned to each location and geologic formation along the fault, with horizontal permeability ranging from 0.001 to 0.5 millidarcies. As discussed in Section 3.2, below, additional sensitivity analysis simulations were conducted considering both sealing and non-sealing faults.

Figure 2-5 shows cross sections of the permeability and porosity for a plane going through the injection well from south to north (cross-section location shown on Figure 2-6a).

2.5. Constitutive Relationships and Other Rock Properties

Remaining parameter values for pore compressibility and van Genuchten parameters were taken from Birkholzer et al. (2011) reproduced in Appendix A and discussed in more detail below. Figures 2-7 and 2-8 show, respectively, the relative permeability and capillary pressure curves for three sets of van Genuchten parameters including the Reference Case and sensitivity analyses discussed in Section 3.2, below.

2.6. Boundary Conditions

Pressure, temperature, and salinity profiles from a static initialization run are kept constant at the top boundary as well as along the vertical side boundaries of the three-dimensional model. The pressure profiles along these boundaries account for depth-dependent density variations caused by the temperature gradient and salinity stratification. The model domain size is sufficiently large so that boundary effects are insignificant, as confirmed by the results of the analysis (see Case M in Section 3.2).

2.7. Initial Conditions

An initial state must be defined from which the system will evolve once carbon dioxide injection commences. This means that the initial values of state variables—pressure, temperature, saturation, and salinity—must be specified throughout the model domain. As the initial state is not well known from direct measurements, a simplified, static distribution is used as an approximation, assuming that the system is initially near equilibrium.

This approximation is considered appropriate and conservative given that the AoR is delineated mainly based on two simulation results: (1) the saturation of the carbon dioxide-rich phase, and (2) the overpressure induced by the carbon dioxide injection in comparison to a location-specific, admissible overpressure. Both criteria refer to calculated changes (in saturation and pressure) rather than their absolute values, significantly reducing the impact of uncertainties in initial conditions on AoR delineation.

Static initial conditions for the model are generated using a steady-state calculation as follows:

- The system is assumed to be fully saturated (single-phase liquid conditions) with initially no dissolved carbon dioxide in the aqueous phase.
- At an elevation of 360 m (which is the land surface elevation above the highest elevation represented in the model), a constant pressure of 1 bar (atmospheric conditions) is specified.
- At an elevation of 360 m, a constant temperature of 18.4°C (approximate mean annual temperature) is specified.

At an elevation of -5,440 m, which is the lowest elevation represented in the model, a constant temperature of 105°C is specified. This value is imposed because of the temperature limit of the ECO2N module (Pruess, 2005). The resulting geothermal gradient of 15°C/km is smaller than the gradient projected for the sequestration site. The error induced by a lower temperature at the elevation of the carbon dioxide plume is considered acceptable.[1]

Salinity is specified as a function of depth as follows (see permit application report Section 2.7):

- For a depth less than 152 m (500 ft), NaCl concentration is 98 ppm; for a depth range between 152 and 1,220 m (500 and 4,000 ft), salinity increases linearly from 98 to 25,000 ppm; below 1,220 m, salinity is constant at 25,000 ppm.
- The bottom boundary and all side boundaries are hydrologically closed.
- The system with these initial and boundary conditions is run to steady state. The resulting static pressure profile, which accounts for the depth-dependent density variation due to changes in temperature and salinity, provides the initial conditions of the three-dimensional model used to simulate carbon dioxide injection.
- The initial pressure and temperature at the injection point are approximately 260 bar and 60°C, respectively, i.e., considerably above the critical pressure and temperature for carbon dioxide of 73.82 bar and 31.04°C.
- The pressure, temperature, and salinity profiles from the initialization run are kept constant at the top boundary as well as along the vertical side boundaries of the three-dimensional model.

Because the process described above yields profiles that are in static equilibrium, they can be used as initial conditions for all subsequent simulations, including the sensitivity analyses (see Section 3.2) in which some of the hydrogeological parameters are changed. As mentioned above, AoR delineation predominantly depends on changes of the system state with respect to these initial conditions rather than their absolute values, which considerably reduces the impact an error in the initial conditions has on the results of interest.

2.8. Operational Information

It is assumed that pure carbon dioxide is injected at a constant mass rate of 1,200 tons per day for 15 years. Flow within the injection well is not explicitly simulated. For the base case simulation injection is assumed in the Upper Vedder only (see Section 2.2 above).

[1] The temperature at the injection interval is approximately 80°C (see Appendix B), i.e., about 80°C higher than the assumed temperature in the model, which is 80°C due to a temperature limitation of 80°C (specified at the bottom of the model at a depth of -5,440 masl) in the equation-of-state module ECO2N (Pruess, 2005). A temperature of 80°C leads to a hydraulic conductivity for scCO2 that is about 9% higher than that at 60°C. This difference is considered insignificant.

2.9. Fracture Pressure and Fracture Gradient

As discussed in the narrative application report (narrative application report Section 7.1, Section 2.5, Appendix G) the fracture gradient at the Vedder formation is calculated to be 0.66 psi/ft, or 5,132 psi (35,384,000 Pa; 354 bar) at the planned injection depth of approximately 7,775 ft bgs. Class VI requirements are that injection pressure shall not exceed 90 percent of the fracture pressure, or 319 bar. Maximum pressure predicted from TOUGH modeling during the injection phase is 265 bar, and over-pressure is on the order of 5.5 bar (550,000 Pa; see discussion below). The maximum overpressure at the well is somewhat higher and will be derived from the experimentally determined injectivity index during well testing. It is apparent, however, that the injection pressure will be safely below the fracture initiation pressure.

3. Computational Modeling Results

3.1. Predictions of System Behavior

The Reference Case model simulations provides the basis for delineating the AoR. As discussed in Section 2.2, the Reference Case reflects the understanding of the geological and hydrological conditions at the injection site, where the conceptual model is developed based on an interpretation of currently available characterization data. In the absence of site-specific measurements, assumptions are made based on nearby sites or from literature data. An injection scenario is also defined: injection of pure carbon dioxide at a constant rate of 1,200 tons per day for 15 years, followed by a 100-year redistribution period for a total simulation time of 115 years.

Sensitivity cases were developed to examine the impact of alternative injection scenarios or uncertainties in properties on the calculated AoR; these simulation results are presented in Section 3.2 below.

3.1.1. Plume Distribution

The general system behavior for the reference scenario can be described as follows. The injection well is perforated below the contact between the Vedder and the confining Freeman-Jewett formations. Consequently, carbon dioxide is injected into the uppermost sand layer of the Vedder. While some of the injected carbon dioxide is dissolved into the brine, the injection rate of 1,200 tons per day is sufficiently high so that a free phase of supercritical carbon dioxide evolves immediately after injection starts (referred to as scCO2 or simply “gas” phase). The scCO2 plume spreads out radially from the injection well, initially mainly driven by the injection overpressure. Constrained by the overlying confining layer, the plume also propagates vertically downwards into the Vedder. However, the scCO2 predominantly spreads in the horizontal direction because of the anisotropy in the sand permeability. The low permeability combined with the high gas-entry pressure of the confining layer prevents gas from entering the Freeman-Jewett formation, even if the injection pressure rises to relatively high values (see discussion below).

Farther away from the injection well, where the injection-induced pressure gradient becomes smaller, buoyancy forces become more relevant. Buoyancy forces are the result of the difference

between the relatively low density of the free-phase scCO2 (approximately 810 kg/m^3) and the aqueous phase, whose density (approximately 1,190 kg/m^3) is high due to its high salinity. Brine density is further increased by the dissolution of carbon dioxide into the aqueous phase. Buoyancy leads to an accumulation of gas immediately beneath the confining layer, increasing the gas saturation of the plume at the top of the Vedder, which further promotes horizontal spreading.

At late times, specifically after carbon dioxide injection has stopped at 15 years, capillary gradients and buoyancy become the main driving forces, and the plume continues spreading and starts migrating along the upward dip direction of the interface between the Vedder and the confining Freeman-Jewett formation. However, as the injection pressure subsides and capillary pressure gradients are reduced, the relatively weak buoyancy forces are insufficient to sustain the migration of the plume. At its leading edge, the gas phase may become discontinuous and thus trapped within the pore space (referred to as capillary or phase trapping). Carbon dioxide also continuously dissolves into the brine, and once immobilized, the volumes of discontinuous gas pockets decline, potentially below the value of the residual gas saturation, thus stopping the further advance of the carbon dioxide plume.

The processes and their interactions described here are the main factors affecting the evolution, migration, size, shape, and extent of the scCO2 plume, which is one of the criteria defining the AoR. Figure 2-6b shows the evolution of the scCO2 plume at various times including the end of injection (15 years) and during the redistribution period (40, 75 and 115 years). The contour lines represent the maximum free-phase gas saturation found within the profile at a given X-Y point. This point is found at the top of the Vedder formation, where the gas accumulates beneath the confining layer due to buoyancy effects.

After 15 years of injection, the scCO2 plume is approximately elliptical, with the slightly longer axis oriented in the north-south direction as a result of the nearby Pond-Poso Creek fault system, which is sealing and thus restricts the extension of the plume to the west. Erratic deviations from the approximate elliptical shape are the result of spatial variability in layer thicknesses, dip, and pressure distribution. The center of the plume is slightly to the east of the injection well, mainly because of the dip of the layers, which generally incline from west to east. Nevertheless, as gas flow during this initial period is dominated by the injection pressure, the plume is close to being circular and centered on the well. The plume has a diameter of less than 2 km.

During the post-injection period, the scCO2 migrates updip and to the east due to buoyancy effects. The plume spreads horizontally as the gas accumulates at the top of the Vedder and due to capillary pressure gradients at its leading edge. As a result of this spreading and equilibration, the maximum saturation values even out as the plume size increases. Note that on the receding, western side of the plume, the 5 percent contour line remains essentially stagnant, as saturation is below the residual saturation of 15 percent, i.e., the gas is trapped. Minor, localized movements of the saturation front are visible at the advancing, eastern edge of the plume, as buoyancy driven gas flow invades portions of the pore space. However, the expansion of the plume in eastern, updip direction has slowed down significantly with time as it approaches its near-steady shape and location.

After 40 years post-injection (i.e., 25 years after injection), the center of the plume has migrated eastward along the dip of the Vedder. The plume's footprint has slightly increased, whereas the size of the high-saturation region (scCO2 saturation greater than 0.3; not shown on Figure 2-6b) is somewhat reduced due to the lateral spreading and dissolution of the scCO2 into the aqueous phase.

This general evolution—eastward migration of the plume center, combined with spreading and thinning of the high-saturation zone—continues during the redistribution period (see contours after 75 and 115 years). Notably, the 0.05 contour line in the west remains stationary, as the scCO2 saturation at the receding edge of the eastwardly migrating plume becomes trapped and is therefore immobile.

3.1.2. First and Second Central Moments

To simplify the reporting of the scCO2 plume evolution, its first and second central moments are calculated as approximate measures of the plume's location and size. The first central moment yields the coordinates of the center of mass of the scCO2 plume. After subtracting the coordinates of the injection well and plotting the result as a function of time, we obtain the lateral and vertical movement of the plume. The second central moment reflects the variance. Taking the square root and multiplying by a factor of two yields is an approximate measure of the scCO2 plume's size (average extent from the plume center) along the three coordinate axes.

Figure 3-1a indicates that the center of the scCO2 plume moves approximately 150 m to the east during the 15-year injection period. It keeps migrating during the post-injection period, but becomes essentially stagnant after about 80 years, with its center approximately 450 m east and 20 m north of the injection well. The vertical upward displacement of the plume by about 50 m reflects the dip of the Freeman-Jewett confining unit, along which the center of the plume migrates upward in the eastern direction.

Figure 3-1b shows the size of the plume, which is approximately a circular disk with a horizontal radius of about 850 m and a thickness of about 100 m. The plume is essentially stable towards the end of the performance period of 115 years. Note that these composite measures from the moment analysis are a good representation of the plume size visualized in Figure 2-6b; they will therefore be used as one basis to report the results from the sensitivity analyses in Section 3.2.

3.1.3. Pressure Distribution

The injection of large amounts of carbon dioxide leads to a pressurization of the storage reservoir and surrounding formations. The magnitude and distribution of overpressures—defined as the difference between the current and initial pore pressure—are calculated to assess the risk that the integrity of the confining layer is compromised, or that nearby faults are reactivated. Moreover, brine displacement is governed by overpressure gradients.

Figure 3-2a shows the distribution of overpressures at the end of the 15-year injection period. Overpressures are highest at the injection well, from where they decline radially out. The Pond-Poso Creek fault system forms a mostly impermeable barrier, which prevents fluid flow and thus pressure propagation across the fault trace line to the west. (As a bounding calculation, the

assumption of a non-sealing Pond-Poso Creek fault is examined as part of the sensitivity analyses; see Case K in Section 3.2).

Pressure propagation is controlled by the hydraulic diffusivity, which is the ratio of permeability and total system compressibility. Overpressures thus propagate considerably farther than the free-phase scCO2 (see Figure 2-6a) or the brine it displaces. While the scCO2 plume migrates to a maximum distance of less than 2 km from the injection well, pressure perturbations travel to distances of more than 20 km in the same period. Note that the overpressure represented by the outermost contour line shown in Figure 3-2a corresponds to a head difference of 2 m. Head differences that constitute the potential for upwards brine migration are discussed in Section 4, below.

The overpressure within a 10-m radius of the injection well is 5 bars or higher. Its peak value within the well, i.e., the maximum injection pressure, depends on the well design and near-well formation properties, which are best determined by a well completion test. Such overpressures are unlikely to compromise the integrity of the sealing formation, as discussed in the Narrative permit application report. The section of the Pond-Poso Creek fault closest to the injection well experiences overpressures on the order of 3 bars. Such overpressures are unlikely to reactivate the fault, given a typical fault reactivation pressure above 20 bars (Rinaldi et al., 2015).

Figure 3-2b visualizes the evolution of the pressure field during the post-injection period (based on a minimum overpressure of 20,000 Pa or 0.2 bar or 2 m of water column head). The edge of the overpressured region slowly expands farther to the east up to about 40 years. At that time, pressure equilibration and dissipation lead to contraction of the overpressured region. After 100 years, overpressures in excess of 0.2 bar are only present in the immediate vicinity (within 1 mile) of the injection well.

Figure 3-3 shows the pressure near the injection well as a function of time (where the injection well intersects the Vedder/ Freeman-Jewett contact, i.e., at a depth of approximately 2,355 m bgs [7,725 ft bgs]). The initial, static pressure at the injection location is 259.5 bar. Instantaneous injection of carbon dioxide at a rate of 1,200 tons/day leads to a very fast pressurization at early times. However, the rate with which the pressure rises becomes smaller as soon as a free gas phase evolves that starts penetrating the formation, as the viscosity of the fluid mixture near the well decreases and the compressibility increases. After one year of injection, the pressure is slightly above 264 bar, slowly increasing to reach its maximum value of approximately 265 bar at the end of the injection period. Once carbon dioxide injection stops, the pressure rapidly declines toward the initial pressure. After 115 years, the formation remains slightly overpressured (by about 0.3 bars) because of the carbon dioxide volume added to the storage formation.

Similar curves showing pressure buildup during carbon dioxide injection and pressure decline afterwards will be used in Section 3.2 to examine the impact of variations in select input parameters on the pressure evolution during the compliance period.

3.1.4. Carbon Dioxide Phase Distribution

Figure 3-4 shows the cumulative amounts of carbon dioxide in the storage formation, separated for each phase (sequestration of carbon dioxide in mineral phases is conservatively not considered in this analysis). A total of 6.57 million metric tons of carbon dioxide are emplaced during the 15-year injection period. At the end of the injection period, 5.23 million tons are present in the free scCO2 phase, whereas 1.34 million tons are dissolved in the brine. After injection ceases, the scCO2 plume redistributes itself (see Figure 2-6b) and continues to dissolve into the aqueous phase. At the end of the 100-year post-injection period, about 64 percent (4.24 million tons) of the injected CO2 is stored in the Vedder pore space as a supercritical phase, whereas the remaining 36 percent (2.33 million tons) are dissolved in the aqueous phase. The increased dissolution percentage leads to a slight reduction in the total gas volume even though the plume has moved upward, where it encounters lower pore pressures and thus slightly expands. The final plume has a gas volume of 6.27 million cubic meters with an average scCO2 density of 804 kg/m^3.

The total pore volume of the uppermost units in the Vedder formation (Vedder sands 1, 1A, and 2), which comprise the targeted storage formation, is approximately 6×10^{10} m^3 given a porosity of 34 percent. This large value assumes that the entire pore space will be available for $scCO_2$ storage. The fraction of the pore space that can be effectively occupied by the $scCO_2$ phase depends mainly on the parameters of the relative permeability (specifically residual liquid saturation) and capillary pressure functions (see Figures 2-7 and 2-8). The calculated pore volume also depends on the size of the finite model domain. Despite these shortcomings of the volumetric approach for the estimation of storage capacity, the simulations indicate that the available pore volume is far greater than the volume of the $scCO_2$ plume (about 6.5×10^6 m^3), and the Vedder formation has sufficient storage capacity to accommodate all of the injected CO_2.

3.2. Model Sensitivity Analyses

The Reference Case is considered a sufficiently realistic representation of the hydrogeological structure and conditions at and near the proposed carbon dioxide injection site, suitable for calculating the relevant processes that help delineate the AoR based on the free-phase scCO2 plume and the associated pressure perturbations. Sensitivity analyses were performed to examine the impacts of various assumptions on the simulation results.

Table 3-1 summarizes the sensitivity cases and notes the assumptions or parameters that were changed. In most cases, only one adjustment was made at a time to unambiguously see the influence of a single parameter or assumption. The remainder of this section discusses the results of the 13 sensitivity cases. Figure 3-5 presents the extent of the plume for the base case simulation and each of the sensitivity analyses.

3.2.1. Sensitivity Cases A and B: Injection Interval

In the Reference Case, carbon dioxide is injected assuming the well is perforated between the top of the Vedder formation (elevation -2,255 meters above sea level [masl]) and the bottom of the Vedder Sand Layer 2 (elevation -2,355 masl). Given the relatively high permeability of the Vedder sands, most of the carbon dioxide enters the formation near the top of the injection

interval. In Sensitivity Case A, a second injection interval is created by perforating the well within Vedder Sand 3, between elevations -2,375 and -2,395 masl. Each interval has its own injection string, and the carbon dioxide injection rate is apportioned to each interval based on its respective transmissivity, with about 87 percent of the total rate of 1,200 tons/day injected into the upper, and 13 percent into the lower interval. In Sensitivity Case B, 100 percent of the carbon dioxide is injected exclusively into the lower interval completed in Vedder Sand 3.

Figures 3-6a through 3-6f show the scCO2 plume along west-east and south-north cross sections through the injection well from 5 to 115 years and Figure 3-7 displays the central moments of the scCO2 plume for different injection intervals. All cross sections reveal the impact of buoyancy, which leads to (a) the accumulation of scCO2 at the top of the respective injection layer (mainly visible in the south-north cross sections), and (b) the migration of the plume in updip direction (mainly visible in the west-east cross sections).

In Case A (see Panels 'b' of Figures 3-6a through 3-6f), only a small percentage of the total amount of carbon dioxide is injected into the lower reservoir (Vedder Sand 3), resulting in only minor differences in the lateral extent of the scCO2 plume, despite the fact that some of the scCO2 is stored in the lower unit.

In Case B (see Panels 'c' of Figures 3-6a through 3-6f), injection of the entire carbon dioxide mass into the relatively thin Vedder Sand 3 leads to high gas saturations and relatively high overpressures. The gas penetrates the thin overlying shale layer (Vedder Shale 2) and flows into the upper-most Vedder sand layer, where it is effectively trapped by the Freeman-Jewett confining unit. Nevertheless, the larger vertical spreading of the plume leads to a smaller lateral footprint after 115 years, as shown in Figure 3-6a through 3-6f.

Note that this gas migration from the lower to the upper storage layer in Case B is partly the result of a discretization artifact, as the steeply dipping layers west of the injection well lead to a direct horizontal connection between the Vedder Sand 3 and Vedder Sand 2, bypassing the low-permeability Vedder Shale 2 layer. This simulation thus illustrates the consequences of leakage through a breach in a thin confining shale layer within the Vedder storage formation. Similar flow and saturation patterns have been described in Doughty (2010).

3.2.2. Sensitivity Cases C and D: Permeability

In the Reference Case, the horizontal permeability (k_h) of the upper Vedder sands is determined from the geometric mean of all available data to be k_h = 254 mD, and the vertical permeability (k_v) is determined from the harmonic mean of all the data to be kv = 62 mD. Two sensitivity cases are selected based on the 75th and 25th percentiles of the distribution of measured permeabilities. In Sensitivity Case C, permeabilities are increased to k_h = 555 mD and k_v = 136 mD; in Sensitivity Case D, permeabilities are reduced to k_h = 82 mD and k_v = 20 mD.

Changing permeability of the injection formation affects both the saturation and pressure distributions. For the constant amount of injected carbon dioxide, the total scCO2 volume is relatively independent of permeability (with pressure-dependent scCO2 density having only a secondary effect). However, gas flows and spreads more readily (i.e., at a lower gas saturation) if

the permeability is higher. Consequently, the plume migration distance is longer and the footprint of the scCO2 plume is larger in Case C compared to Case D, as shown in Figure 3-8.

As expected, injecting carbon dioxide at a constant mass flow rate requires higher injection pressures if permeability is lower, as shown in Figure 3-9.

3.2.3. Sensitivity Cases E and F: Porosity

In the Reference Case, the porosity of the upper Vedder sands (θ) is taken as the median of all available data, θ = 0.34. Two sensitivity cases are selected based on the 90th and 10th percentiles of the distribution of measured porosities. In Sensitivity Case E, porosity is set to θ = 0.39; in Sensitivity Case F, porosity is set to θ = 0.26.

A larger porosity reduces the transport velocity of the injected and displaced fluid phases. Consequently, the migration distance is shorter or longer (by approximately the inverse of the porosity ratio) if porosity is increased or reduced, respectively (see Figure 3-10). Moreover, a higher porosity also provides more space for scCO2 storage in the subsurface, thus resulting in a smaller footprint of the scCO2 plume, as shown in Figure 3-10. The pressure is not significantly affected by changes in porosity. Porosity is therefore a somewhat influential parameter regarding the plume size but has a limited impact on the pressure. Also note that the influence of porosity on plume size is moderate because the uncertainty range of porosity values is relatively small.

3.2.4. Sensitivity Cases G and L: Phase Trapping

In the Reference Case, a residual gas saturation of 15 percent is specified, which leads to trapping of a portion of the free-phase scCO2 in the pore space. In Case G, the residual gas saturation is set to zero, allowing gas to remain contiguous and to flow in response to driving forces even at very low saturations. As expected, this leads to a larger migration distance along the dip of the confining unit, and a somewhat larger plume size, as shown in Figure 3-11.

In Case L, the residual gas saturation is initially zero, i.e., the gas is highly mobile during the injection phase, when the advancement of the scCO2 gas front drains brine from the pore space. However, in the post-injection phase, when brine re-imbibes the pore space, hysteresis effects lead to a location- and history-dependent increase in the residual gas saturation. The amount by which the residual gas saturation is changed depends on the saturation state after each flow reversal (between drainage and imbibition); for details, see Doughty (2013). As a result, some of the scCO2 plume becomes trapped during brine imbibition, effectively stopping the further migration and expansion of the plume. The hysteretic Sensitivity Case L thus lies between the Case G, which does not account for phase trapping, and the Reference Case.

3.2.5. Sensitivity Cases H and I: van Genuchten Parameters

The van Genuchten (1980) parameters determine the shape of the relative permeability and capillary pressure functions and thus affect (a) phase interference and resistance to flow of the aqueous and scCO2 phases, and (b) the capillary driving forces. Relative permeability and capillary pressure parameters are only relevant where two-phase (aqueous-gas) conditions prevail, i.e., within the Vedder.

The reference van Genuchten parameters are taken from Birkholzer et al. (2011; see Appendix A). Sensitivity Cases H and I examine variations to some of key van Genuchten parameters, i.e., the residual liquid saturation (Srl), the pore size distribution index (n), and the capillary strength parameter (1/α) (see Table 3-1 for chosen parameter values). Note that the influence of residual gas saturation (Srg), which affects phase trapping, has been analyzed separately in Sensitivity Cases G and L.

Figures 2-7 and 2-8 show, respectively, the relative permeability and capillary pressure curves for the three sets of van Genuchten parameters. i.e., the Reference Case and Sensitivity Cases H and I. It should be noted that all curves cross each other at various saturation points, and that higher capillary suction is correlated to lower relative permeability of the aqueous phase. Moreover, relative permeabilities vary over multiple orders of magnitude. These complexities make it difficult to predict or explain the impact of changes in van Genuchten parameters on plume behavior.

Figure 3-12 shows that changing van Genuchten parameters has a moderate impact on the evolution of the scCO2 plume. It should be noted that there is not only uncertainty in the parameters of a given relative permeability and capillary pressure curves, but also their functional form (which has not been changed in this sensitivity analysis, where only the van Genuchten curve is used). Moreover, concurrent changes in multiple van Genuchten parameters may cancel each other's effects on the shape of the curve. Nevertheless, for the three sets explored in this sensitivity analysis, the results indicate that their combined impact on plume evolution is less significant than the influence of the residual gas saturation parameter (Sgr), which governs phase trapping (see Sensitivity Cases G and L above).

Changes in van Genuchten parameters affect the flow behavior only in the two-phase region of the Vedder, i.e., where a free-phase scCO2 plume exists, whereas the distance to which a pressure perturbation propagates into the far field of the reservoir is mainly determined by the hydraulic diffusivity of the outer, fully brine saturated area. Consequently, while the choice of van Genuchten parameters impacts the well pressure during carbon dioxide injection, it has a minor effect on the extent of the overpressure zone, which determines the AoR.

3.2.6. Sensitivity Cases J and K: Fault Sealing

The injection site is relatively close to the Pond-Poso Creek fault system. The propagation of both the scCO2 plume and the pressure perturbation across the fault line is thus of interest and depends on whether these faults are sealing or non-sealing. As the analyses described in the Narrative permit application report show, the lateral sealing effectiveness critically depends on the shale gouge ratio. In the Reference Case, this ratio has been determined along the Pond-Poso Creek fault trend, and the corresponding permeability has been categorized and assigned to appropriate subsections of the fault. Note that in addition to a reduced permeability of the fault gouge, the offset across the fault also affects the lateral transmissivity available for pressure and fluid propagation, as the vertical displacement of confining layers reduce the cross-section available for horizontal fluid transport across the fault line. This effect is appropriately accounted for by the geometrical representation of the offsets, which are based on Allan diagrams.

Sensitivity Cases J and K examine the importance of this intricate treatment of the faults and their sealing properties. In Case J, the entire fault is considered sealing, with a low permeability assigned to the fault core in all directions. A fully sealing Pond-Poso Creek fault is likely prohibiting the expansion of the scCO2 plume to the west, but it may also lead to higher overpressures in the area east of the fault line. Conversely, the assumption that the Pond-Poso Creek fault is non-sealing (i.e., its fault gouge does not pose a barrier for lateral fluid transfer across the fault line) may reduce the maximum value and size of the overpressure zone but may slightly change the location and extent of the scCO2 plume.

While the sealing properties of the fault do not have significant impact on the location, shape, and size of the scCO2 plume, Figure 3-13 shows that the horizontal sealing properties of the nearby Pond-Poso Creek fault impact pressure propagation, as expected. In particular, a non-sealing fault would allow some of the pressure to dissipate to the west, lowering the maximum injection pressure. The results of the Reference Case, which uses different sealing properties to individual subsections of the fault, are very similar to those based on the assumption that the Pond-Poso Creek fault is completely sealing.

3.2.7. Sensitivity Case M: Boundary Conditions

In the Reference Case, the vertical outer boundaries of the model are open, with pressures fixed according to the hydrostatic profiles established during model initialization. In Case M, no-flow boundaries were imposed along all outer boundaries of the model domain. This is an unrealistic configuration, as there are no hydrogeological features (such as sealing faults or water divides) that would impose such boundary conditions. It is conceived as a bounding case for the purpose of demonstrating that the outer boundaries of the model domain have no undue impact on the simulation results.

Figure 3-14 confirms that the calculated pressure is only very slightly increased by closing all outer boundaries, with the hydrostatic assumption used in the Reference Case considered more realistic. There is no discernable impact of the outer boundary conditions on the scCO2 plume evolution.

4. <u>AoR Delineation</u>

4.1. Critical Pressure Calculations

AoR delineation was based on the methods of Nicot et al. (2008), which is also referenced in the U.S. EPA AoR and Corrective Action Guidance. First, the following equation was used (Eq-1):

$$\frac{\Delta P}{g} = (z_v - z_I)\left(\frac{\lambda - \xi}{2}(z_v - z_I) + \rho_{I,\lambda} - \rho_I\right)$$

where ΔP is the admissible overpressure that can be sustained before fluid in the injection zone would flow into a USDW through a hypothetical open conduit "threshold overpressure" due to

density differentials in the injection zone and USDW, g is acceleration due to gravity, z_v is the elevation of the injection zone, z_i is the lowermost elevation of the USDW, λ is a linear coefficient that describes the density gradient in the wellbore at a constant total dissolved solids (TDS), ξ is a linear coefficient that describes the initial density gradient in the borehole, $\rho_{I,\lambda}$ represents the density of fluid in the wellbore at the depth of the USDW after increased pressure has moved denser brine into the wellbore, and ρ_I is the initial density in the wellbore at the depth of the USDW. Equation 1 assumes that pressure increase is slow enough for the fluid to equilibrate thermally with its surroundings, and that additional pressure has to be balanced by the increase in density of the water column in the well bore.

Critical pressure necessary to drive formation fluids into an overlying USDW also accounted for pressure necessary to overcome gel strength of water-based drilling muds consistent with methods given in Nicot et al. (2008), Barker (1981), and Johnston and Knape (1986). U.S. EPA UIC program has previously approved accounting for gel strength for calculation of the allowable pressure buildup that defines the AoR, for example in approval of a hazardous waste injection restriction exemption reissuance in Mississippi (GKS, 2018). Rotary drilling includes use of drilling muds that are left in place when the well is abandoned. Well abandonment in the vicinity of the project, going back to the early drilling in the early 1900s included documenting that the well was filled with heavy mud when abandoned (e.g., see records for well 0402930603).

Water-based drilling muds develop a gel structure, and conservatively assuming an open borehole the pressure due to gel strength (P_g) is given by (Eq-2):

$$P_g = \frac{0.00333 \cdot G \cdot h}{d}$$

where G is the gel strength (lb/100ft^2), d is borehole diameter (inches), h is the formation depth, and 0.00333 is a conversion factor so that P_g is given in units of pounds per square inch (psi). G is conservatively assumed to be 25 lb/100ft^2 (Nicot et al., 2008), h is taken as the depth of the Vedder formation at any given location, and borehole diameter was assumed to be 16 inches based on review of local abandoned well logs. Final allowable overpressure is the sum of ΔP (Equation-1) and P_g (Equation-2).

Appendix B presents threshold overpressure calculations at example locations within the vicinity shown on Figure 3-2a. Injection zone and USDW elevations are based on the digital model grid and USDW delineations presented in the Narrative permit application report. TDS is based on salinity mapping also presented in the narrative permit application report. Linear coefficients are calculated based on density as a function of temperature and salinity using standard methods as given in Appendix B. Threshold admissible pressure is calculated to be 420,000 Pa at the injection well location.

Admissible pressure increase at all locations within the TOUGH domain was delineated by applying Equations 1 and 2 at each TOUGH model grid location based on the specific salinity, USDW elevation, and injection-zone formation elevations at each model grid cell location. The resulting area greater than admissible pressure was determined by comparing the simulated Vedder formation overpressure at 15 years after injection begins (time of maximum pressure at

the injection well location) to the admissible pressure at each location (Figure 4-1). The area with greater than admissible pressure at 15 years is limited to within approximately 0.5 miles of the injection well and has a smaller footprint than the carbon dioxide plume. Overpressure was also evaluated at 20 and 40 years after injection begins (5 and 25 years after injection ends), and in both cases there were no areas with greater than admissible pressure (due to pressure decline at the location of the injection well and vicinity, see Figure 3-3).

4.2. AoR Delineation

The AoR encompasses the maximum extent of the carbon dioxide plume and area of elevated pressure that may endanger USDWs (U.S. EPA, 2013). As discussed in Section 4.1, pressure calculations demonstrate that the injection project will not cause pressure increases sufficient to endanger USDWs outside of the footprint of the carbon dioxide plume (Figure 4-1). Therefore, the AoR is given by the outermost carbon dioxide plume simulated in TOUGH modeling as shown on Figure 4-1 (defined as the 0.05 carbon dioxide saturation contour 115 years after the beginning of injection). The AoR is 1.49 square miles.

5. Corrective Action

No abandoned wells or wells that penetrate the confining system are present within the AoR based on review of CalGEM records. Figure 4-2 shows abandoned oil and gas wells within the vicinity of the project and AoR. Because no wells are present that penetrate the confining system, corrective action is not necessary prior to the commencement of injection.

6. Reevaluation Schedule and Criteria

Consistent with U.S. EPA regulations and guidance, the AoR will be reevaluated at a fixed frequency of once every five years during the injection and post-injection periods and under additional conditions as described below:

- After injection well construction and pre-injection testing and logging, to incorporate additional geologic information obtained from core analyses and additional injection well tests
- Identification of new Site data from any monitoring activities that indicate the presence of previously unidentified faults, fractures or abandoned wells that penetrate the confining zone
- Significant changes in site operations that may alter model predictions and the AoR delineation, including
    - At least a 15% increase from permitted injection rates averaged over a 3-month period
    - Any switch from injection in the upper Vedder units (assumed in the baseline scenarios) to the Vedder 3 unit

  - Exceedance of fracture pressure conditions

- Monitoring results for the injected carbon dioxide plume and/or the associated pressure front that differ significantly from model predictions, including:
  - Measured pressure at the injection and/or monitoring wells that exceeds model simulations at the corresponding depth and time period by at least 25%
  - Carbon dioxide plume movement further than model predictions by at least 25% distance from the injection well
- New site characterization data obtained that may significantly change model predictions and the delineated AoR.
- Initiation of additional injection projects within the Vedder formation within a 1- mile radius of the injection well;
- Significant land-use changes that would impact site access;
- A compromise in injection well mechanical integrity;
- Any seismic event greater than M 3.5 within 5 miles of the injection well; and
- Any other activity prompting a model recalibration as directed by the U.S. EPA.

AoR reevaluations will occur within 6 months of the events listed above. AoR reevaluation will consist of adjusting model parameters based on any newly obtained information (e.g., newly collected permeability values); and adjusting model parameters to match observed pressure and carbon dioxide saturation data collected during monitoring activities listed in the Testing and Monitoring Plan. Reporting of the revised AoR will include:

- All model attributes, as given in Section 3.5 of the U.S. EPA AoR and Corrective Action guidance document, will be re-submitted to the UIC Program Director. In addition, the model calibration process and final AoR delineation results will be presented in detail as part of the submission;
- Adjusted input parameter values listed;
- Graphs comparing observed and modeled values of carbon dioxide migration and fluid pressure;
- Model results showing carbon dioxide and pressure front migration over time included; and
- Value of the model calibration statistics
- Newly delineated AoR presented on maps that highlight similarities and differences in comparison with previous AoR delineations.

- Amended AoR and Corrective Action Plan and amendments to related project plans, including any maps presented in the permit application with an overlay of the AoR.

SJR will report to U.S. EPA if it determines that no updates to any of the project plans are needed based on the results of an AoR reevaluation, and the basis for such a determination.

References

Barker, S.E. 1981. Determining the area of review for industrial waste disposal wells. Presented to the Faculty of the Graduate School of the University of Texas at Austin in Partial Fulfillment of the Requirements for the Degree of Masters in Science in Engineering. December 1981.

Doughty, C. A., 2013. User's guide for hysteretic capillary pressure and relative permeability functions in TOUGH2. No. LBNL-6533E. Lawrence Berkeley National Lab.(LBNL), Berkeley, CA (United States), 2013.

Doughty, C., 2010. Investigation of CO2 plume behavior for a large-scale pilot test of geologic carbon storage in a saline formation, Transp. Porous Med., 82, 49–76, 2010.

Fetter, 2001. Applied Hydrogeology, 4th Edition.

Finsterle, S., 2021. iTOUGH2-EOS1nT: A Nonisothermal Two-Phase Flow Simulator for Water and Multiple Tracers User's Guide. Finsterle GeoConsulting, Kensington CA, July, 19 2021.

Finsterle, S., Commer, M., Edmiston, J. K., Jung, Y., Kowalsky, M. B., Pau, G. S. H., ... & Zhang, Y. (2017). iTOUGH2: A multiphysics simulation-optimization framework for analyzing subsurface systems. Computers & Geosciences, 108, 8-20.

Geostock Sandia, LLC (GKS), 2018. Chemours DeLisle Plant 2017 HWDIR Exemption Petetion Reissuance Application, Section 4.0 Area of Review. September 2018.

Haukwa, 1998. AMESH - A mesh creating program for the integral finite difference method: A User's Manual. LBNL, Earth Sciences Division.

Johnston, O. C., and B. K. Knape, 1986, Pressure Effects of the Static Mud Column in Abandoned Wells, Texas Water Commission LP 86-06 [0110880].

Nicot, J.-P., Oldenburg, C.M., Bryant, S.L., Hovorka, S.D., 2008. Pressure perturbations from geologic carbon sequestration: Area-of-review boundaries and borehole leakage driving forces: presented at the 9th International Conference on Greenhouse Gas Control Technologies (GHGT-9), Washington, D.C., November 16-20, 2008. GCCC Digital Publication Series #08-03h.

Pruess, K., C. Oldenburg, and G. Moridis, 2012. TOUGH2 User's Guide, Version 2.1, Report LBNL-43134, Lawrence Berkeley National Laboratory, Berkeley, Calif., 2012.

Pruess, K. (2005). ECO2N: A TOUGH2 fluid property module for mixtures of water, NaCl, and CO2 (p. 76). Berkeley, CA: Lawrence Berkeley National Laboratory.

Pruess, K., J. Garcia, T. Kovscek, C. Oldenburg, J. Rutqvist, C. Steefel, and T. Xu. 2004. Code intercomparison builds confidence in numerical simulation models for geologic disposal of CO2. Energy 29:1431–1444.

Rinaldi, A.P., V. Vilarrasa, J. Rutqvist and F. Cappa. 2015. Fault reactivation during CO2 sequestration: Effects of well orientation on seismicity and leakage. Greenhouse Gas Sci Technol. 5:645–656 (2015); DOI: 10.1002/ghg

Spycher, N., Pruess, K., & Ennis-King, J. (2003). CO2-H2O mixtures in the geological sequestration of CO2. I. Assessment and calculation of mutual solubilities from 12 to 100 C and up to 600 bar. Geochimica et cosmochimica acta, 67(16), 3015-3031.

U.S. Environmental Protection Agency (U.S. EPA), 2013. Geologic Sequestration of Carbon Dioxide, Underground Injection Control (UIC) Program Class VI Well Area of Review Evaluation and Corrective Action Guidance. EPA 816-R-13-005.

Van Genuchten, M. T. (1980). A closed-form equation for predicting the hydraulic conductivity of unsaturated soils. Soil science society of America journal, 44(5), 892-898.

Figures

List of Figures

2-1 Mesh Plan View
2-2 Mesh Expanded View, Radial Portion
2-3 Mesh Enlarged View, Intersections of the Pond-Poso Creek Faults
2-4 Mesh Enlarged View, Jasmin fault elements and intersections
2-5 Materials, Permeability and Porosity Cross Sections, TOUGH2 Model
2-6a TOUGH2 simulated maximum carbon dioxide saturation, base case (Expanded View)
2-6b TOUGH2 simulated maximum carbon dioxide saturation, base case (Local View)
2-7 Relative permeability of the aqueous phase and scCO2 phase
2-8 Capillary pressure functions

3-1a Central moments of scCO2 plume for Reference Case (First Moment)
3-1b Central moments of scCO2 plume for Reference Case (Second Moment)
3-2a TOUGH2 simulated maximum overpressure, base case (15 years)
3-2b TOUGH2 simulated maximum overpressure, base case (15 years to 115 years)
3-3 Average pressure within a 10-m radius of the injection well, base case
3-4 Cumulative CO_2 stored in supercritical gas phase and dissolved in brine
3-5 TOUGH2 simulated maximum carbon dioxide saturation, base case and sensitivity runs, Upper Vedder and Vedder 3 response
3-6a Comparison of scCO2 Saturation Profiles in West-Eastern and South-Northern Directions (5 years)
3-6b Comparison of scCO2 Saturation Profiles in West-Eastern and South-Northern Directions (10 years)
3-6c Comparison of scCO2 saturation profiles in west-eastern and south-norther directions (15 years)
3-6d Comparison of scCO2 saturation profiles in west-eastern and south-norther directions (40 years)
3-6e Comparison of scCO2 saturation profiles in west-eastern and south-norther directions (75 years)
3-6f Comparison of scCO2 saturation profiles in west-eastern and south-norther directions (115 years)
3-7 Central moments of scCO2 plume for different injection intervals

3-8 Central moments of scCO2 plume for permeability sensitivity cases
3-9 Average pressure within a 10-m radius of the injection well for permeability sensitivity cases
3-10 Central moments of scCO2 plume for porosity sensitivity cases
3-11 Central moments of scCO2 plume for different phase trapping mechanisms
3-12 Central moments of scCO2 plume for different sets of van Genuchten parameters
3-13 Average pressure within a 10-m radius of the injection well, fault sealing sensitivity cases
3-14 Average pressure within a 10-m radius of the injection well, boundary condition sensitivity analyses

4-1 AoR Delineation
4-2 AoR Delineation and Oil and Gas Wells

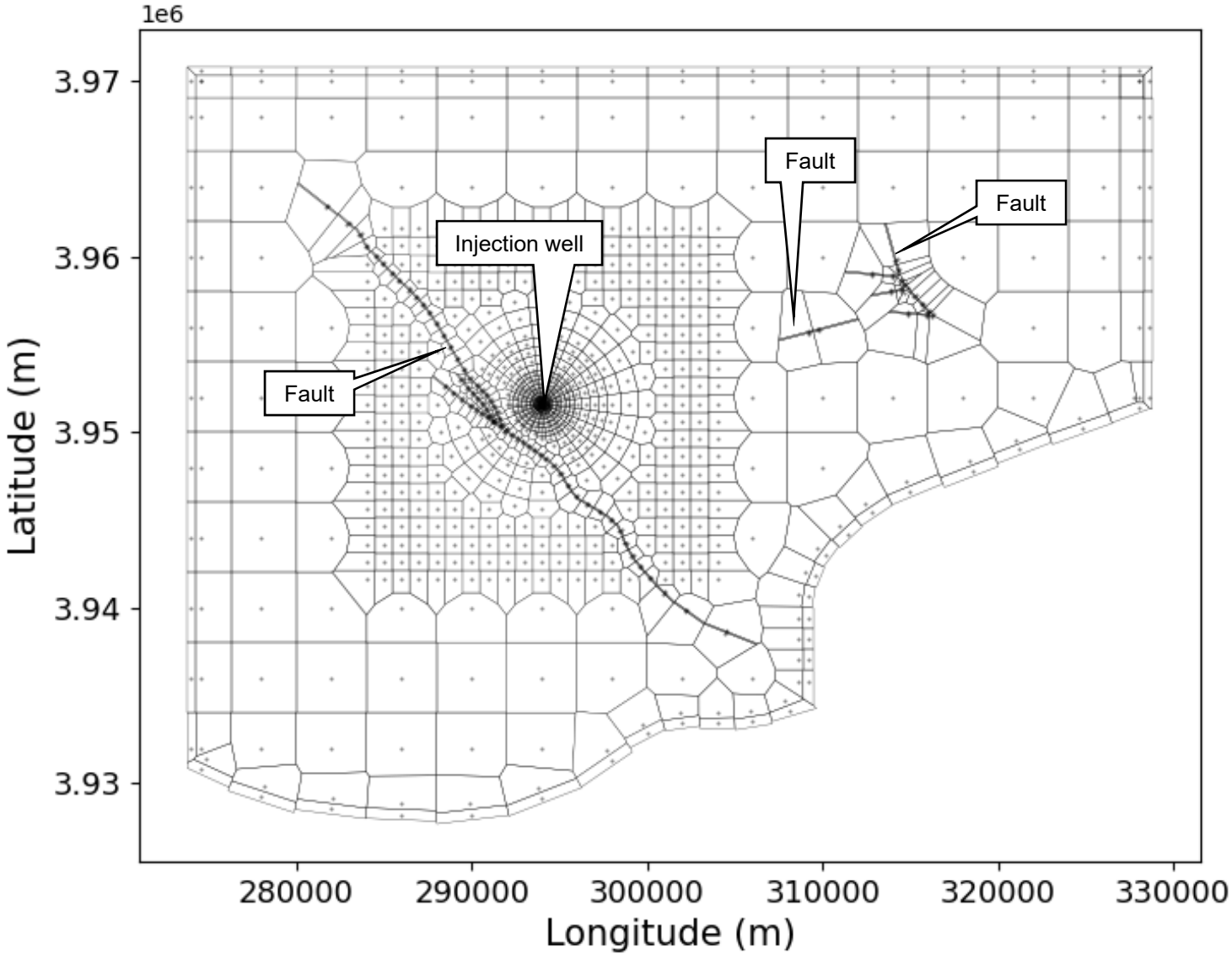

Notes: Plan view of the 3-D mesh used in the TOUGH2 simulations presented in this report, which includes faults embedded in a background mesh containing radial and Cartesian regions and thin boundary elements on the north, south, east, and west boundaries.

SAN JOAQUIN RENEWABLES

Mesh Plan View

Figure 2-1

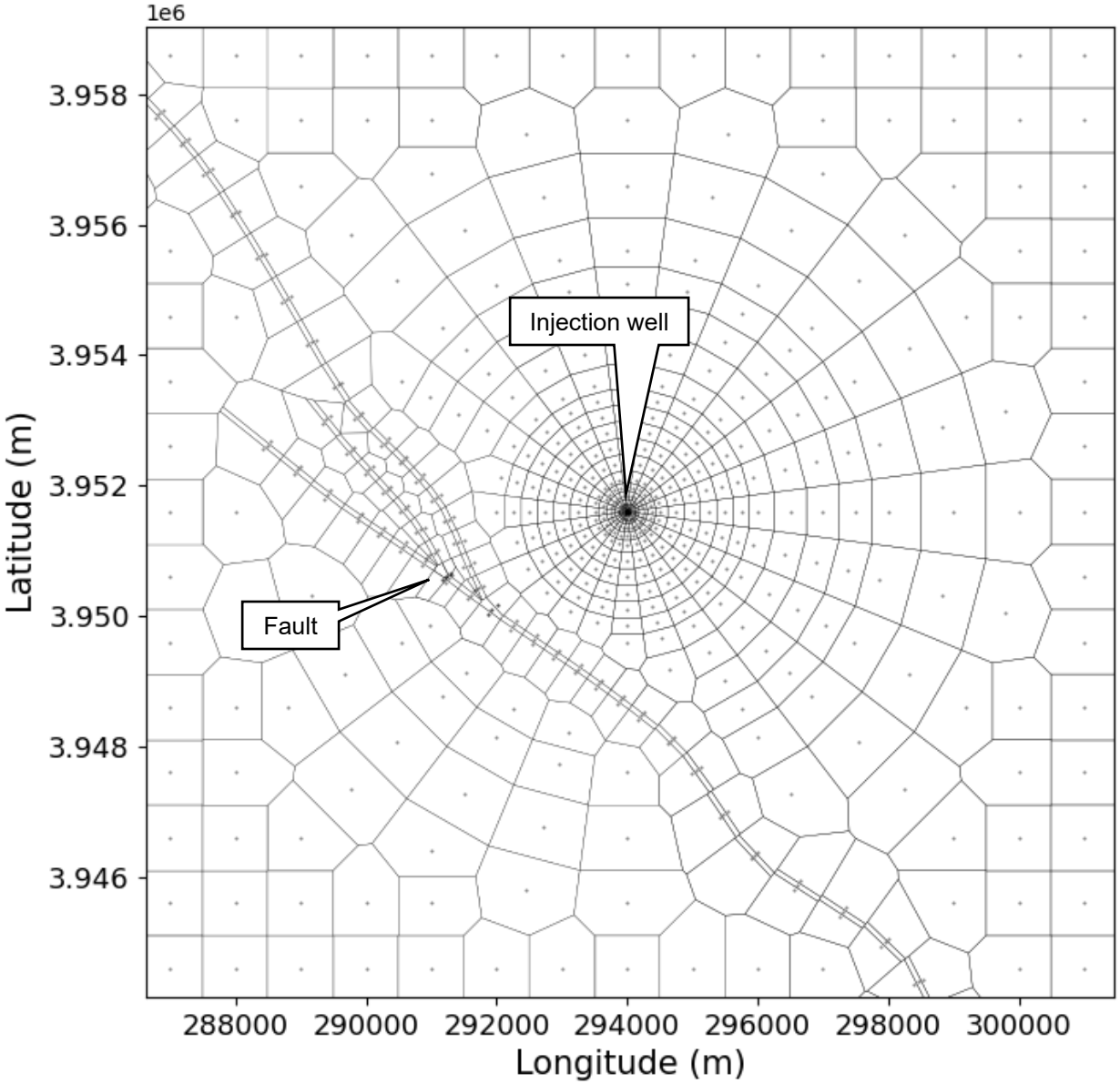

SAN JOAQUIN RENEWABLES

Mesh Expanded View, Radial Portion

Figure 2-2

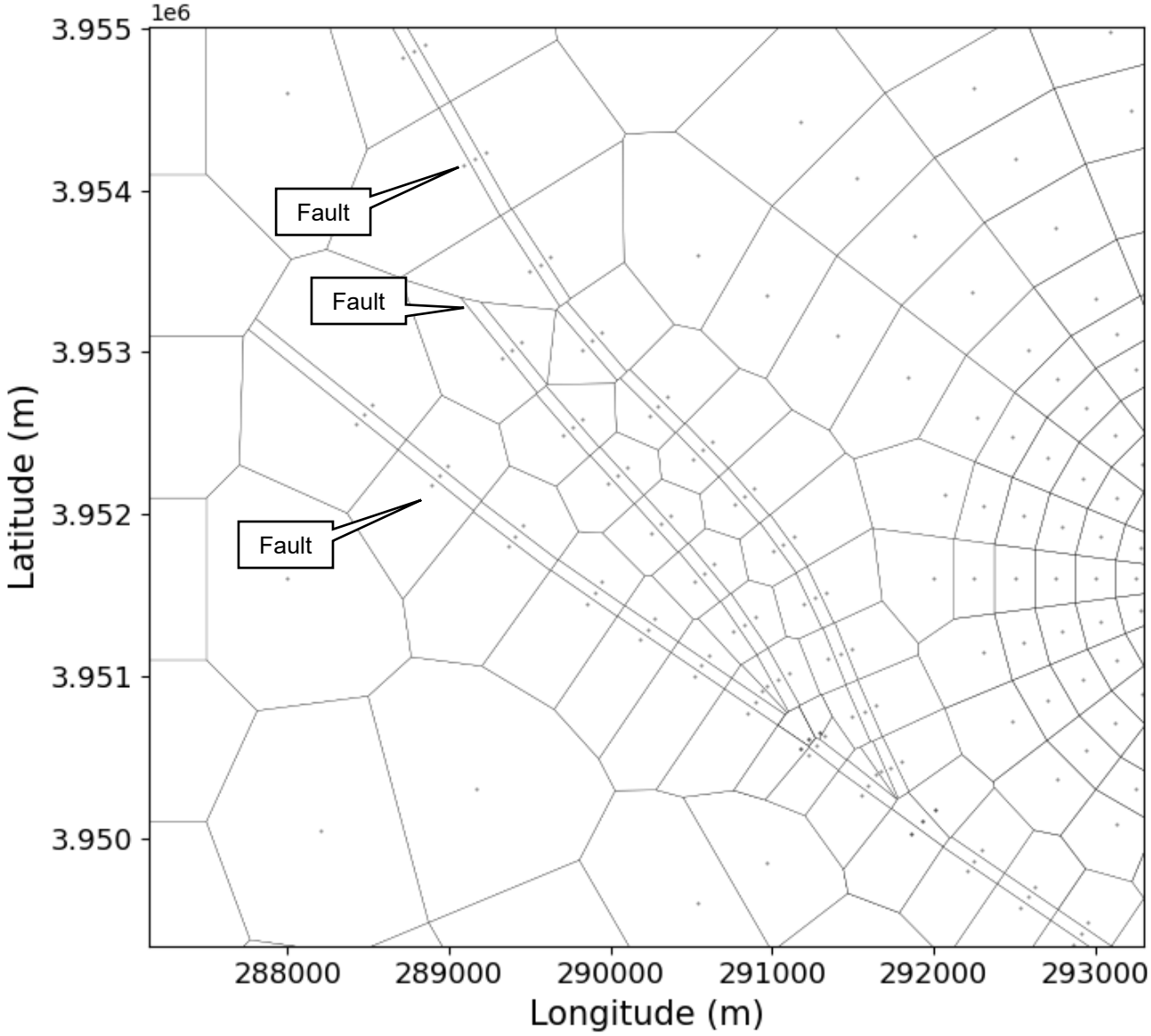

SAN JOAQUIN RENEWABLES

Mesh Enlarged View, Intersections of the Pond-Poso Creek Faults

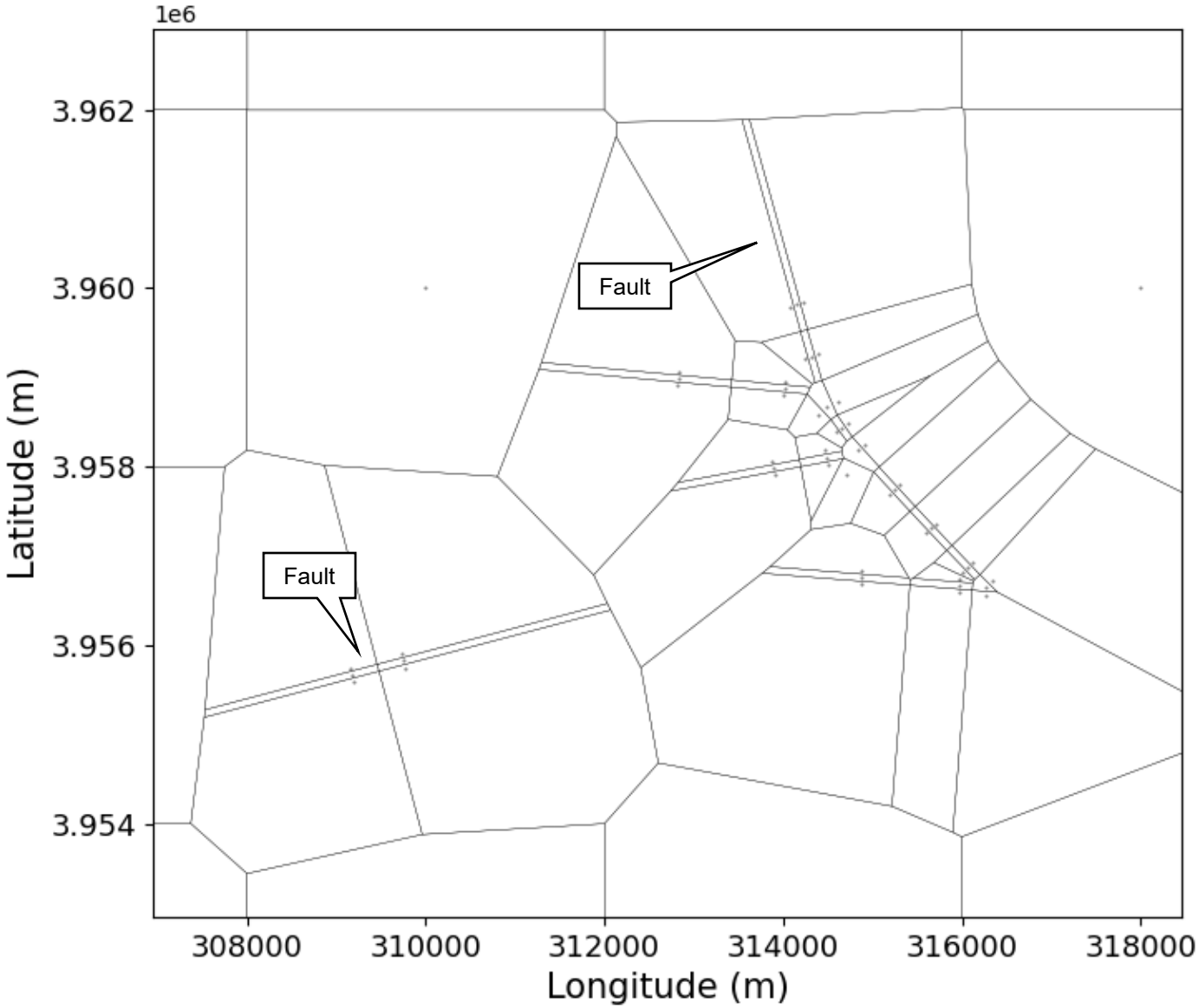

SAN JOAQUIN RENEWABLES

Mesh Enlarged View, Jasmin Fault Elements and Intersections

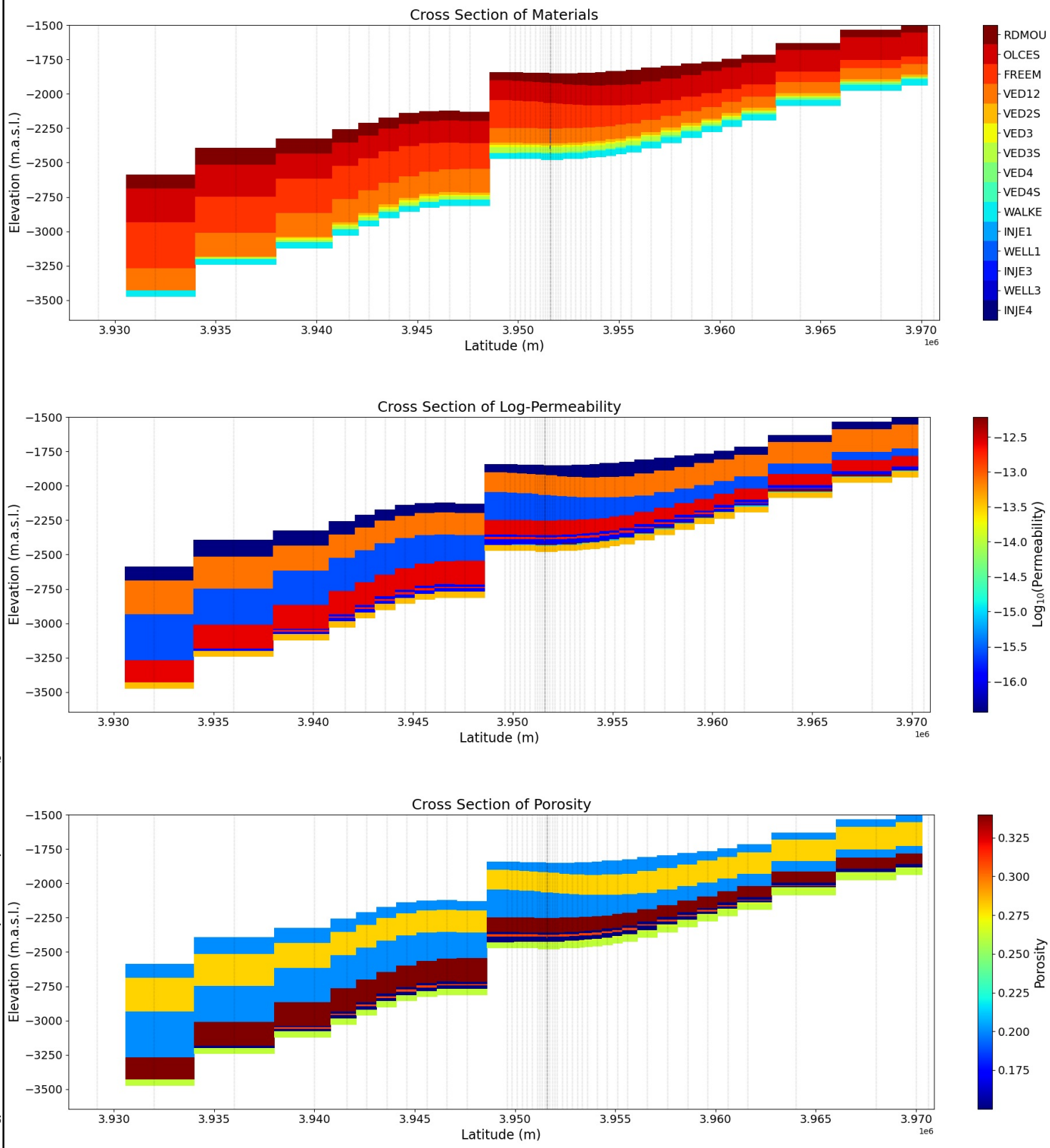

S:\Projects\DB19.1252_Frontline_Bioenergy\GIS\QGIS\2-5 Materials, Permeability, and Porosity Cross Sections.qgz

SAN JOAQUIN RENEWABLES

Materials, Permeability, and Porosity Cross Sections, TOUGH2 Model

08/11/2022 JN DB19.1252

Figure 2-5

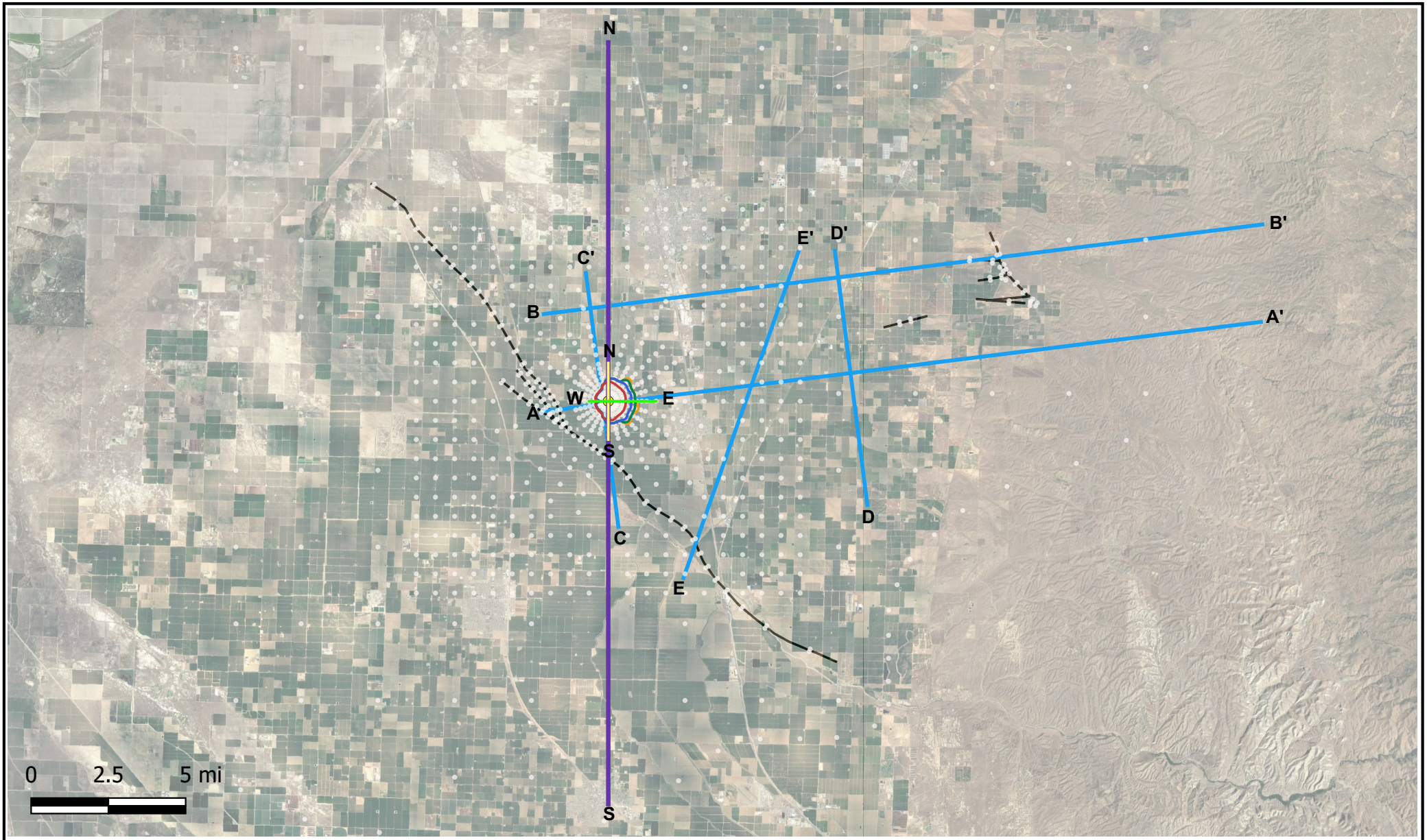

Explanation

- 15-Year
- 40-Year
- 75-Year
- 115-Year
- Injection Well
- TOUGH2 Elements
- Geologic Cross-Sections
- Faults at Vedder

TOUGH2 Model Cross sections

- Materials Distribution north-south
- Saturation Profiles Section west-east
- Saturation Profiles Section north-south

N

Note: Contour lines represent 0.05 simulated carbon dioxide saturation (dimensionless).

SAN JOAQUIN RENEWABLES

TOUGH2 simulated maximum carbon dioxide saturation base case (Expanded View)

S:\Projects\DB19.1252_Frontline_Bioenergy\Analysis\TOUGH\Figures\Frontline_Case0_Final_SatGas_ViewA.qgz

08/16/2022 JN DB19.1252

Figure 2-6a

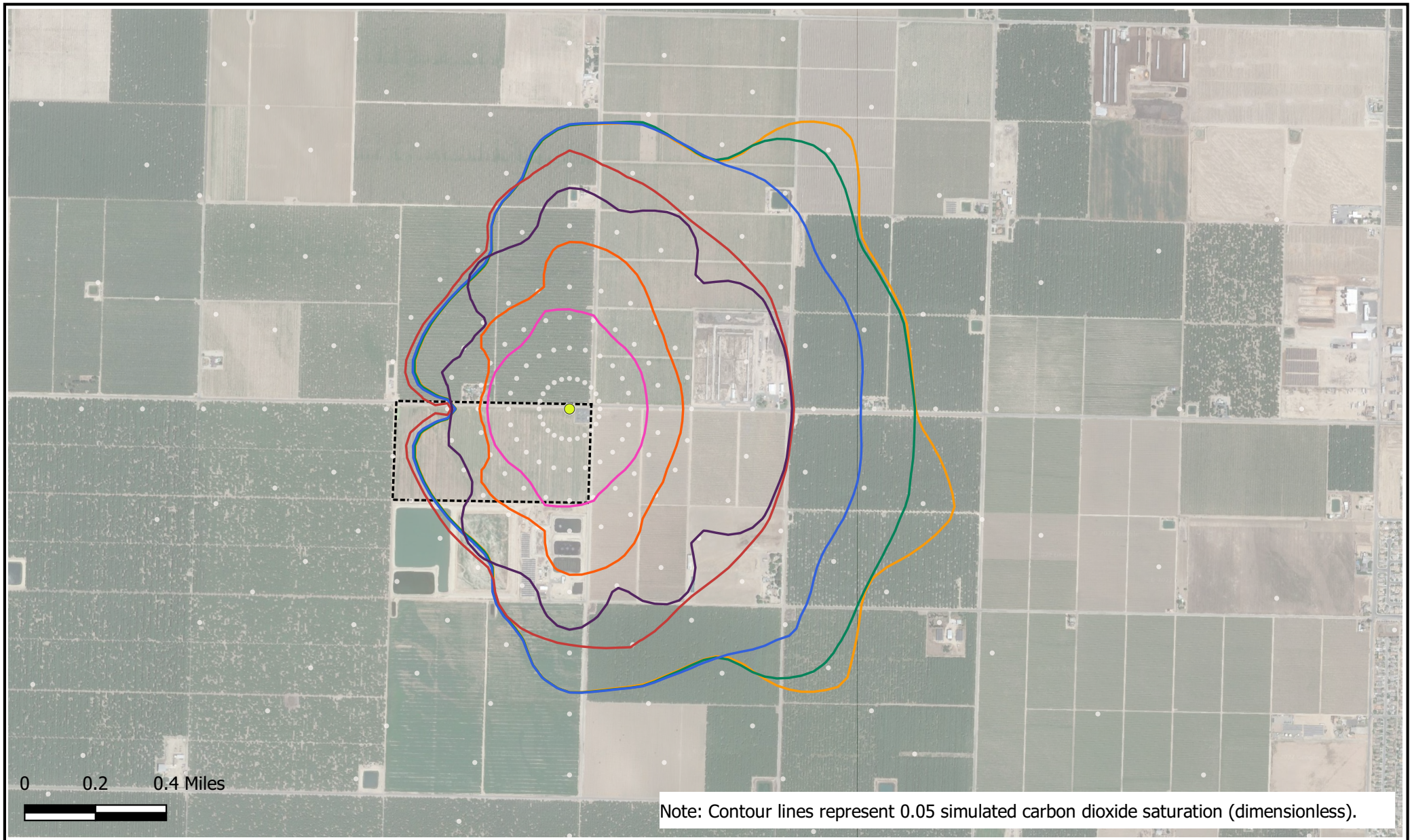

Explanation

- Case0_2yr_CO2-Sat
- Case0_5yr_CO2-Sat
- Case0_10yr_CO2-Sat
- Case0_T15_SatGas
- Case0_T40_SatGas
- Case0_T75_SatGas
- Case0_T115_SatGas
- Injection Well
- TOUGH2 Elements
- Frontline Property Boundary

N

SAN JOAQUIN RENEWABLES

TOUGH2 simulated maximum carbon dioxide saturation, base case (Local View)

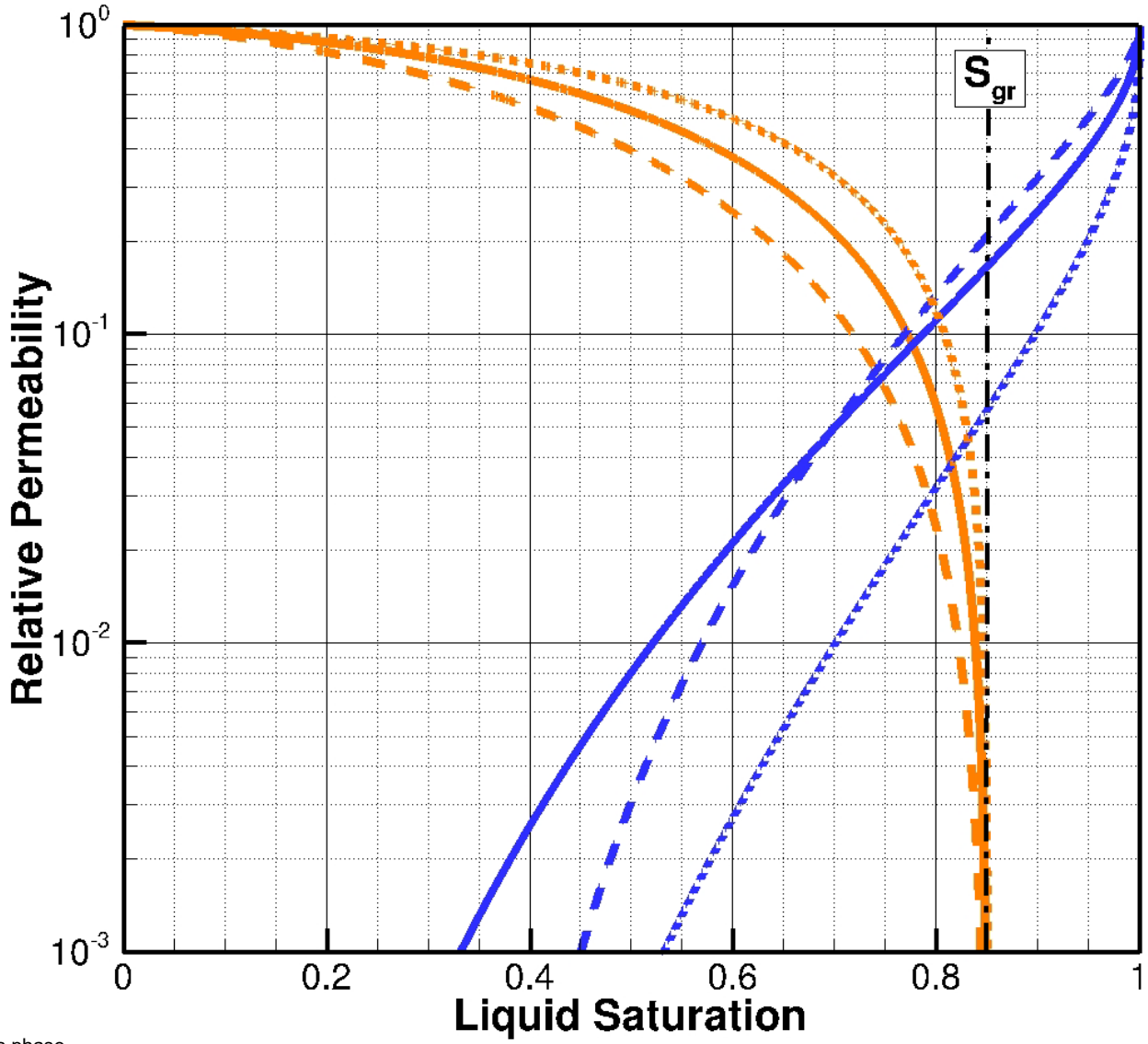

Notes:
Blue line = aqueous phase
Orange line = $scCO_2$ phase
Solid line = Reference case
Dash line = Case H
Dotted line = Case I

SAN JOAQUIN RENEWABLES

Relative Permeability of the Aqueous Phase and $scCO_2$ Phase

Figure 2-7

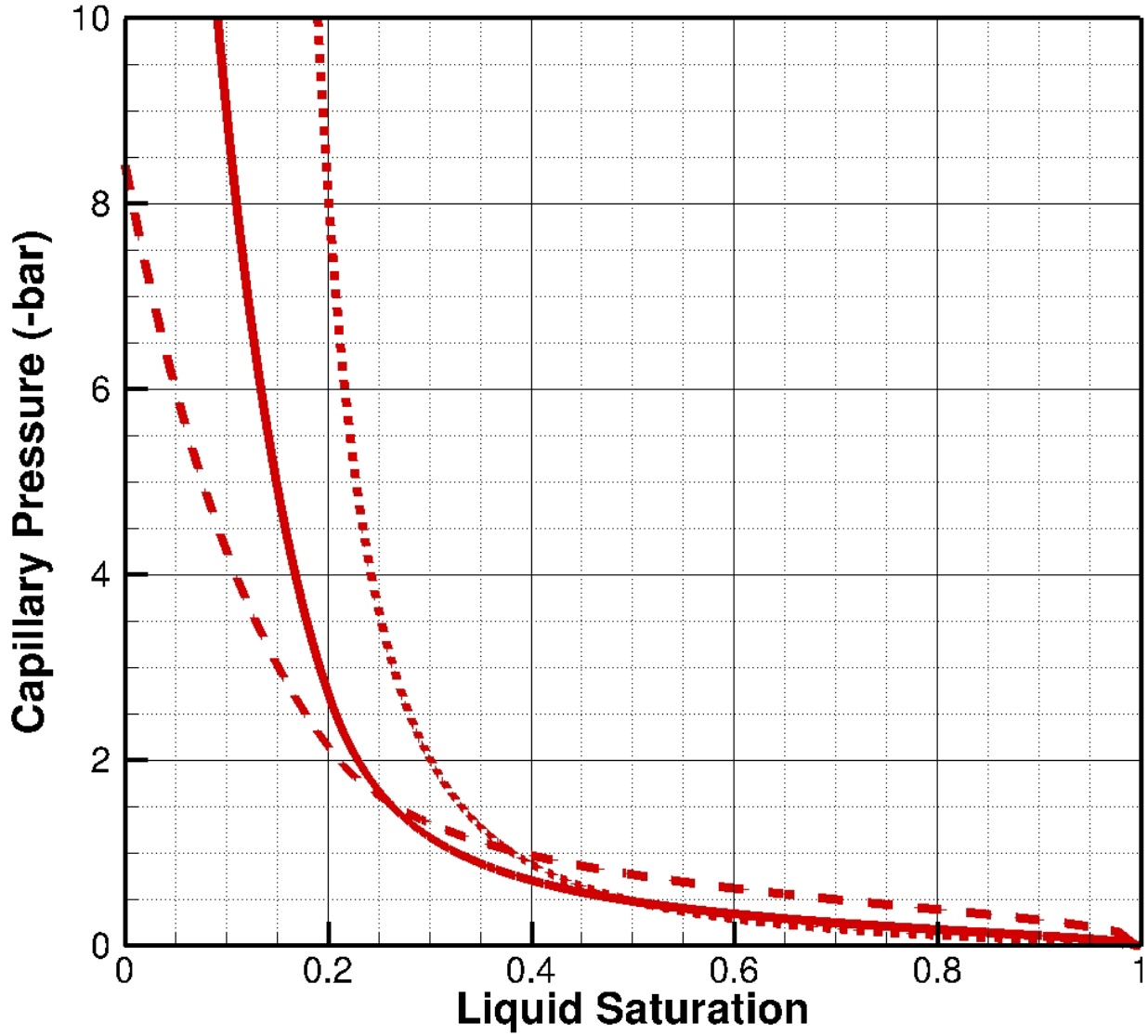

Notes:
Solid line = Reference case
Dash line = Case H
Dotted line = Case I

SAN JOAQUIN RENEWABLES

Capillary Pressure Functions

Figure 2-8

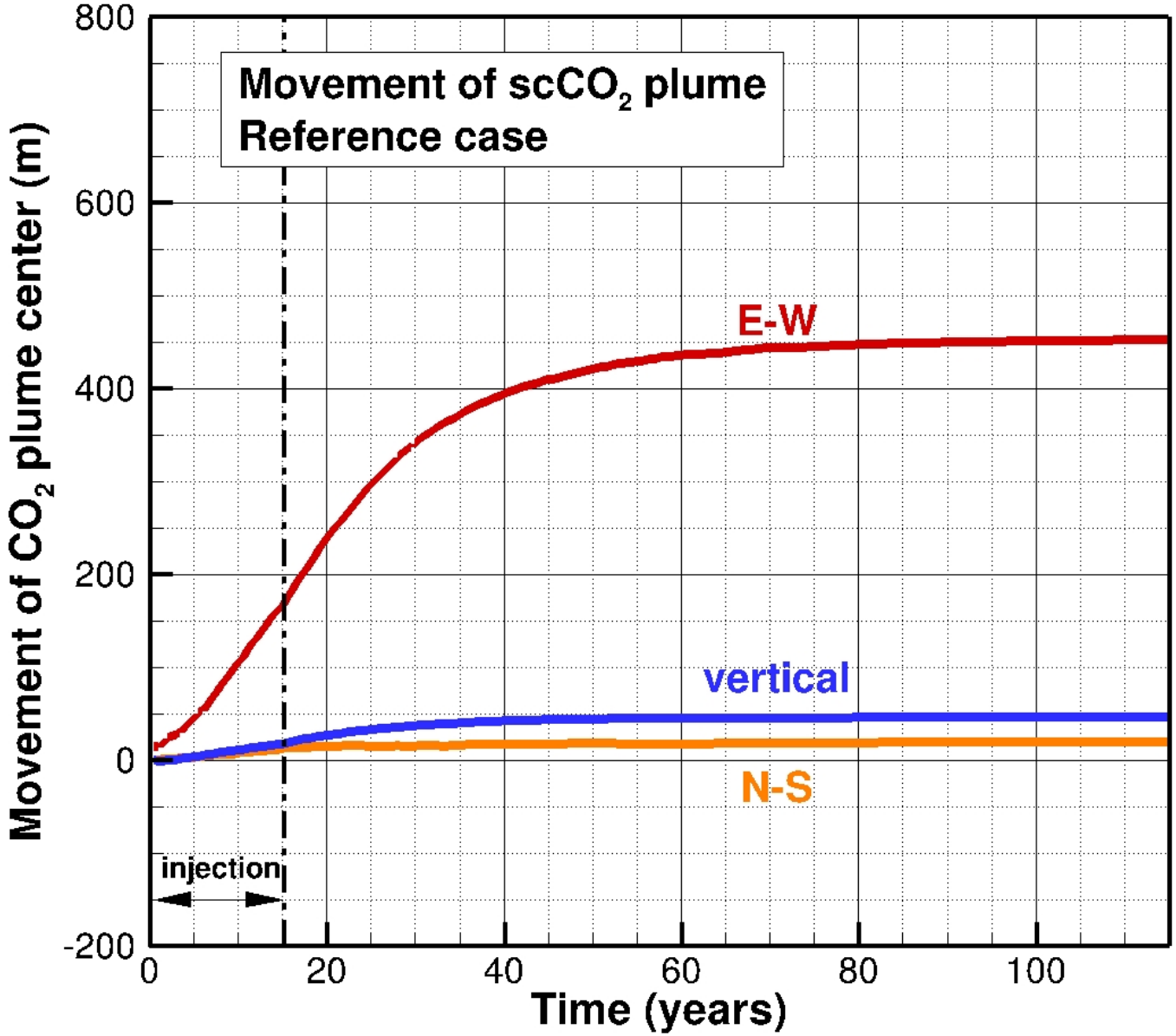

Note: The first moment indicates the migration of the center of mass of the scCO2 plume away from the injection well.

FRONTLINE BIOENERGY

Central Moments of scCO2 Plume for Reference Case (First Moment)

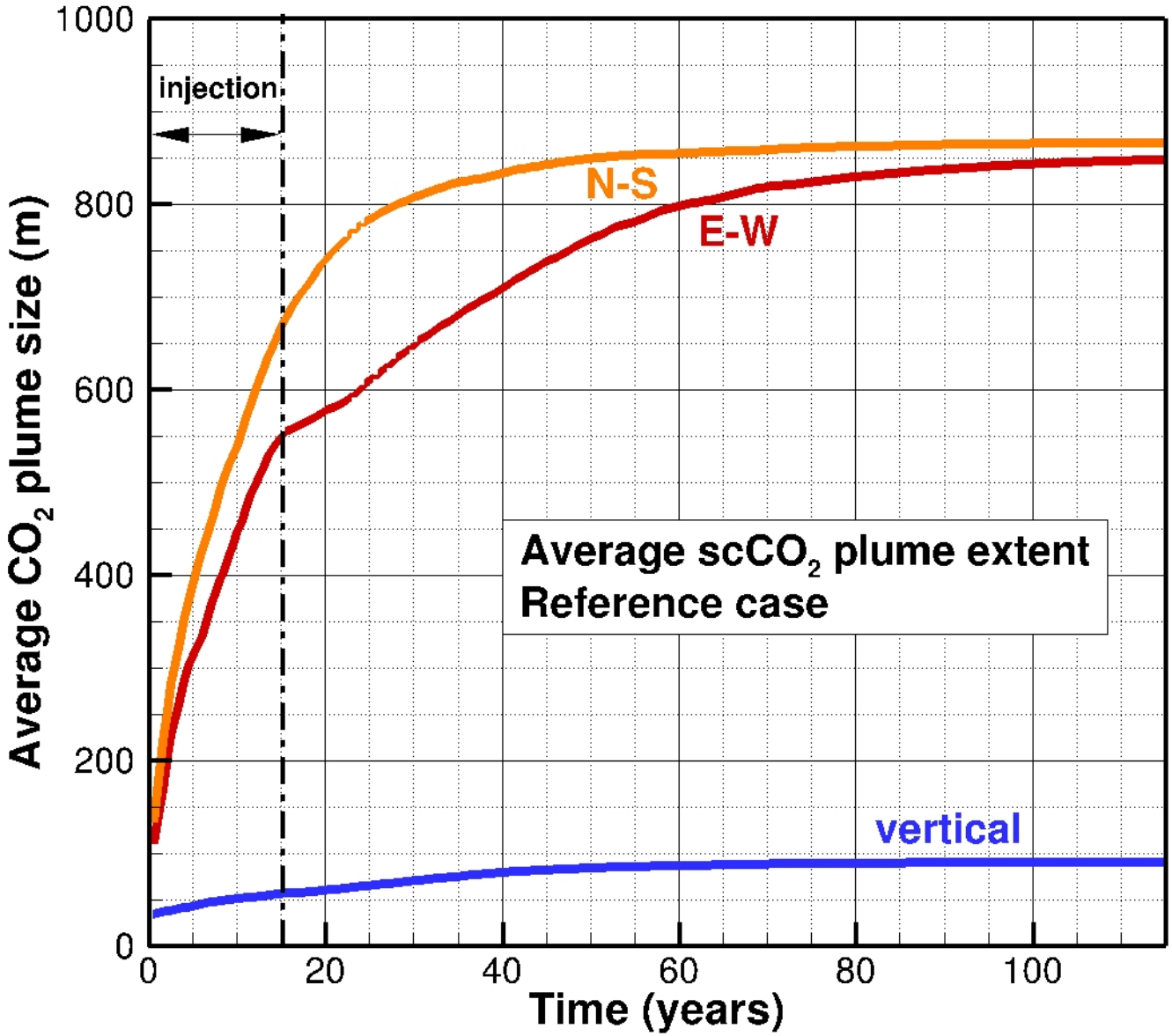

Note: The second moment indicates the average extent of the scCO2 plume.

FRONTLINE BIOENERGY

Central Moments of scCO2 Plume for Reference Case (Second Moment)

Figure 3-1b

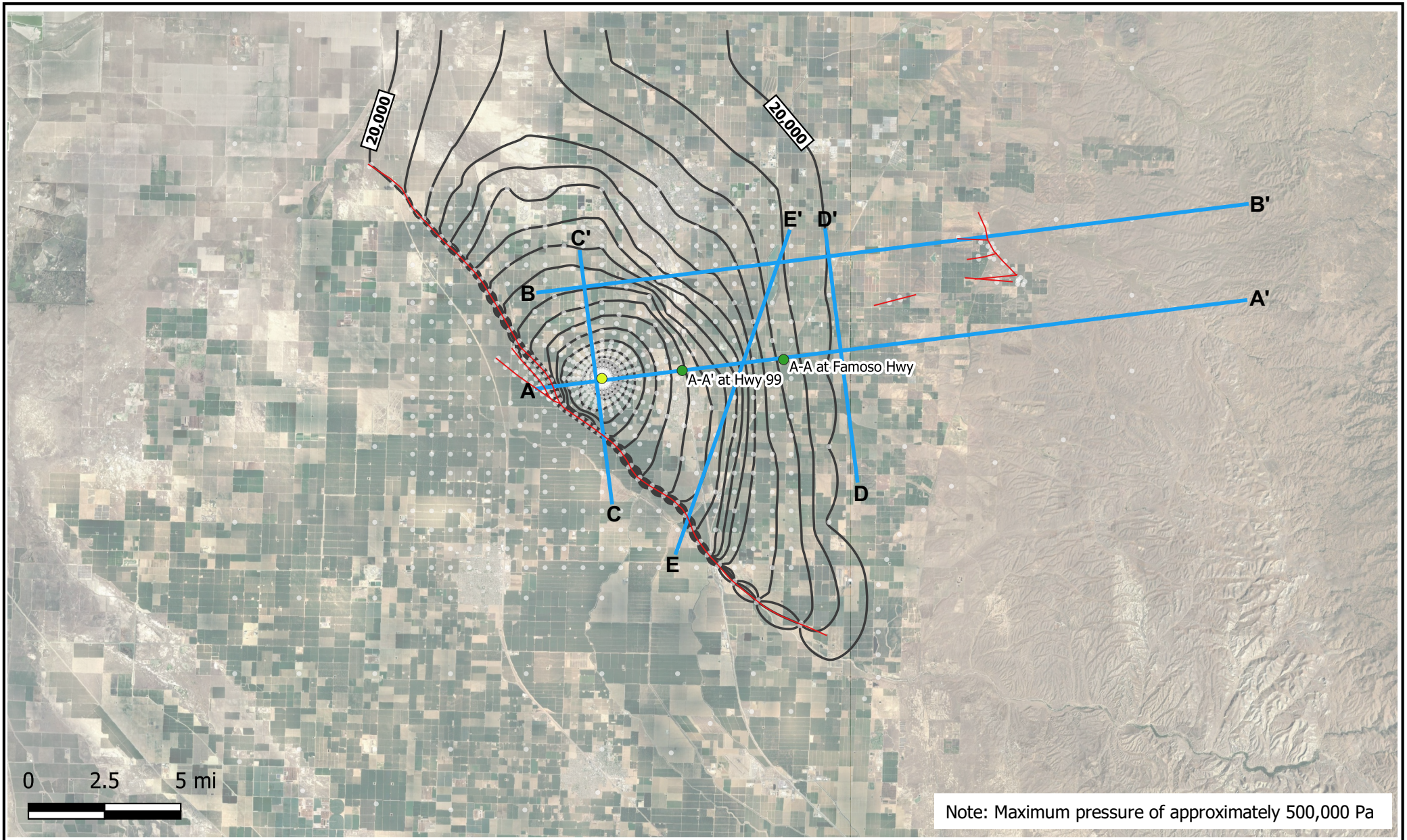

Explanation

- Maximum Pressure Increase, 20,000 Pa Interval
- Cross Sections
- Injection Well
- 20,000 Simulated Pressure Increase (Pa)
- TOUGH2 Elements
- Faults at Vedder

N

SAN JOAQUIN RENEWABLES

TOUGH2 simulated maximum overpressure, base case (15 years)

S:\Projects\DB19.1252_Frontline_Bioenergy\Analysis\TOUGH\Figures\Frontline_Case0_Final_DeltaPress.qgz

08/16/2022 JN DB19.1252

Figure 3-2a

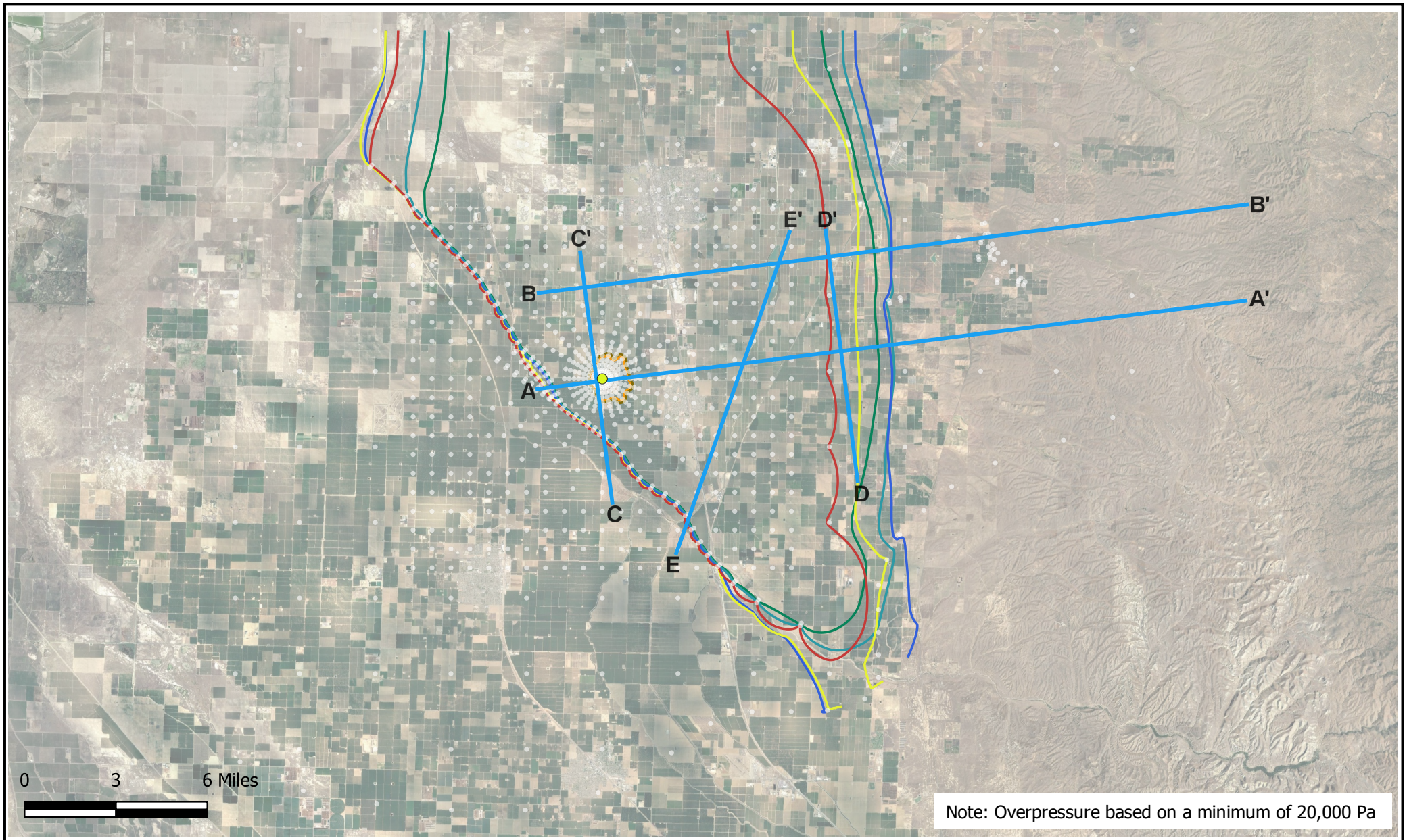

Explanation

- 15-Year
- 20-Year
- 40-Year
- 65-Year
- 75-Year
- 100-Year
- 115-Year
- Cross-Sections
- Injection Well
- TOUGH2 Elements

N

FRONTLINE BIOENERGY

TOUGH2 simulated maximum overpressure, base case (15 years to 115 years)

S:\Projects\DB19.1252_Frontline_Bioenergy\GIS\QGIS\EPA comments\Fig_3-2b TOUGH2 simulated maximum overpressure, base case (15 years to 115 years).qgz

08/11/2022 JN DB19.1252

Figure 3-2b

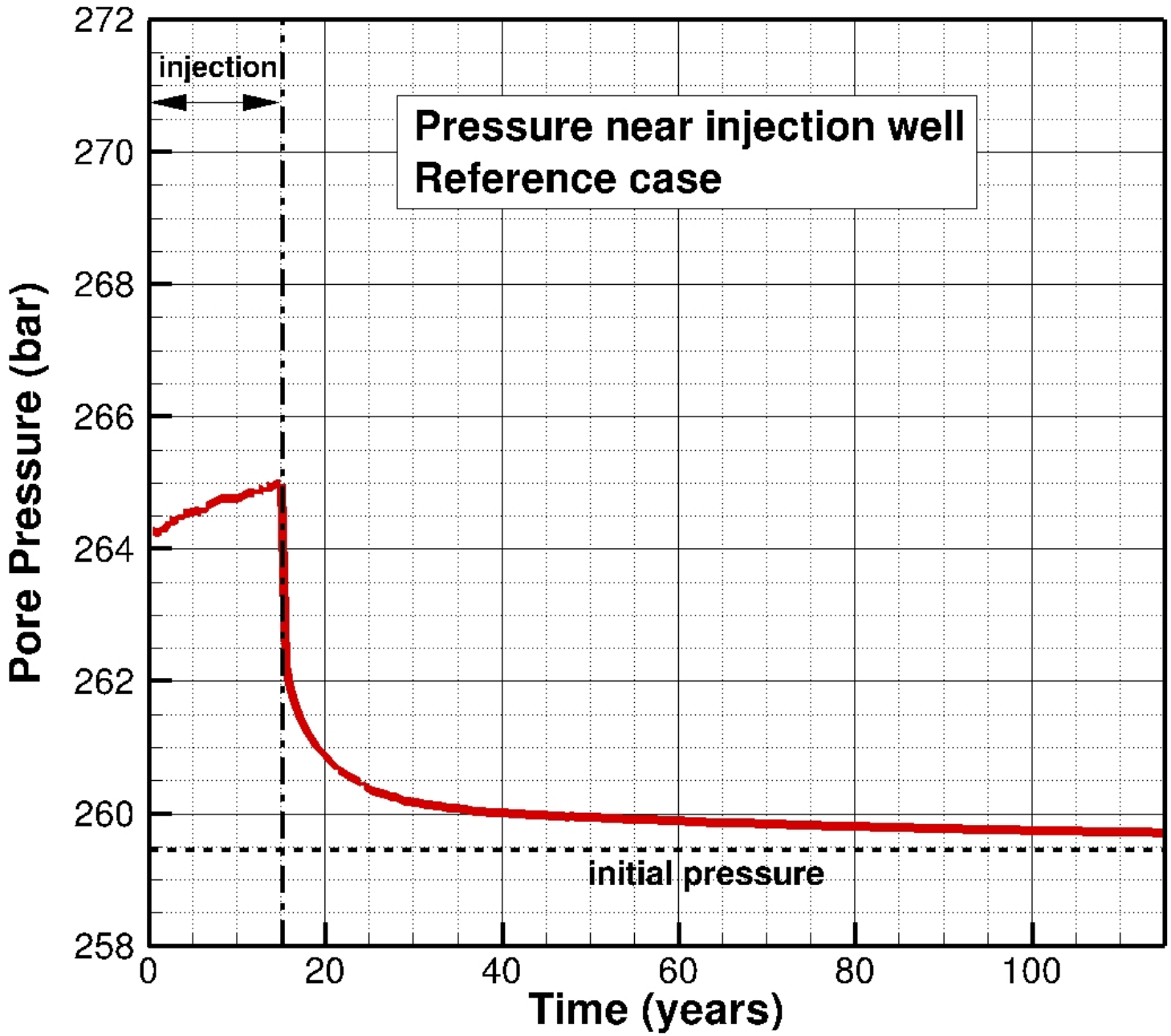

SAN JOAQUIN RENEWABLES

Average Pressure within a 10-m Radius of the Injection Well, Base Case

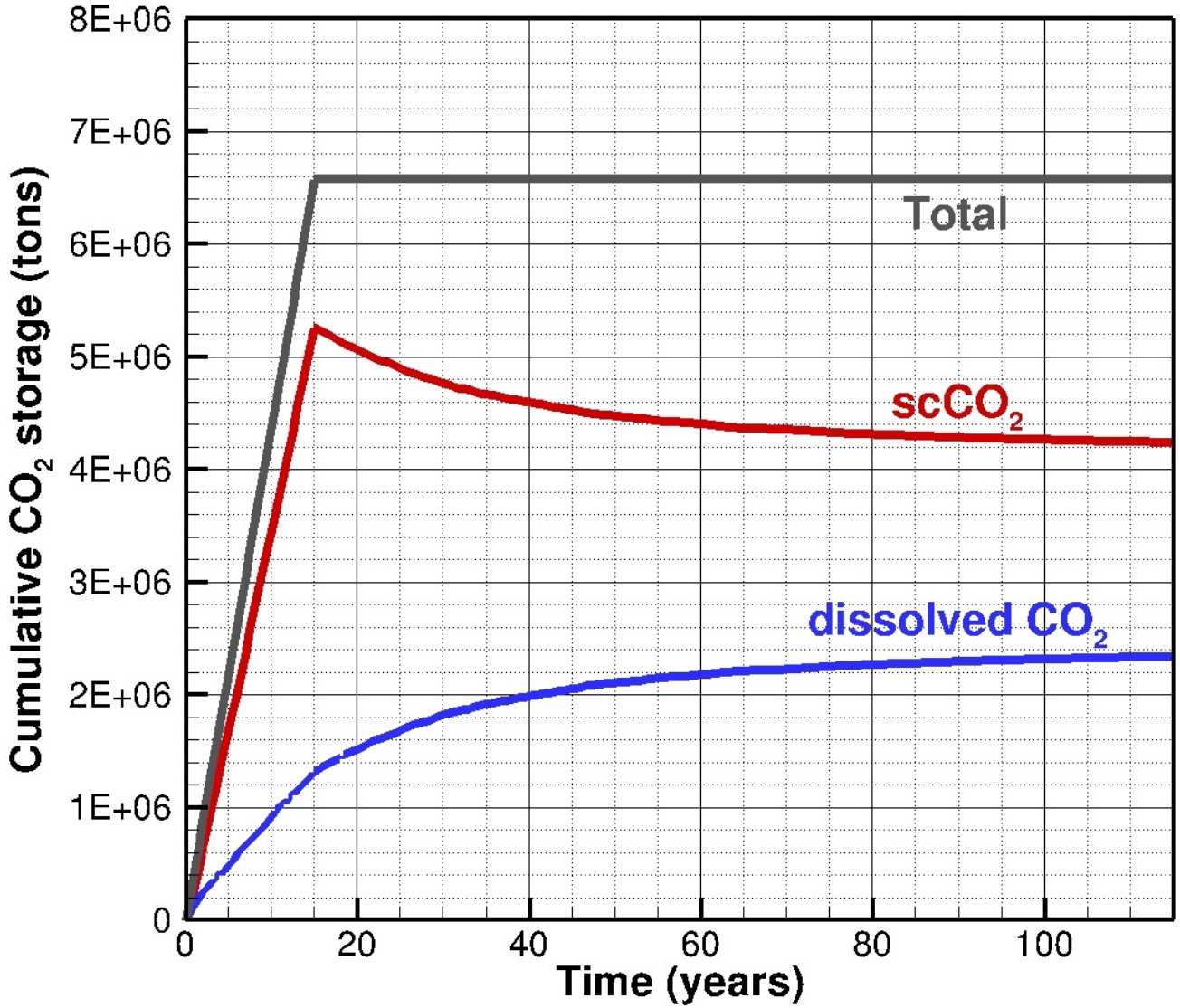

SAN JOAQUIN RENEWABLES

Cumulative CO2 stored in supercritical gas phase and dissolved in brine

S:\Projects\DB19.1252_Frontline_Bioenergy\GIS\QGIS\3-4 Cumulative CO2 stored in supercritical gas phase and dissolved in brine.qgz

08/11/2022 JN DB19.1252

Figure 3-4

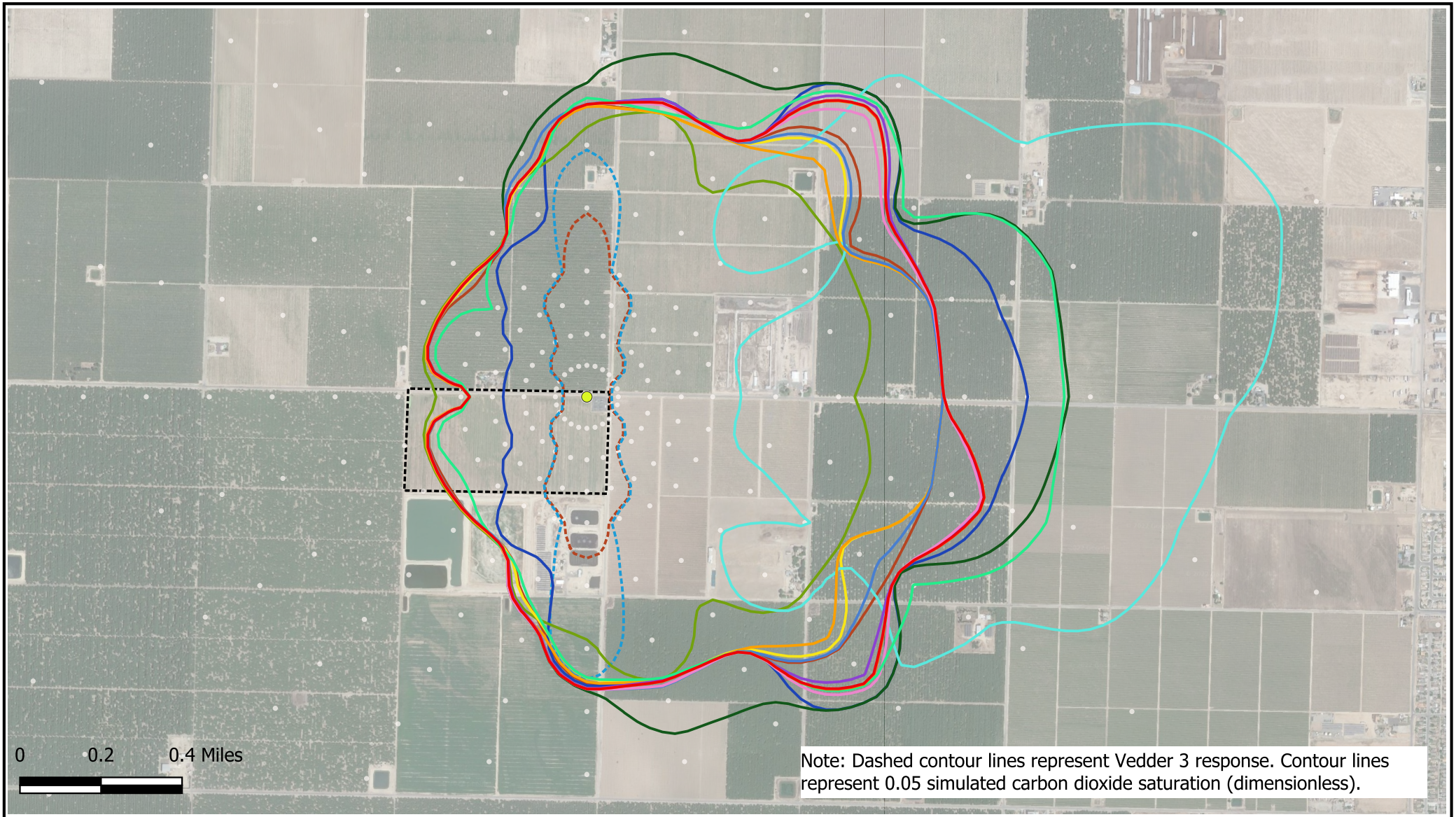

Explanation

- base case
- case A
- case A, vedder 3
- case B, vedder 3
- case C
- case D
- case E
- case F
- case G
- case H
- case I
- case J
- case K
- case L
- case M
- Injection Well
- TOUGH2 Elements
- Frontline Property Boundary

N

SAN JOAQUIN RENEWABLES

TOUGH2 simulated maximum carbon dioxide saturation, base case and sensitivity runs, Upper Vedder and Vedder 3 response

S:\Projects\DB19.1252_Frontline_Bioenergy\Analysis\TOUGH\Figures\Frontline_Case0-M_Final_SatGas_ViewB_2022_Sensitivity.qgz

08/16/2022 JN DB19.1252

Figure 3-5

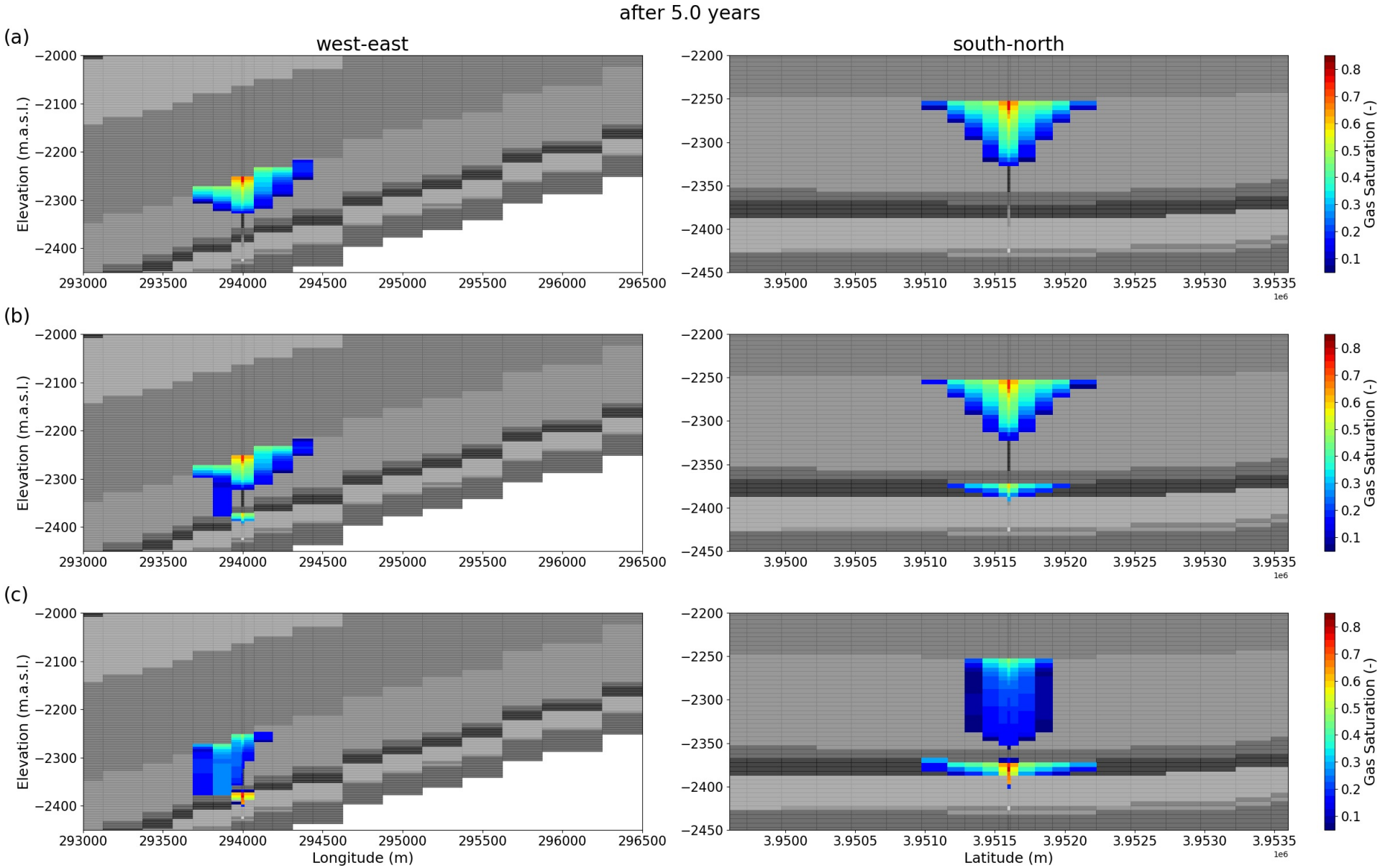

Notes: (a) Injection in Vedder Sand 1 and 2, (b) Injection in Vedder Sand 1, 2, and 3, and (c) Injection in Vedder Sand 3.

SAN JOAQUIN RENEWABLES

Comparison of scCO2 saturation profiles in west-eastern and south-northern directions (5 years)

S:\Projects\DB19.1252_Frontline_Bioenergy\GIS\QGIS\3-6a Comparison of scCO2 Saturation Profiles in West-Eastern and South-Northern Directions (5 years).qgz

08/11/2022 JN DB19.1252

Figure 3-6a

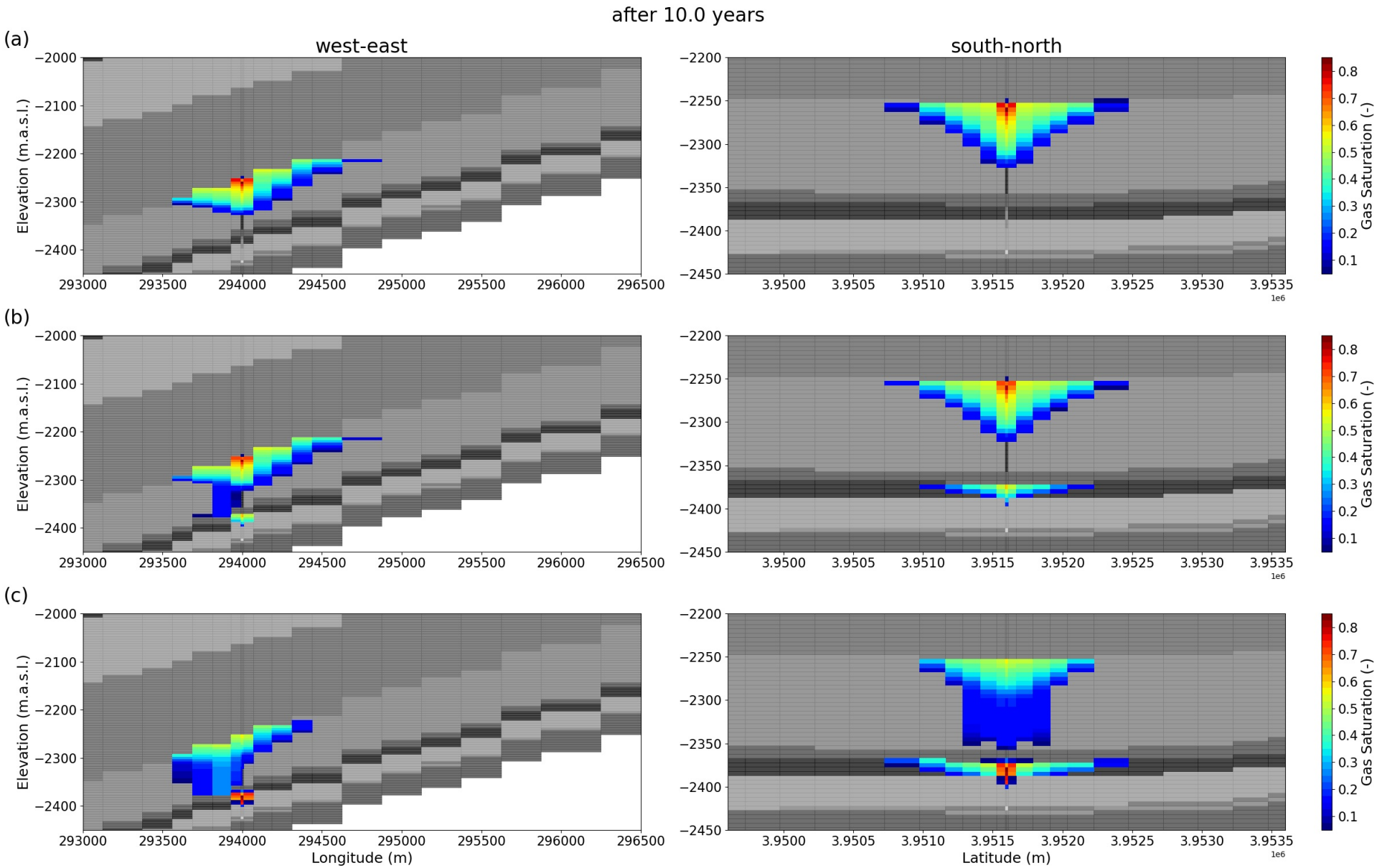

Notes: (a) Injection in Vedder Sand 1 and 2, (b) Injection in Vedder Sand 1, 2, and 3, and (c) Injection in Vedder Sand 3.

SAN JOAQUIN RENEWABLES

Comparison of scCO2 saturation profiles in west-eastern and south-northern directions (10 years)

S:\Projects\DB19.1252_Frontline_Bioenergy\GIS\QGIS\3-6b Comparison of scCO2 saturation profiles in west-eastern and south-northern directions (10 years).qgz

08/16/2022 JN DB19.1252

Figure 3-6b

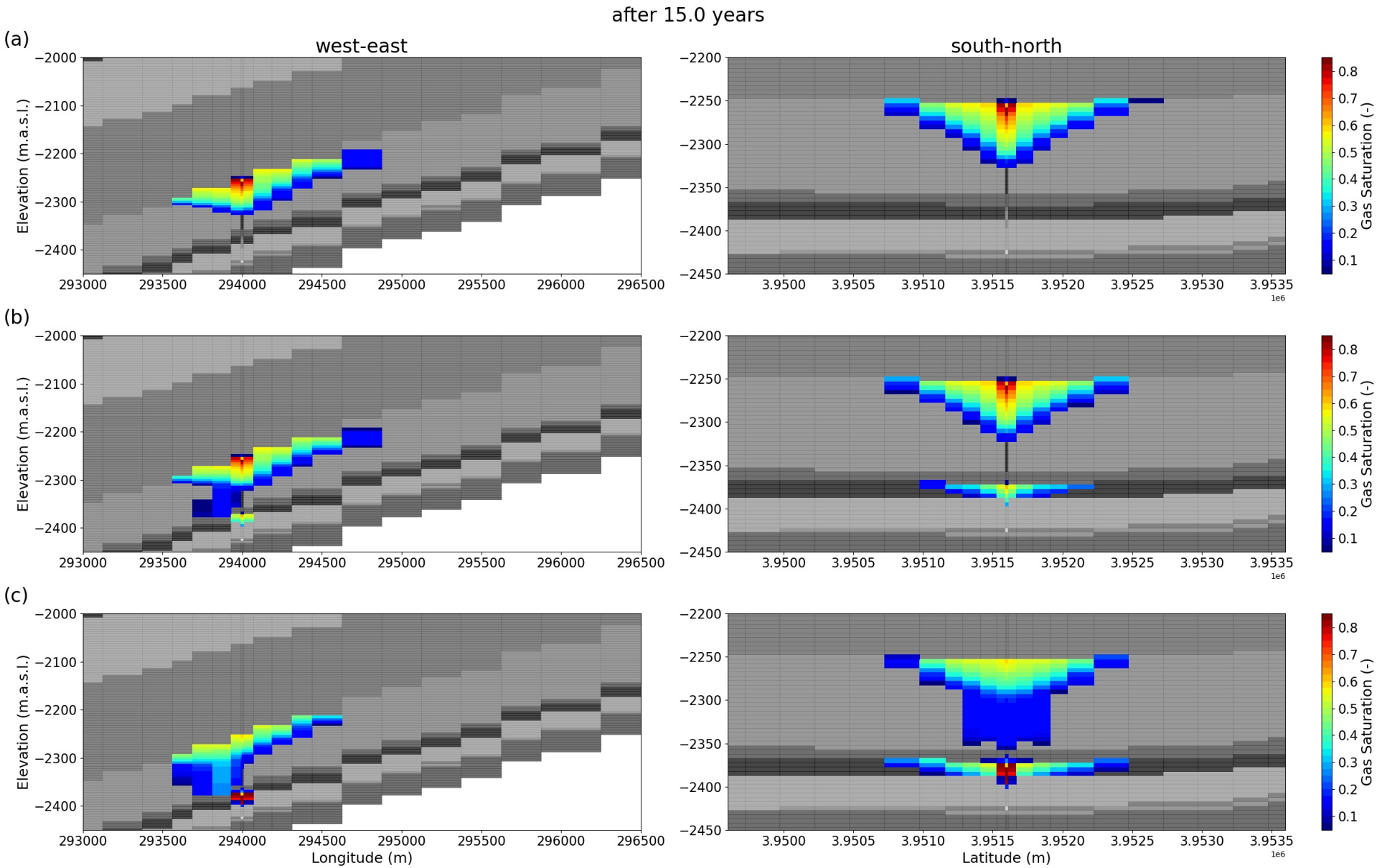

Notes: (a) Injection in Vedder Sand 1 and 2, (b) Injection in Vedder Sand 1, 2, and 3, and (c) Injection in Vedder Sand 3.

SAN JOAQUIN RENEWABLES

Comparison of scCO2 saturation profiles in west-eastern and south-northern directions (15 years)

S:\Projects\DB19.1252_Frontline_Bioenergy\GIS\QGIS\3-6c Comparison of scCO2 saturation profiles in west-eastern and south-northern directions (15 years).qgz

08/11/2022 JN DB19.1252

Figure 3-6c

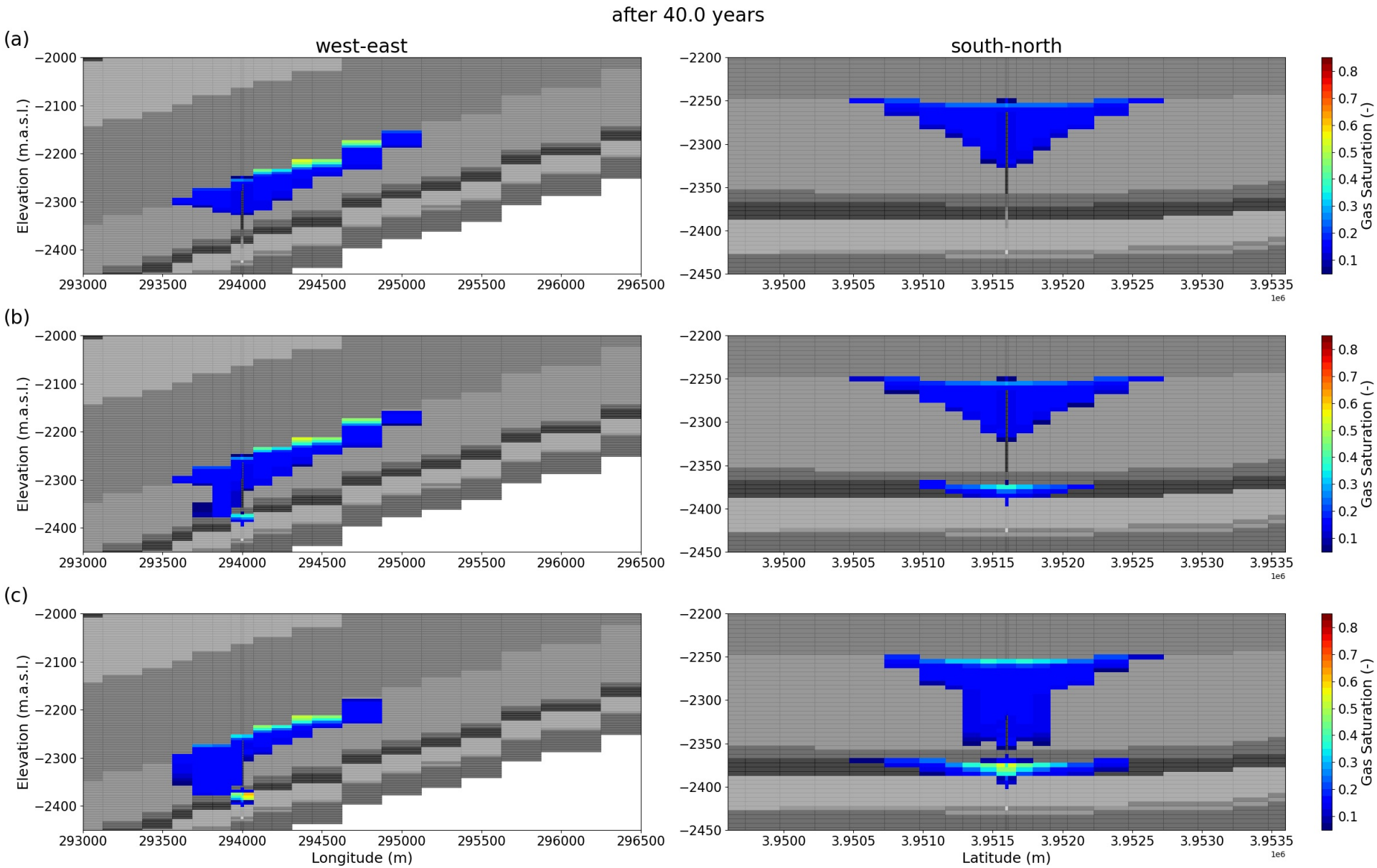

Notes: (a) Injection in Vedder Sand 1 and 2, (b) Injection in Vedder Sand 1, 2, and 3, and (c) Injection in Vedder Sand 3.

SAN JOAQUIN RENEWABLES

Comparison of scCO2 saturation profiles in west-eastern and south-northern directions (40 years)

S:\Projects\DB19.1252_Frontline_Bioenergy\GIS\QGIS\3-6d Comparison of scCO2 saturation profiles in west-eastern and south-northern directions (40 years).qgz

08/11/2022 JN DB19.1252

Figure 3-6d

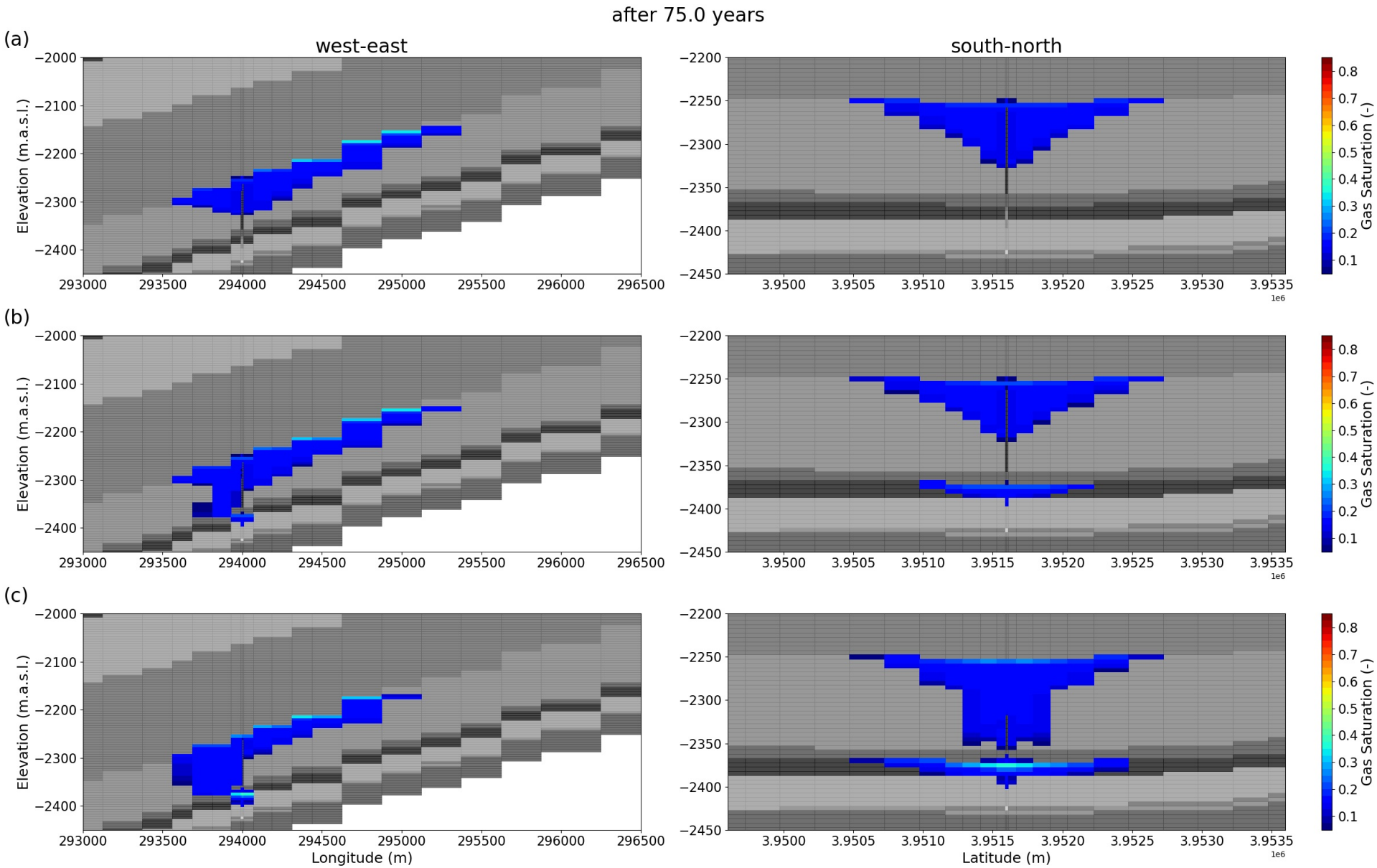

Notes: (a) Injection in Vedder Sand 1 and 2, (b) Injection in Vedder Sand 1, 2, and 3, and (c) Injection in Vedder Sand 3.

SAN JOAQUIN RENEWABLES

Comparison of scCO2 saturation profiles in west-eastern and south-northern directions (75 years)

S:\Projects\DB19.1252_Frontline_Bioenergy\GIS\QGIS\3-6e Comparison of scCO2 saturation profiles in west-eastern and south-norther directions (75 years).qgz

08/11/2022 JN DB19.1252

Figure 3-6e

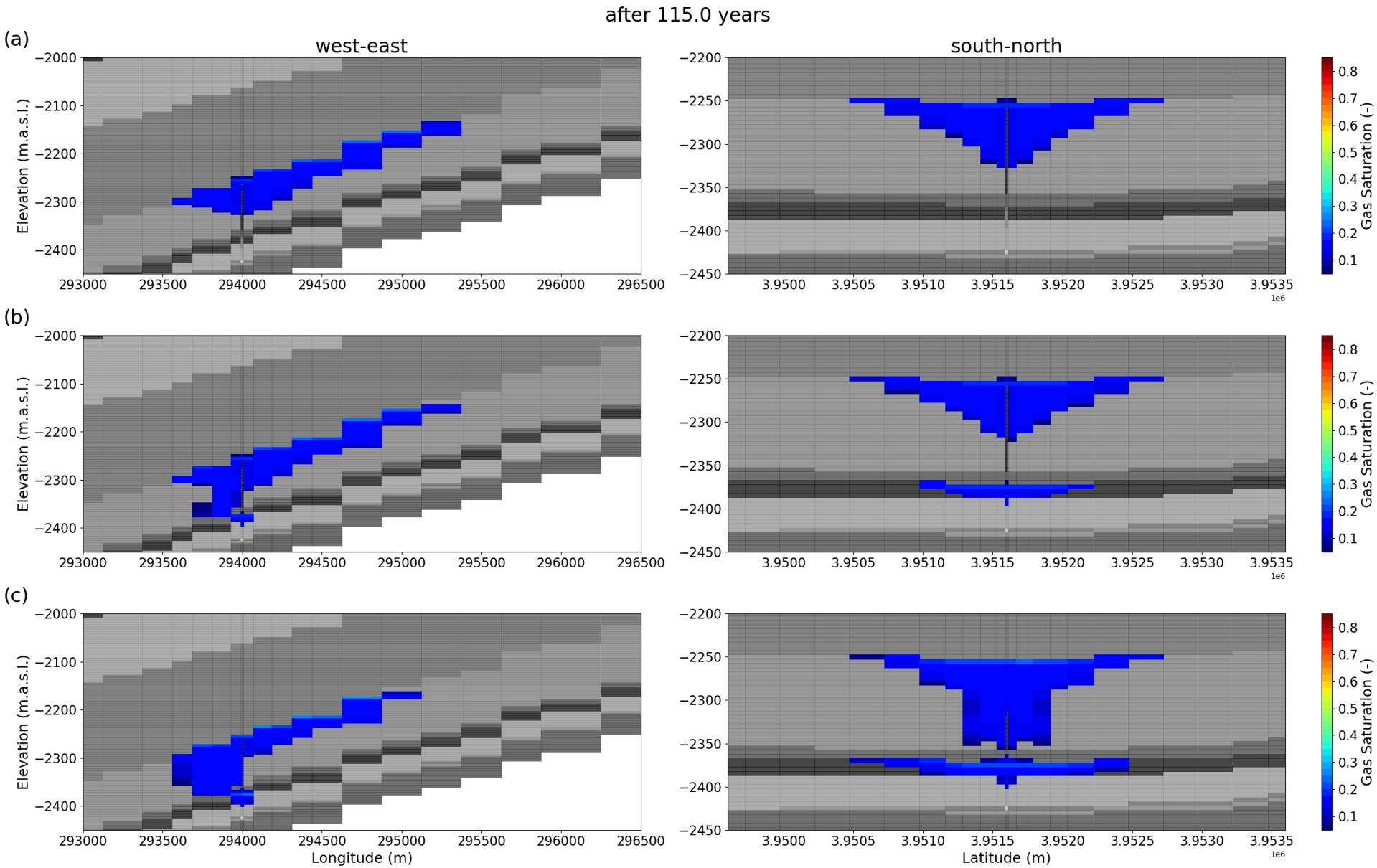

Notes: (a) Injection in Vedder Sand 1 and 2, (b) Injection in Vedder Sand 1, 2, and 3, and (c) Injection in Vedder Sand 3.

SAN JOAQUIN RENEWABLES

Comparison of scCO2 saturation profiles in west-eastern and south-northern directions (115 years)

S:\Projects\DB19.1252_Frontline_Bioenergy\GIS\QGIS\3-6f Comparison of scCO2 saturation profiles in west-eastern and south-northern directions (115 years).qgz

08/11/2022 JN DB19.1252

Figure 3-6f

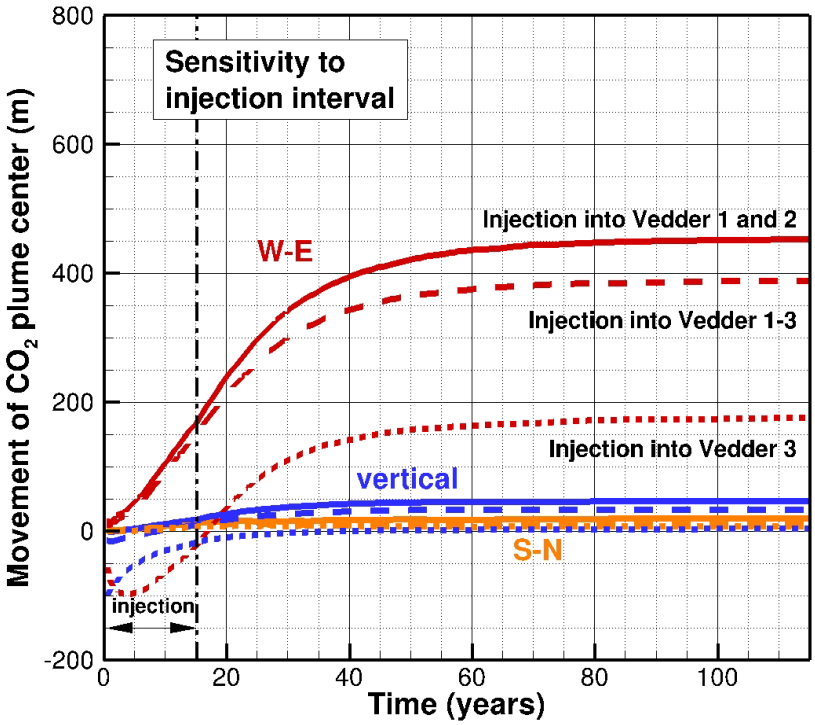

(a) The first moment indicates the migration of the center of mass of the $scCO_2$ plume away from the injection well.

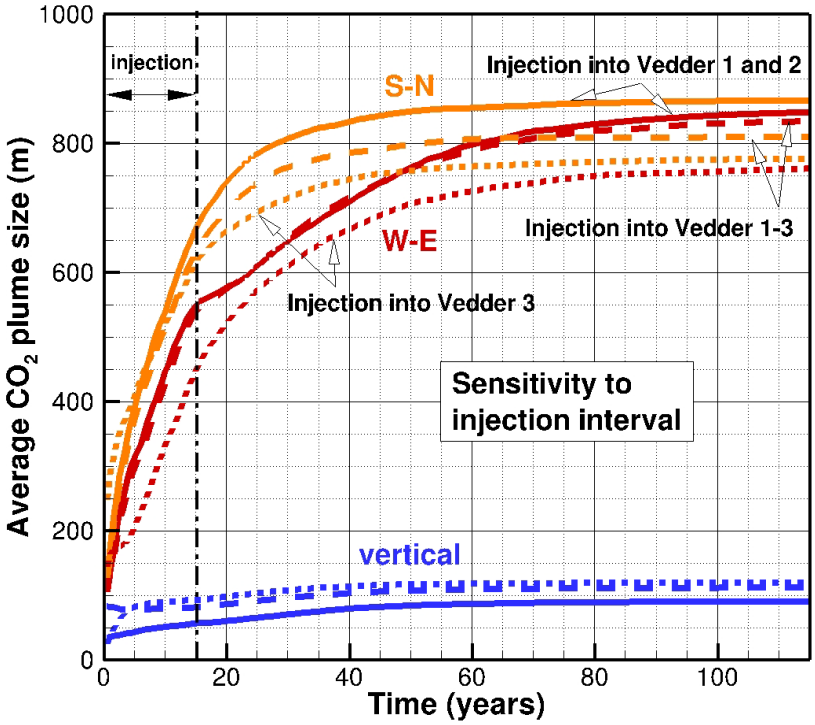

(b) The second moment indicates the average extent of the $scCO_2$ plume.

Notes:
Solid line = Reference Case
Dashed line = Case A
Dotted line = Case B

SAN JOAQUIN RENEWABLES

Central Moments of $scCO_2$ Plume for Different Injection Intervals

Figure 3-7

S:\Projects\DB19.1252_Frontline_Bioenergy\Final Documents\EPA Class VI permit application\3_AoR Corrective Action Plan\Figures\word\Fig_3-7 Different injection iintervals.docxintervals.docxintervals.docx

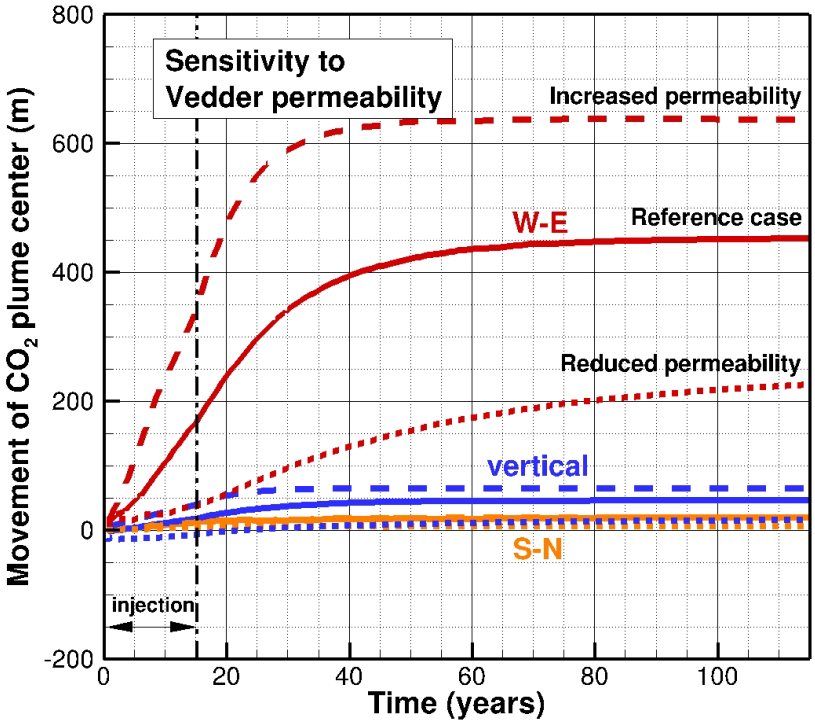

(a) The first moment indicates the migration of the center of mass of the $scCO_2$ plume away from the injection well.

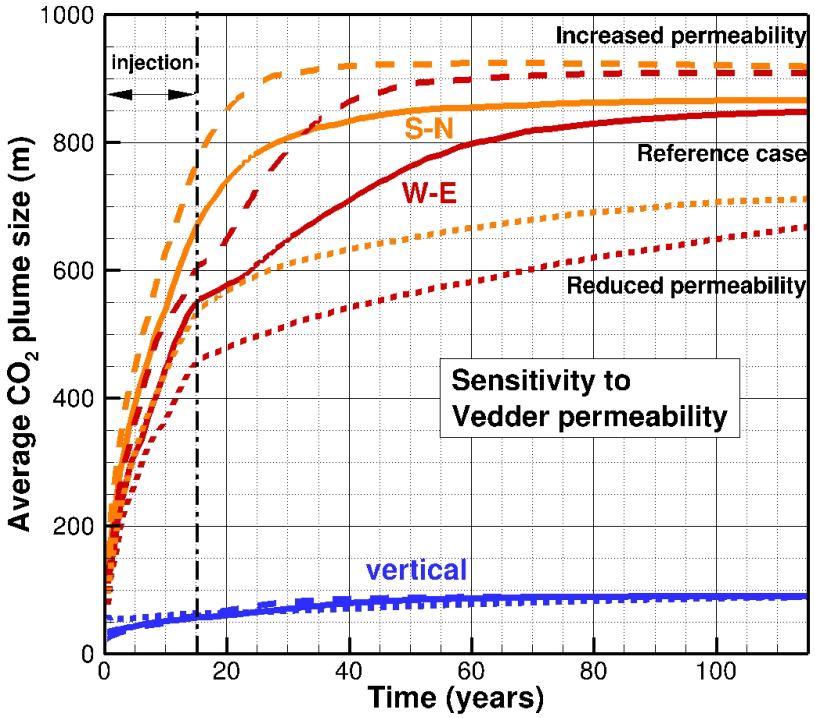

(b) The second moment indicates the average extent of the $scCO_2$ plume.

Notes:
Solid line = Reference Case
Dashed line = Case C
Dotted line = Case D

SAN JOAQUIN RENEWABLES

Central Moments of $scCO_2$ Plume for Permeability Sensitivity Cases

Figure 3-8

S:\Projects\DB19.1252_Frontline_Bioenergy\Final Documents\EPA Class VI permit application\3_AoR Corrective Action Plan\Figures\word\Fig_3-8 Permeability Sensitivity.docx

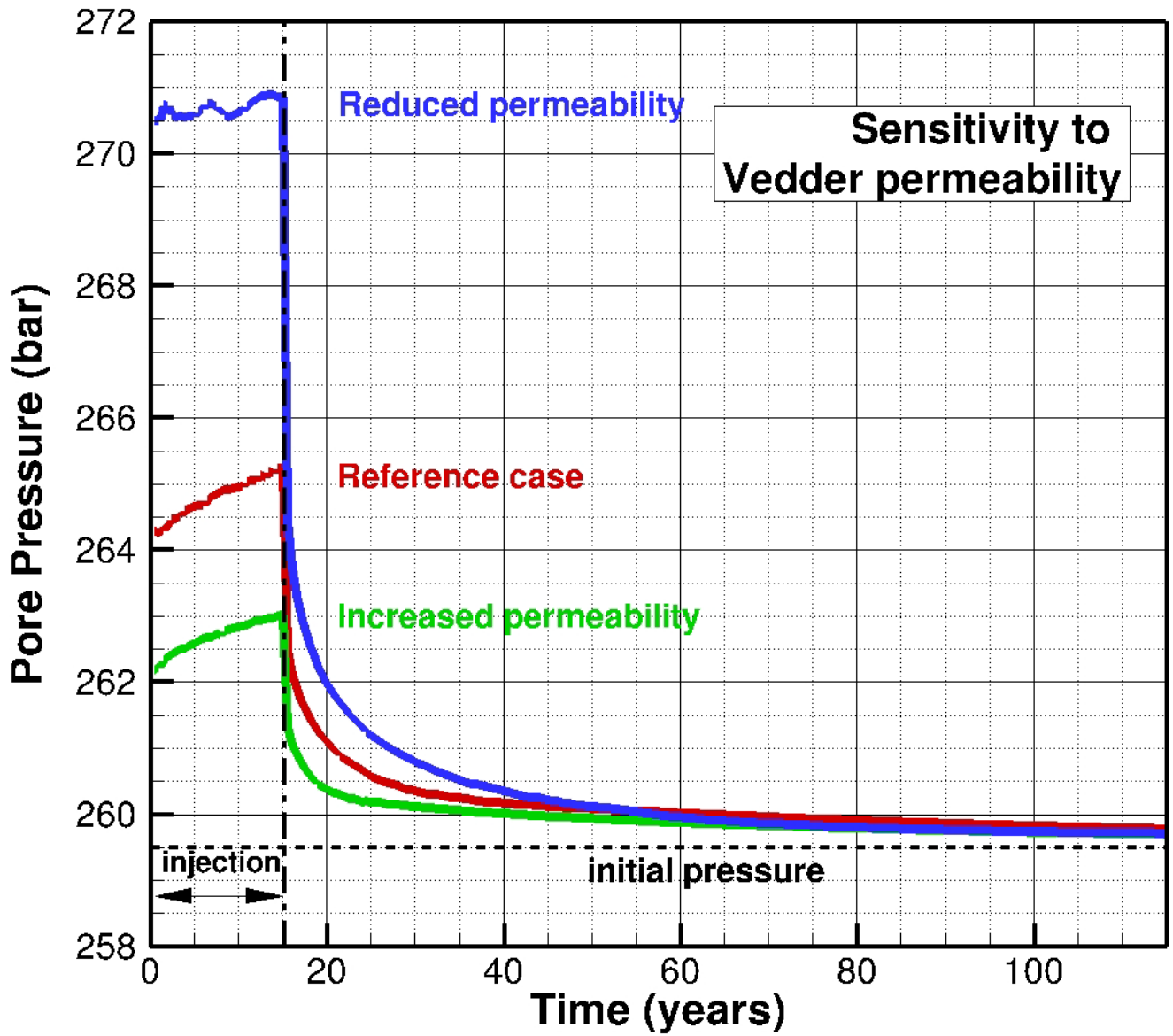

SAN JOAQUIN RENEWABLES

Average Pressure within a 10-m Radius of the Injection Well for Permeability Sensitivity Cases

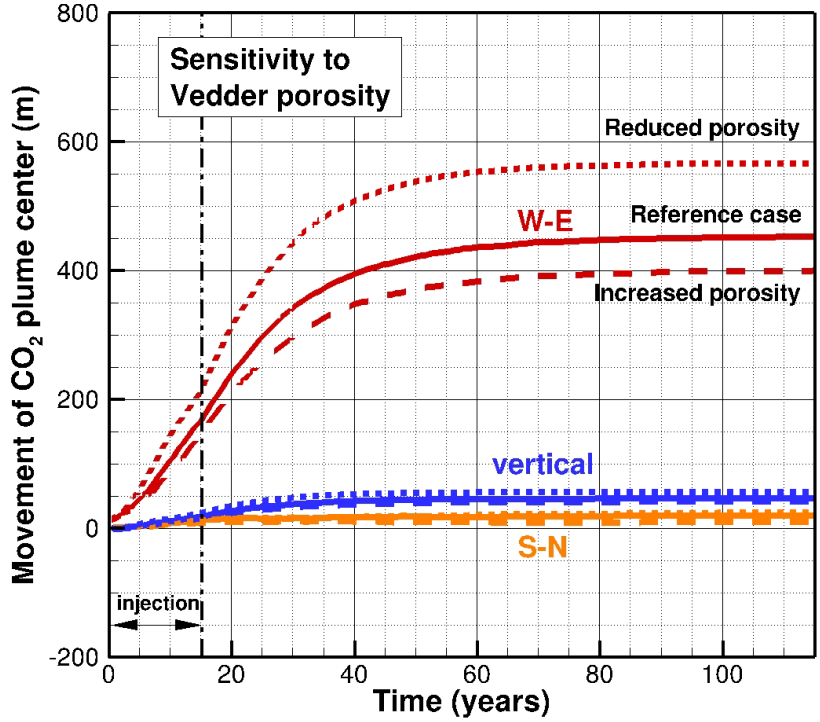

(a) The first moment indicates the migration of the center of mass of the $scCO_2$ plume away from the injection well.

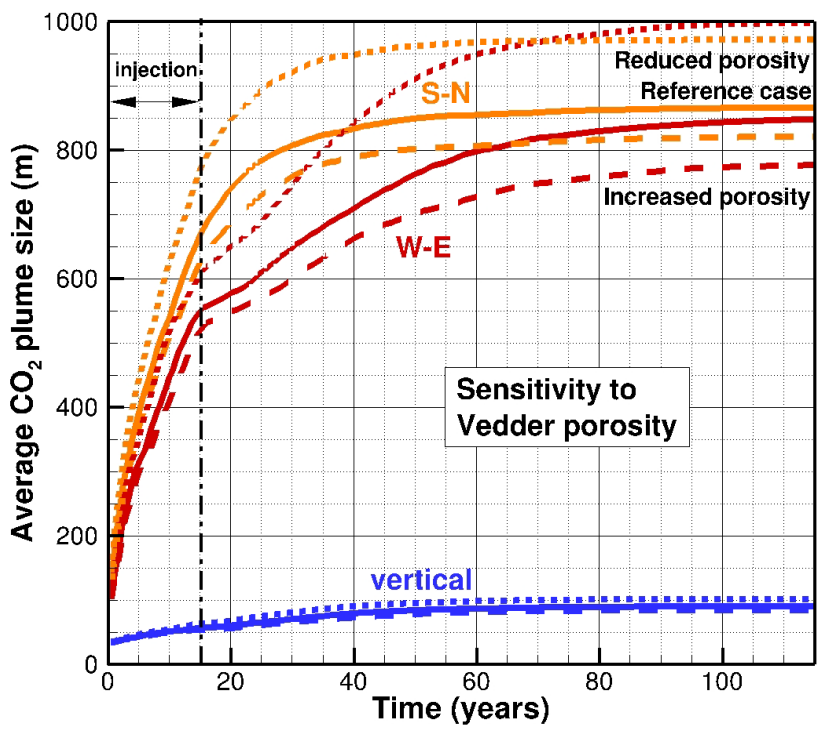

(b) The second moment indicates the average extent of the $scCO_2$ plume.

Notes:
Solid line = Reference Case
Dashed line = Case E
Dotted line = Case F

SAN JOAQUIN RENEWABLES

Central Moments of $scCO_2$ Plume for Porosity Sensitivity Cases

Figure 3-10

S:\Projects\DB19.1252_Frontline_Bioenergy\Final Documents\EPA Class VI permit application\3_AoR Corrective Action Plan\Figures\word\Fig_3-10 Porosity Sensitivity.docx

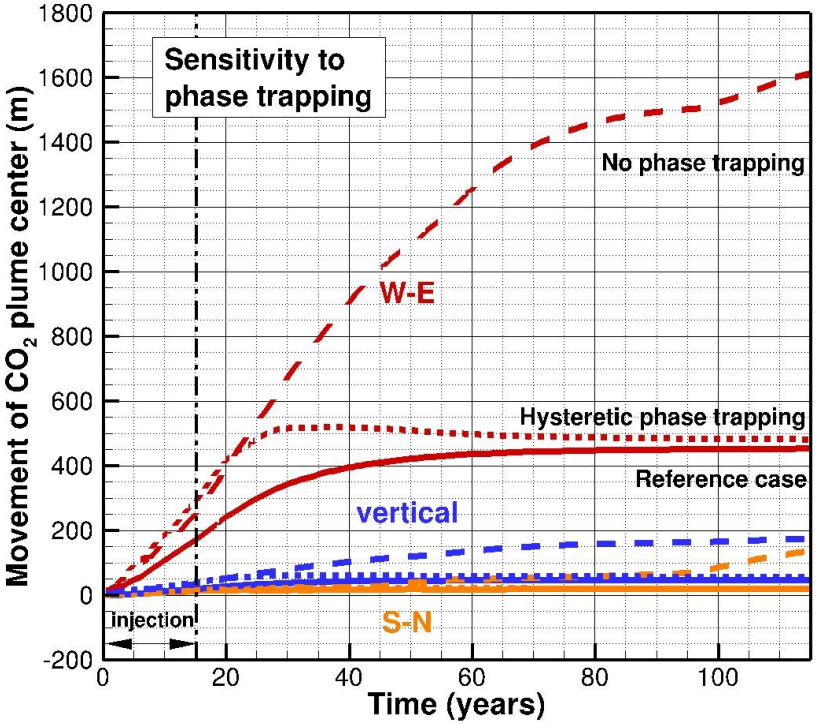

(a) The first moment indicates the migration of the center of mass of the $scCO_2$ plume away from the injection well.

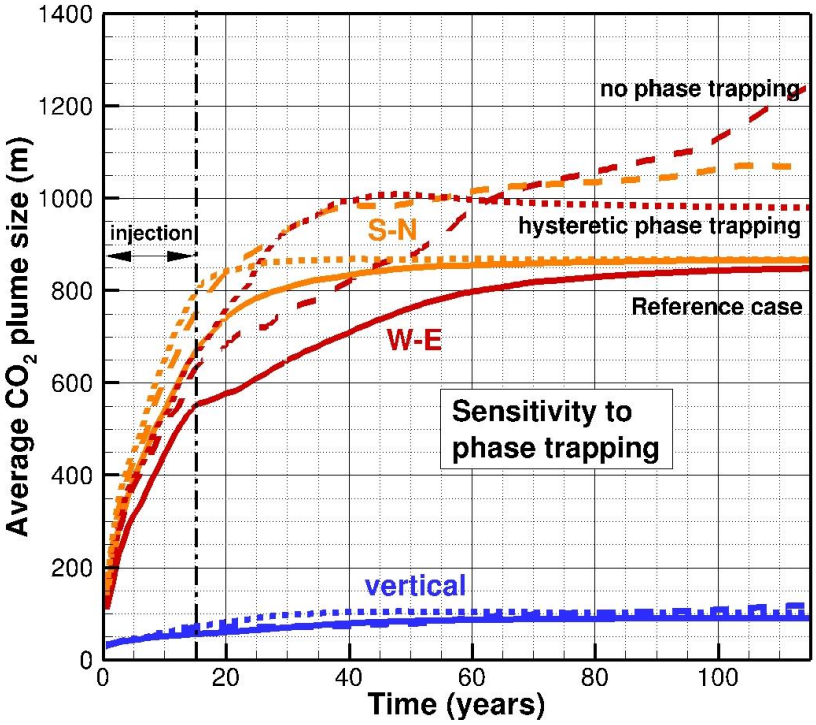

(b) The second moment indicates the average extent of the $scCO_2$ plume.

Notes:
Solid line = Reference Case
Dashed line = Case G
Dotted line = Case L

SAN JOAQUIN RENEWABLES

Central Moments of $scCO_2$ Plume for Different Phase Trapping Mechanisms

Figure 3-11

S:\Projects\DB19.1252_Frontline_Bioenergy\Final Documents\EPA Class VI permit application\3_AoR Corrective Action Plan\Figures\word\Fig_3-11 Central moments of scCO2 plume for different phase trapping mechanisms.docx

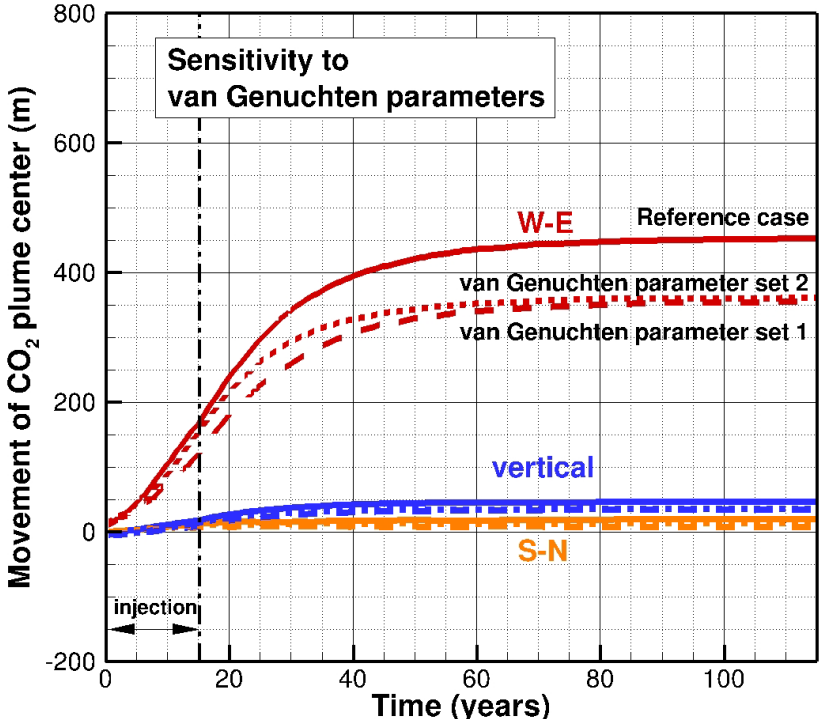

(a) The first moment indicates the migration of the center of mass of the $scCO_2$ plume away from the injection well.

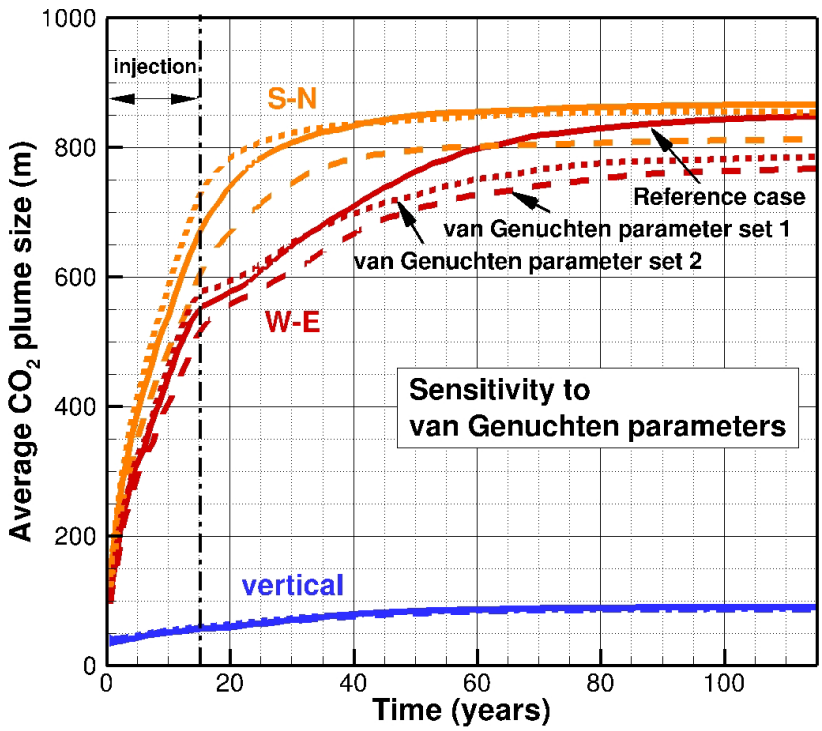

(b) The second moment indicates the average extent of the $scCO_2$ plume.

Notes:
Solid line = Reference Case
Dashed line = Case H
Dotted line = Case I

SAN JOAQUIN RENEWABLES

Central Moments of $scCO_2$ Plume for Different Sets of van Genuchten Parameters

Figure 3-12

S:\Projects\DB19.1252_Frontline_Bioenergy\Final Documents\EPA Class VI permit application\3_AoR Corrective Action Plan\Figures\word\Fig_3-12 van Genuchten parameters.docxparameters.docx

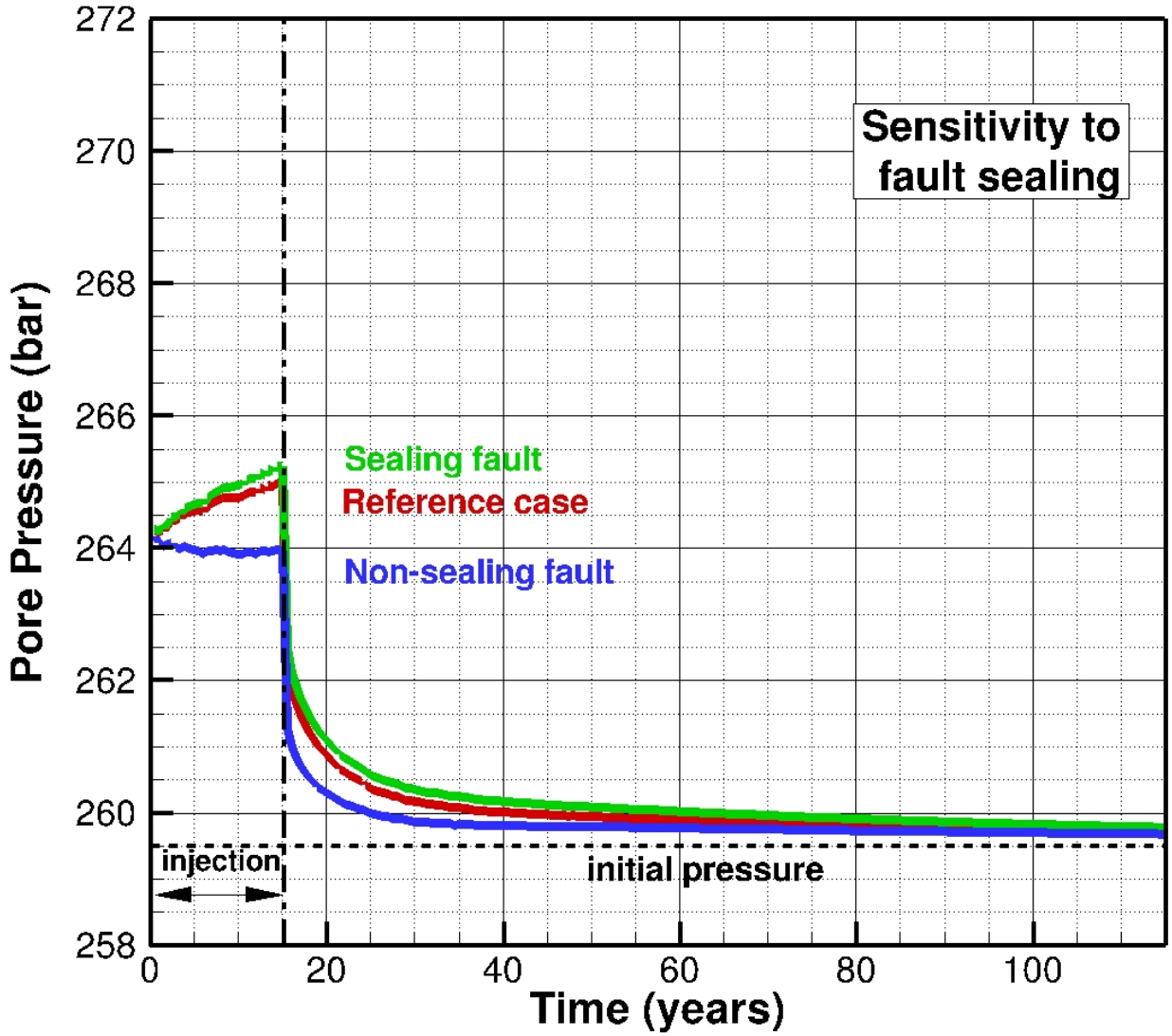

SAN JOAQUIN RENEWABLES

Average Pressure within a 10-m Radius of the Injection Well, Fault Sealing Sensitivity Case

Figure 3-13

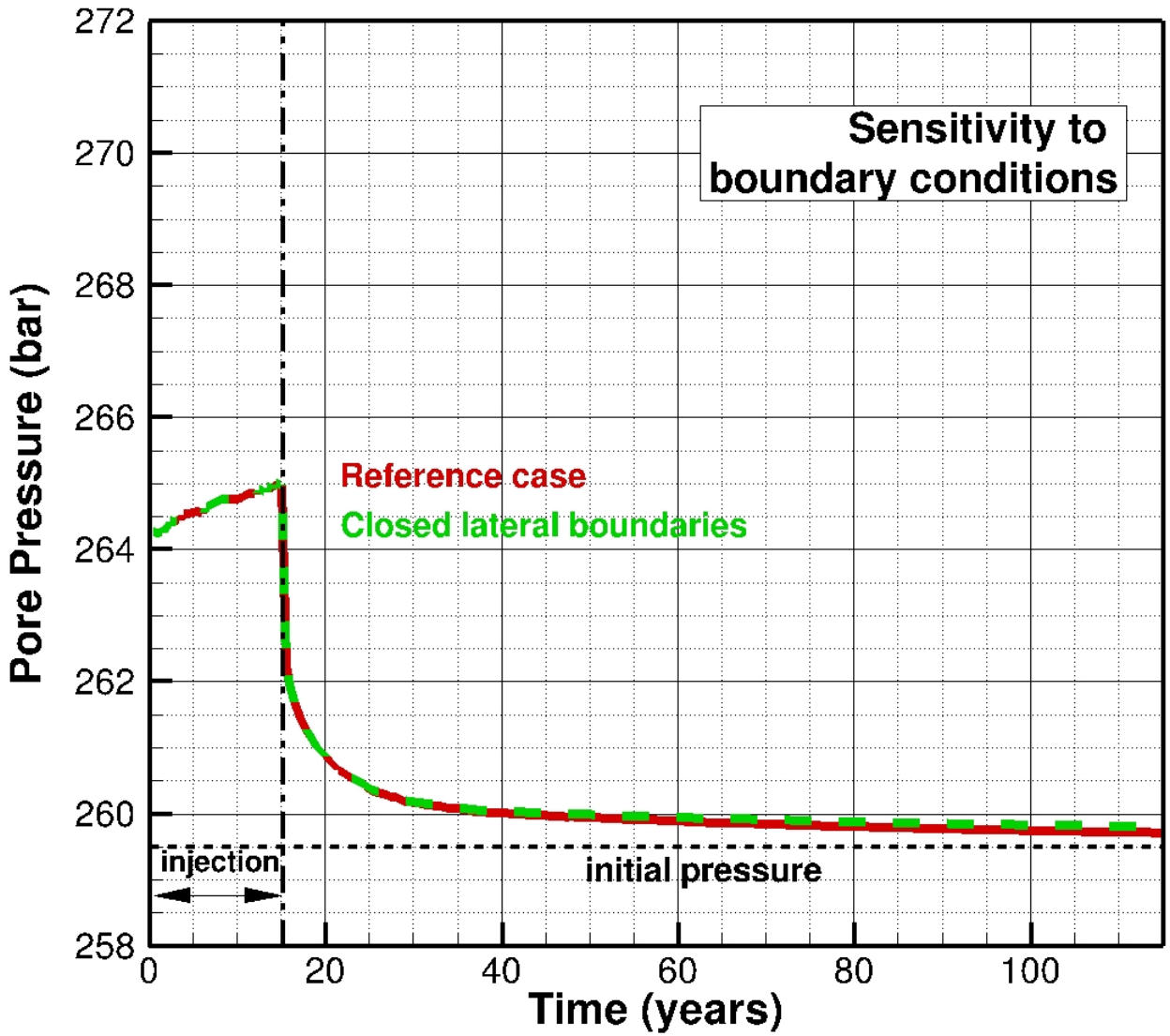

SAN JOAQUIN RENEWABLES

Average Pressure within a 10-m Radius of the Injection Well, Boundary Condition Sensitivity Analyses

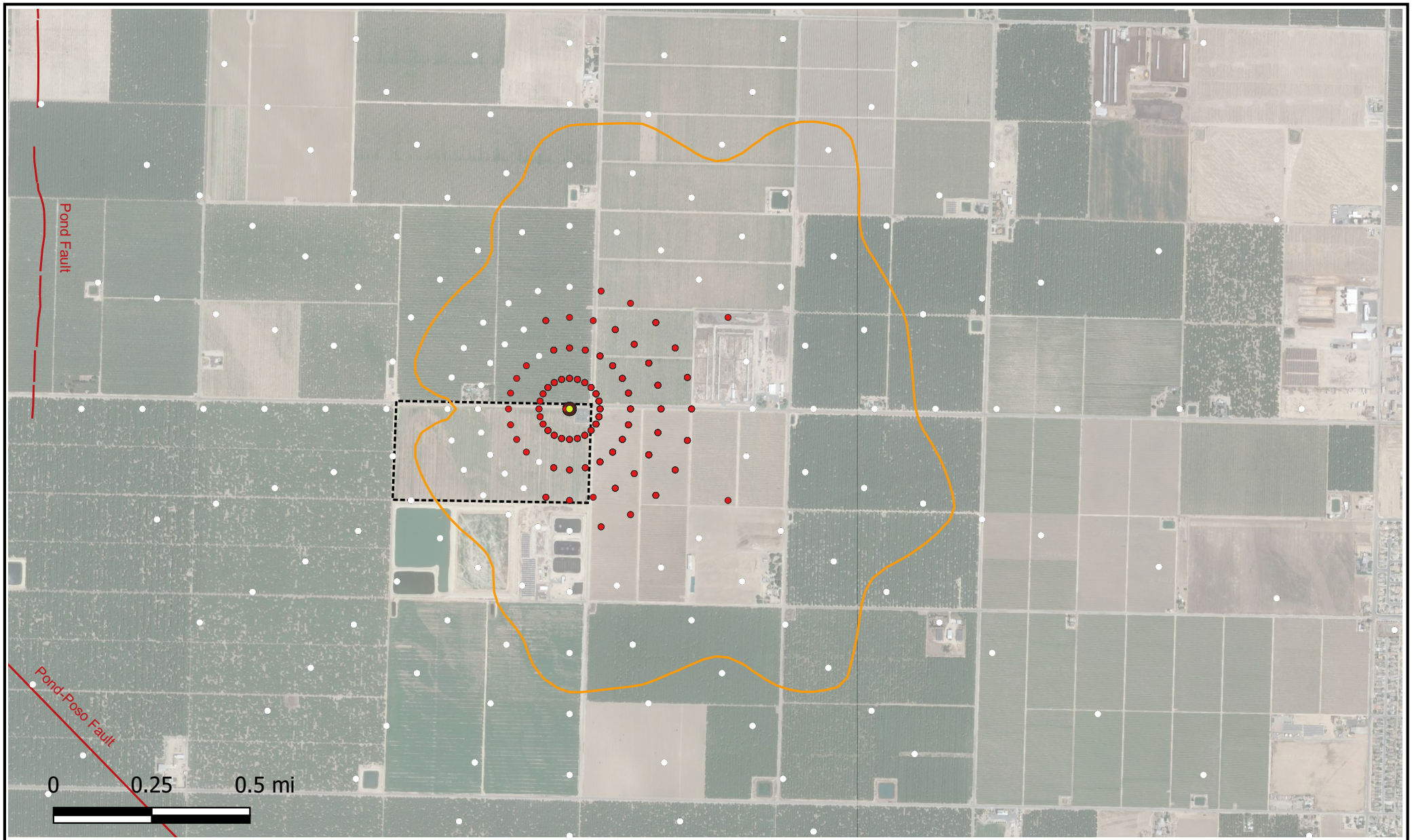

Explanation

- Quaternary Faults
- Area of Review/Storage Complex (115-yr carbon dioxide 0.05 contour line)
- Areas with greater than admissible pressure, 15 years
- TOUGH2 Elements
- SJR Property Boundary
- Injection Well

N

SAN JOAQUIN RENEWABLES

AoR Delineation

S:\Projects\DB19.1252_Frontline_Bioenergy\GIS\QGIS\EPA comments\Fig_4-1_Area of Review - Storage Complex.qgz

08/16/2022 JN DB19.1252

Figure 4-1

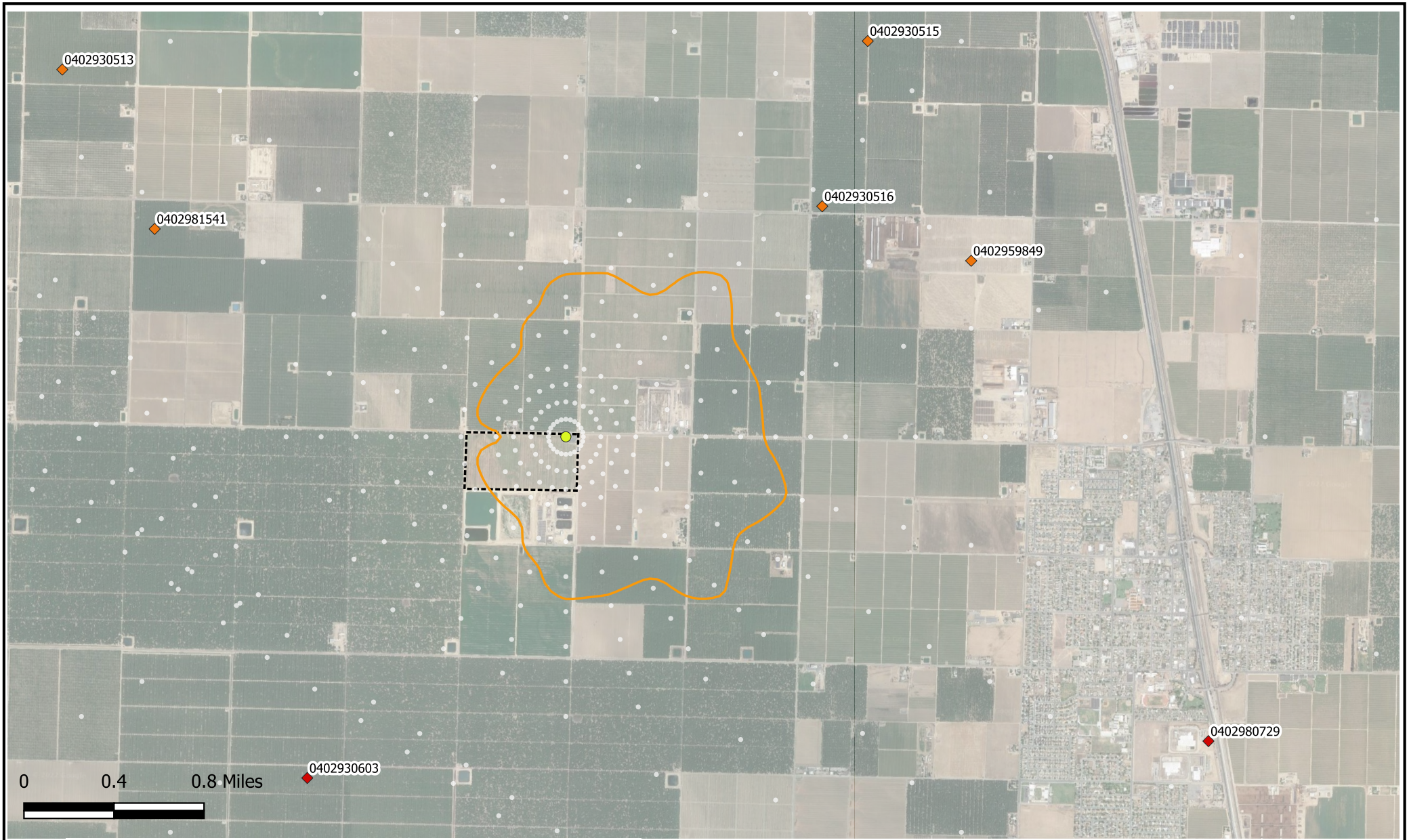

Explanation

Oil and Gas Well

- Penetrates Freeman-Jewett
- Does Not Penetrate Freeman-Jewett
- Injection Well

TOUGH2 Elements

Area of Review/Storage Complex

SJR Property Boundary

N

SAN JOAQUIN RENEWABLES

AoR Delineation and Oil and Gas Wells

S:\Projects\DB19.1252_Frontline_Bioenergy\GIS\QGIS\EPA comments\Fig_4-2_ Area of Review - Storage Complex and Oil and Gas wells.qgz

08/11/2022 JN DB19.1252

Figure 4-2

Tables

List of Tables

2-1 Model domain information (in text)
2-2 Base Case Simulation Permeability and Porosity Values
2-3 Pond-Poso Creek Fault Permeability Subcategories

3-1 Sensitivity Analyses

Table 2-2. Summary of Porosity and Permeability from Core Data

Formation	Permeability					Porosity	
	Horizontal mD	Horizontal Basis	Vertical mD	Basis	Anisotropy Ratio	Value (%)	Basis
Round-Mountain	0.037	GM of all values	0.00073	HM of all values	50.0	20	Assumed same as Freeman-Jewett
Olcese [a]	76.6	Weighted GM assuming 90% sands, 10% shales	4.3	Weighted HM assuming 90% sands, 10% shales	17.9	28	Median all values
Freeman-Jewett	0.26	GM of all values	0.0036	HM of all values	71.3	20	Median all values
PYDH-VED1-VED2	254.31	GM of all values	62.0	HM of all values	4.1	34	Median all values
VED2 SH	0.11	GM of all values	0.0052	HM of all values	20.3	15	Median all values
VED3	192.29	GM of all values	154.15	HM of all values	1.2	31	Median all values
VED3 SH	0.11	No samples, assumed same as VED 2 SH	0.0052	No samples, assumed same as VED 2 SH	20.3	15	No values, assumed same as VED 2 SH
VED4	613	GM of all values	116	HM of all values	5.3	26	Median all values
VED4 SH	0.91	GM of all values	0.025	HM of all values	35.8	27	Median all values
Walker	36.37	GM of all values	1.41	HM of all values	25.8	26	Median all values

[a] Excludes KCL-25-1 sample at 6,131 feet bgs (very low-k shale) for permeability values.

GM = Geometric mean
HM = Harmonic mean
PYDH-VED1-VED2 = Pyramid Hills/Vedder 1/Vedder 2 Sand
VED2 SH = Vedder 2 Shale
VED3 = Vedder 3 Sand
VED3 SH = Vedder 3 Shale
VED4 = Vedder 4 Sand
VED4 SH = Vedder 4 Shale

Table 2-3. Fault Subcategories

Cross Section	Effective Fault Gouge K (mD)			Subcategory		
	Olcese	PYDH-V1-V2	VED3	Olcese	PYDH-V1-V2	VED3
1	0.477	0.47	0.381	A	A	A
2	0.278	0.03	0.5	A	C	A
3	0.235	0.001	0.5	B	D	A
4	0.225	0.001	0.5	B	D	A
5	0.242	0.001	0.5	B	D	A
6	0.227	0.001	0.5	B	D	A
7	0.241	0.001	0.5	B	D	A
8	0.134	0.001	0.5	B	D	A
9	0.001	0.001	0.5	D	D	A
10	0.001	0.001	0.001	D	D	D
11	0.001	0.08	0.481	D	B	A
12	0.001	0.389	0.001	D	A	D
13	0.001	0.5	0.254	D	A	A
14	0.001	0.5	0.001	D	A	D
15	0.001	0.252	0.001	D	A	D
16	0.001	0.146	0.001	D	B	D
17	0.001	0.001	0.001	D	D	D
18	0.001	0.001	0.001	D	D	D
19	0.001	0.001	0.001	D	D	D
20	0.001	0.001	0.001	D	D	D
21	0.332	0.172	0.5	A	B	A
22	0.168	0.076	0.5	B	B	A
23	0.436	0.142	0.5	A	B	A

Subcategory	k, Horizontal	k, Vertical
A	0.5	0.05
B	0.1	0.01
C	0.03	0.003
D	0.001	0.0001

Table 3-1. Overview of Sensitivity Cases
Page 1 of 2

Case	Description	Reference	Perturbation
0	Reference case		NA
A	Injection from longer interval	Injection into Upper Vedder sands	Injection into Upper Vedder and Vedder 3 sands
B	Injection from deeper interval	Injection into Upper Vedder sands	Injection into Vedder 3 sands
C	Increased permeability of Vedder sands based on 75th percentile of measured values; maintain anisotropy ratio	k_h = 254 mD k_v = 62 mD	k_h = 555 mD k_v = 136 mD
D	Decreased permeability of Vedder sands based on 25th percentile of measured values; maintain anisotropy ratio	k_h = 254 mD k_v = 62 mD	k_h = 82 mD k_v = 20 mD
E	Increased porosity of Vedder sands based on 90th percentile of measured values	f = 0.34	f = 0.39
F	Decreased porosity of Vedder sands based on 10th percentile of measured values	f = 0.34	f = 0.26
G	Reduced phase trapping by reduced residual gas saturation of Vedder sands	S_{gr} = 0.15	S_{gr} = 0.00
H	Changed van Genuchten parameters for relative permeability and capillary pressure of Vedder sands	S_{lr} = 0.0 n = 1.842 $1/a$ = 0.2 bar	S_{lr} = 0.3 n = 2.5 $1/a$ = 0.5 bar
I	Changed van Genuchten parameters for relative permeability and capillary pressure of Vedder sands	S_{lr} = 0.0 n = 1.842 $1/a$ = 0.2 bar	S_{lr} = 0.1 n = 1.5 $1/a$ = 0.1 bar
J	Sealing faults	Fault permeabilities based on Allan diagrams	All faults sealing k_h = 0.0036 mD k_v = 0.0036 mD
K	Non-sealing faults	Fault permeabilities based on Allan diagrams	All faults non-sealing k_h = 254 mD k_v = 0.0036 mD

Table 3-1. Overview of Sensitivity Cases
Page 2 of 2

Case	Description	Reference	Perturbation
L	Hysteretic characteristic curves	Non-hysteretic characteristic curves	Hysteretic characteristic curves from Doughty (2010)
M	Side boundary conditions	Dirichlet side boundary conditions	No-flow side boundary conditions

Appendix A: Model Parameter values from Birkholzer et al. (2011)

Available online at www.sciencedirect.com
ScienceDirect
Energy Procedia 4 (2011) 4371–4378
Energy Procedia
www.elsevier.com/locate/procedia

GHGT-10

A Sensitivity Study on Regional Pressure Buildup from Large-Scale CO_2 Storage Projects

J.T. Birkholzer*, Q. Zhou, A. Cortis, S. Finsterle
Lawrence Berkeley National Laboratory, 1 Cyclotron Road, MS 90-116, Berkeley, CA 94707, USA

Table 1. Hydrogeologic properties assigned to each formation: k_h is horizontal permeability, k_v is vertical permeability, Φ is porosity, β_p is pore compressibility, α is the van Genuchten parameter for entry capillary pressure, and m is the van Genuchten parameter for pore-size distribution.

Formations	k_h [mDarcy]	k_v [mDarcy]	Φ [-]	β_p [10^{-10} Pa^{-1}]	α [10^{-5} Pa^{-1}]	m [-]
Non-Fault Zones						
Pre-Etchegoin	3000	3000	0.35	15.5	5.0	0.457
Etchegoin	1200	1200	0.32	15.5	5.0	0.457
Macoma-Chanac	1900	1900	0.31	10.5	5.0	0.457
Santa Margarita-McLure	2000	2000	0.275	10.5	5.0	0.457
Stevens Sand	240	48	0.22	10.5	5.0	0.457
Fruitvale-Round Mountain	0.002	0.001	0.338	14.5	0.42	0.457
Olcese Sand	170	34	0.336	4.9	5.0	0.457
Temblor-Freeman	0.002	0.001	0.338	14.5	0.42	0.457
Vedder Sand (sand layers)	303	60.6	0.264	4.9	13.0	0.457
Vedder Sand (shale layers)	0.1	0.05	0.32	14.5	0.42	0.457
Tumey-Eocence	0.07	0.07	0.07	14.5	0.42	0.457
Baserock	0.0001	0.0001	0.01	22.7	0.5	0.457

Appendix B: AoR Delineation Calculations

Location	50-ft N of Injection Well
X	294000
Y	3951615

Symbol	Parameter	Value	Units
z_i	Depth, injection zone	2355.2854	m
z_u	Depth, USDW	739.7	m
TDS,i	TDS, injection zone	25000	mg/L
TDS,u	TDS, USDW	500	mg/L
T	Average surface temperature	18.9	C
ΔT	Geothermal Gradient	25	C/km
g	Gravitational constant	9.81	m/s^2
λ	Density gradient at constant TDS	-1.22E-05	kg/L*m
		-1.22E-02	kg/m^3*m
ξ	Initial density gradient in borehole	-1.07E-06	kg/L*m
		-1.07E-03	kg/m^3*m
Δρ	Final density difference at USDW base	0.018	kg/L
		18.05	kg/m^3
ΔP_d	**Admissible pressure increase, density difference**	**143,029**	**Pa**
G	Gel Strength, drilling mud	25	$lb/100ft^2$
d	Assumed wellbore diameter	16	inches
ΔP_g	**Admissible pressure, gel strength**	**277,212**	**Pa**
ΔP_a	**Maximum admissible pressure increase, total**	**420,241**	**Pa**
ΔP_a	**Over-pressure, 15 years from TOUGH**	**524,108**	**Pa**

	Depth (m)	T, °C	A	B	Rho (kg/m^3)	ρ, TDS = 500 mg/L (kg/L)	ρ, TDS = 25,000 mg/L (kg/L)
	500	31.4	0.75	-0.004	995.247	0.996	1.014
	750	37.7	0.75	-0.004	993.125	0.993	1.012
	1000	43.9	0.74	-0.004	990.700	0.991	1.009
	1250	50.2	0.74	-0.005	987.995	0.988	1.006
	1500	56.4	0.74	-0.005	985.030	0.985	1.003
	1750	62.7	0.75	-0.006	981.821	0.982	1.000
	2000	68.9	0.76	-0.007	978.378	0.979	0.997
	2250	75.2	0.77	-0.007	974.714	0.975	0.993
	2500	81.4	0.79	-0.008	970.836	0.971	0.990
	2750	87.7	0.81	-0.009	966.751	0.967	0.986
USDW	739.7	37.4	0.75	-0.004	993.219	0.994	1.012
Injection	2355.285	77.8	0.78	-0.008	973.106	0.973	0.992

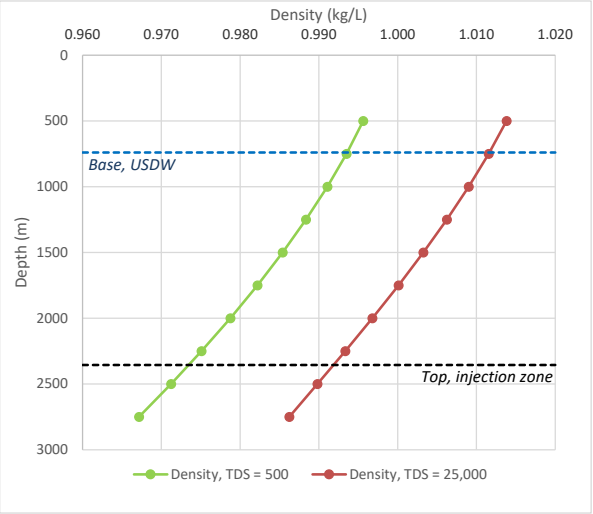

Earthward Consulting, 2016

Water density as function of temperature and concentration

McCutcheon, S.C., Martin, J.L, Barnwell, T.O. Jr. 1993. Water Quality in Maidment, D.R. (Editor). Handbood of Hydrology, McGraw-Hill, New York, NY (p. 11.3)

Water density as a function of temperature only

rho = density in kg/m^3 as a function of temperature

T = temperature in C

rho = 1000(1 - (T+288.9414)/(508929.2*(T+68.12963))*(T-3.9863)^2)

Water density as a function of temperature and salinity

rhos = density in kg/m^3 as a function of temperature and salinity

S = salinity in g/kg

rhos = rho + AS + BS^(3/2) + CS^2

A = 8.24493E-1 - 4.0899E-3*T + 7.6438E-5*T^2 -8.2467E-7*T^3 + 5.3675E-9*T^4

B = -5.724E-3 + 1.0227E-4*T - 1.6546E-6*T^2

C = 4.8314E-4

Location	D-D' at A-A'
X	306000
Y	3952000

Symbol	Parameter	Value	Units
z_i	Depth, injection zone	1350	m
z_u	Depth, USDW	924	m
TDS,i	TDS, injection zone	25000	mg/L
TDS,u	TDS, USDW	500	mg/L
T	Average surface temperature	18.9	C
ΔT	Geothermal Gradient	25	C/km
g	Gravitational constant	9.81	m/s^2
λ	Density gradient at constant TDS	-1.11E-05	kg/L*m
		-1.11E-02	kg/m^3*m
ξ	Initial density gradient in borehole	3.11E-05	kg/L*m
		3.11E-02	kg/m^3*m
Δρ	Final density difference at USDW base	0.018	kg/L
		17.97	kg/m^3
ΔP_d	**Admissible pressure increase, density difference**	**37,543**	**Pa**
G	Gel Strength, drilling mud	25	$lb/100ft^2$
d	Assumed wellbore diameter	16	inches
ΔP_g	**Admissible pressure, gel strength**	**158,892**	**Pa**
ΔP_a	**Maximum admissible pressure increase, total**	**196,435**	**Pa**
ΔP_a	**Over-pressure, 15 years from TOUGH**	**17,994**	**Pa**

	Depth (m)	T, °C	A	B	Rho (kg/m^3)	ρ, TDS = 500 mg/L (kg/L)	ρ, TDS = 25,000 mg/L (kg/L)
	500	31.4	0.75	-0.004	995.247	0.996	1.014
	750	37.7	0.75	-0.004	993.125	0.993	1.012
	1000	43.9	0.74	-0.004	990.700	0.991	1.009
	1250	50.2	0.74	-0.005	987.995	0.988	1.006
	1500	56.4	0.74	-0.005	985.030	0.985	1.003
	1750	62.7	0.75	-0.006	981.821	0.982	1.000
	2000	68.9	0.76	-0.007	978.378	0.979	0.997
	2250	75.2	0.77	-0.007	974.714	0.975	0.993
	2500	81.4	0.79	-0.008	970.836	0.971	0.990
	2750	87.7	0.81	-0.009	966.751	0.967	0.986
USDW	924	42.0	0.74	-0.004	991.468	0.992	1.010
Injection	1350	52.7	0.74	-0.005	986.840	0.987	1.005

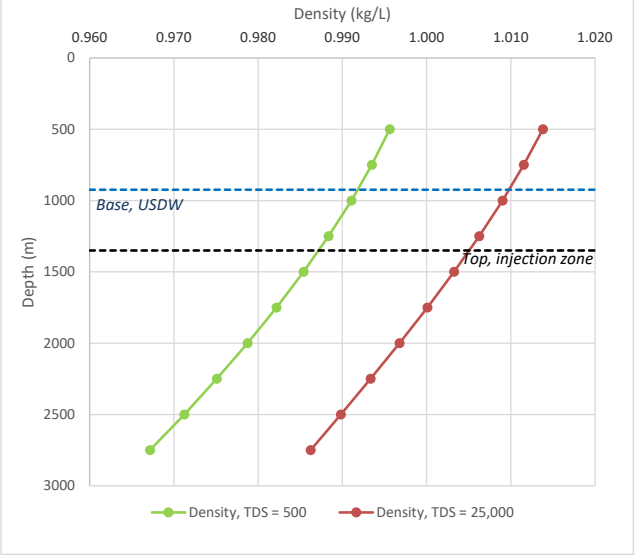

Earthward Consulting, 2016

Water density as function of temperature and concentration

McCutcheon, S.C., Martin, J.L, Barnwell, T.O. Jr. 1993. Water Quality in Maidment, D.R. (Editor). Handbood of Hydrology, McGraw-Hill, New York, NY (p. 11.3)

Water density as a function of temperature only

rho = density in kg/m^3 as a function of temperature

T = temperature in C

rho = 1000(1 - (T+288.9414)/(508929.2*(T+68.12963))*(T-3.9863)^2)

Water density as a function of temperature and salinity

rhos = density in kg/m^3 as a function of temperature and salinity

S = salinity in g/kg

rhos = rho + AS + BS^(3/2) + CS^2

A = 8.24493E-1 - 4.0899E-3*T + 7.6438E-5*T^2 -8.2467E-7*T^3 + 5.3675E-9*T^4

B = -5.724E-3 + 1.0227E-4*T - 1.6546E-6*T^2

C = 4.8314E-4

Location	E-E at B-B
X	303000
Y	3957600

Symbol	Parameter	Value	Units
z_i	Depth, injection zone	1507	m
z_u	Depth, USDW	787	m
TDS,i	TDS, injection zone	25000	mg/L
TDS,u	TDS, USDW	500	mg/L
T	Average surface temperature	18.9	C
ΔT	Geothermal Gradient	25	C/km
g	Gravitational constant	9.81	m/s^2
λ	Density gradient at constant TDS	-1.11E-05	kg/L*m
		-1.11E-02	kg/m^3*m
ξ	Initial density gradient in borehole	1.39E-05	kg/L*m
		1.39E-02	kg/m^3*m
Δρ	Final density difference at USDW base	0.018	kg/L
		18.03	kg/m^3
ΔP_d	**Admissible pressure increase, density difference**	**63,634**	**Pa**
G	Gel Strength, drilling mud	25	$lb/100ft^2$
d	Assumed wellbore diameter	16	inches
ΔP_g	**Admissible pressure, gel strength**	**177,371**	**Pa**
ΔP_a	**Maximum admissible pressure increase, total**	**241,004**	**Pa**
ΔP_a	**Over-pressure, 15 years from TOUGH**	**49,316**	**Pa**

	Depth (m)	T, °C	A	B	Rho (kg/m^3)	ρ, TDS = 500 mg/L (kg/L)	ρ, TDS = 25,000 mg/L (kg/L)
	500	31.4	0.75	-0.004	995.247	0.996	1.014
	750	37.7	0.75	-0.004	993.125	0.993	1.012
	1000	43.9	0.74	-0.004	990.700	0.991	1.009
	1250	50.2	0.74	-0.005	987.995	0.988	1.006
	1500	56.4	0.74	-0.005	985.030	0.985	1.003
	1750	62.7	0.75	-0.006	981.821	0.982	1.000
	2000	68.9	0.76	-0.007	978.378	0.979	0.997
	2250	75.2	0.77	-0.007	974.714	0.975	0.993
	2500	81.4	0.79	-0.008	970.836	0.971	0.990
	2750	87.7	0.81	-0.009	966.751	0.967	0.986
USDW	787.302	38.6	0.75	-0.004	992.782	0.993	1.011
Injection	1507	56.6	0.74	-0.005	984.944	0.985	1.003

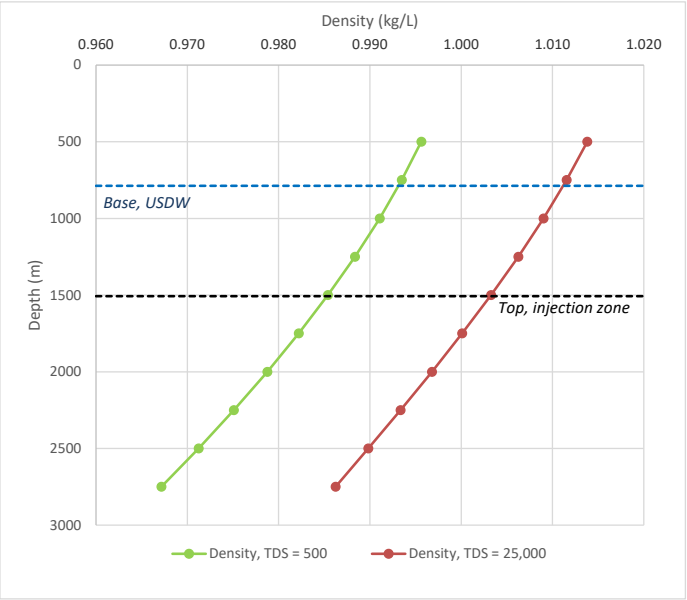

Earthward Consulting, 2016

Water density as function of temperature and concentration

McCutcheon, S.C., Martin, J.L, Barnwell, T.O. Jr. 1993. Water Quality in Maidment, D.R. (Editor). Handbood of Hydrology, McGraw-Hill, New York, NY (p. 11.3)

Water density as a function of temperature only

rho = density in kg/m^3 as a function of temperature

T = temperature in C

rho = 1000(1 - (T+288.9414)/(508929.2*(T+68.12963))*(T-3.9863)^2)

Water density as a function of temperature and salinity

rhos = density in kg/m^3 as a function of temperature and salinity

S = salinity in g/kg

rhos = rho + AS + BS^(3/2) + CS^2

A = 8.24493E-1 - 4.0899E-3*T + 7.6438E-5*T^2 -8.2467E-7*T^3 + 5.3675E-9*T^4

B = -5.724E-3 + 1.0227E-4*T - 1.6546E-6*T^2

C = 4.8314E-4

Location	A-A' at Famoso Hwy
X	304000
Y	3952600

Symbol	Parameter	Value	Units
z_i	Depth, injection zone	1493	m
z_u	Depth, USDW	861	m
TDS,i	TDS, injection zone	25000	mg/L
TDS,u	TDS, USDW	500	mg/L
T	Average surface temperature	18.9	C
ΔT	Geothermal Gradient	25	C/km
g	Gravitational constant	9.81	m/s^2
λ	Density gradient at constant TDS	-1.12E-05	kg/L*m
		-1.12E-02	kg/m^3*m
ξ	Initial density gradient in borehole	1.73E-05	kg/L*m
		1.73E-02	kg/m^3*m
Δρ	Final density difference at USDW base	0.018	kg/L
		17.99	kg/m^3
ΔP_d	**Admissible pressure increase, density difference**	**55,751**	**Pa**
G	Gel Strength, drilling mud	25	$lb/100ft^2$
d	Assumed wellbore diameter	16	inches
ΔP_g	**Admissible pressure, gel strength**	**175,723**	**Pa**
ΔP_a	**Maximum admissible pressure increase, total**	**231,473**	**Pa**
ΔP_a	**Over-pressure, 15 years from TOUGH**	**47,258**	**Pa**

	Depth (m)	T, °C	A	B	Rho (kg/m^3)	ρ, TDS = 500 mg/L (kg/L)	ρ, TDS = 25,000 mg/L (kg/L)
	500	31.4	0.75	-0.004	995.247	0.996	1.014
	750	37.7	0.75	-0.004	993.125	0.993	1.012
	1000	43.9	0.74	-0.004	990.700	0.991	1.009
	1250	50.2	0.74	-0.005	987.995	0.988	1.006
	1500	56.4	0.74	-0.005	985.030	0.985	1.003
	1750	62.7	0.75	-0.006	981.821	0.982	1.000
	2000	68.9	0.76	-0.007	978.378	0.979	0.997
	2250	75.2	0.77	-0.007	974.714	0.975	0.993
	2500	81.4	0.79	-0.008	970.836	0.971	0.990
	2750	87.7	0.81	-0.009	966.751	0.967	0.986
USDW	861.2959	40.4	0.74	-0.004	992.081	0.992	1.010
Injection	1493	56.2	0.74	-0.005	985.117	0.985	1.003

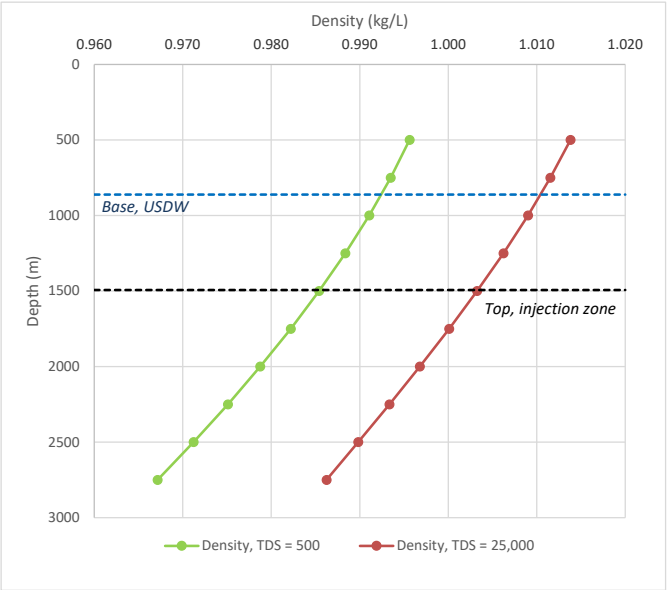

Earthward Consulting, 2016

Water density as function of temperature and concentration

McCutcheon, S.C., Martin, J.L, Barnwell, T.O. Jr. 1993. Water Quality in Maidment, D.R. (Editor). Handbood of Hydrology, McGraw-Hill, New York, NY (p. 11.3)

Water density as a function of temperature only

rho = density in kg/m^3 as a function of temperature

T = temperature in C

rho = 1000(1 - (T+288.9414)/(508929.2*(T+68.12963))*(T-3.9863)^2)

Water density as a function of temperature and salinity

rhos = density in kg/m^3 as a function of temperature and salinity

S = salinity in g/kg

rhos = rho + AS + BS^(3/2) + CS^2

A = 8.24493E-1 - 4.0899E-3*T + 7.6438E-5*T^2 -8.2467E-7*T^3 + 5.3675E-9*T^4

B = -5.724E-3 + 1.0227E-4*T - 1.6546E-6*T^2

C = 4.8314E-4

Location	A-A at Hwy-99
X	298000
Y	3951600

Symbol	Parameter	Value	Units
z_i	Depth, injection zone	2005	m
z_u	Depth, USDW	774	m
TDS,i	TDS, injection zone	25000	mg/L
TDS,u	TDS, USDW	500	mg/L
T	Average surface temperature	18.9	C
ΔT	Geothermal Gradient	25	C/km
g	Gravitational constant	9.81	m/s^2
λ	Density gradient at constant TDS	-1.19E-05	kg/L*m
		-1.19E-02	kg/m^3*m
ξ	Initial density gradient in borehole	2.79E-06	kg/L*m
		2.79E-03	kg/m^3*m
Δρ	Final density difference at USDW base	0.018	kg/L
		18.03	kg/m^3
ΔP_d	**Admissible pressure increase, density difference**	**108,880**	**Pa**
G	Gel Strength, drilling mud	25	$lb/100ft^2$
d	Assumed wellbore diameter	16	inches
ΔP_g	**Admissible pressure, gel strength**	**235,984**	**Pa**
ΔP_a	**Maximum admissible pressure increase, total**	**344,864**	**Pa**
ΔP_a	**Over-pressure, 15 years from TOUGH**	**232,186**	**Pa**

	Depth (m)	T, °C	A	B	Rho (kg/m^3)	ρ, TDS = 500 mg/L (kg/L)	ρ, TDS = 25,000 mg/L (kg/L)
	500	31.4	0.75	-0.004	995.247	0.996	1.014
	750	37.7	0.75	-0.004	993.125	0.993	1.012
	1000	43.9	0.74	-0.004	990.700	0.991	1.009
	1250	50.2	0.74	-0.005	987.995	0.988	1.006
	1500	56.4	0.74	-0.005	985.030	0.985	1.003
	1750	62.7	0.75	-0.006	981.821	0.982	1.000
	2000	68.9	0.76	-0.007	978.378	0.979	0.997
	2250	75.2	0.77	-0.007	974.714	0.975	0.993
	2500	81.4	0.79	-0.008	970.836	0.971	0.990
	2750	87.7	0.81	-0.009	966.751	0.967	0.986
USDW	774	38.3	0.75	-0.004	992.905	0.993	1.011
Injection	2005	69.0	0.76	-0.007	978.307	0.979	0.997

<u>Earthward Consulting, 2016</u>

Water density as function of temperature and concentration

McCutcheon, S.C., Martin, J.L, Barnwell, T.O. Jr. 1993. Water Quality in Maidment, D.R. (Editor). Handbood of Hydrology, McGraw-Hill, New York, NY (p. 11.3)

Water density as a function of temperature only

rho = density in kg/m^3 as a function of temperature

T = temperature in C

rho = 1000(1 - (T+288.9414)/(508929.2*(T+68.12963))*(T-3.9863)^2)

Water density as a function of temperature and salinity

rhos = density in kg/m^3 as a function of temperature and salinity

S = salinity in g/kg

rhos = rho + AS + BS^(3/2) + CS^2

A = 8.24493E-1 - 4.0899E-3*T + 7.6438E-5*T^2 -8.2467E-7*T^3 + 5.3675E-9*T^4

B = -5.724E-3 + 1.0227E-4*T - 1.6546E-6*T^2
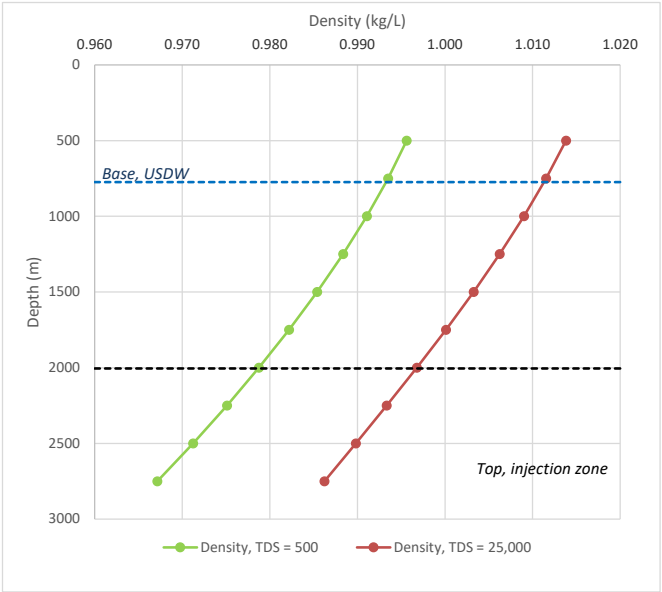
C = 4.8314E-4